FERMILAB-THESIS-2017-03

THE UNIVERSITY OF CHICAGO

FAST TRANSVERSE BEAM INSTABILITY CAUSED BY ELECTRON CLOUD TRAPPED IN COMBINED FUNCTION MAGNETS

A DISSERTATION SUBMITTED TO

THE FACULTY OF THE DIVISION OF THE PHYSICAL SCIENCES

IN CANDIDACY FOR THE DEGREE OF

DOCTOR OF PHILOSOPHY

DEPARTMENT OF PHYSICS

BY

SERGEY ANTIPOV

CHICAGO, ILLINOIS

MARCH 2017

Operated by Fermi Research Alliance, LLC under Contract No. DE-AC02-07CH11359 with the United States Department of Energy

TABLE OF CONTENTS

LIST OF FIGURES

LIST OF TABLES

ACKNOWLEDGEMENTS

Working at Fermilab under the supervision of Prof. Sergei Nagaitsev has been a great experience for me. I am grateful to Sergei for suggesting an interesting topic, for guiding me along the way, and for giving me the freedom to develop my own ideas. I would also like to thank my advisor at the University of Chicago Prof. Young-Kee Kim for giving me the opportunity to be in this interesting field, for her support and motivation, for sharing the energy and wisdom.

At Fermilab I was lucky to do research with and learn from some of the best experts in the field. I would like to thank Valeri Lebedev for sharing with me his deep knowledge on electromagnetism and plasma physics, for the important practical advices and support with the experimental part; Yuri Alexahin for helping with the theory of electron cloud and collective effects; Alexei Burov sharing his profound understanding of beam instabilities and Landau damping, and especially for our countless conversations on the philosophy of science. I would also like to thank Alexander Valishev for the invaluable practical experience I received when working on the design and construction of IOTA.

This work would have been impossible without the support of many people in the Fermilab Accelerator Division. I would like to thank Phil Adamson, Ming-Jen Yang, Rob Ainsworth, Mike Olander, Victor Grzelak and all the Operations Department for their help in conduction numerous beam studies. I would like to thank the members of the electron cloud group: Jeff Eldred, Yichen Ji, Bob Zwaska for numerous useful suggestions and discussions. I am also grateful to Ralph Pasquinelli, Brian Chase, Peter Prieto, and especially to Brian Fellenz from the electrical engineering support group for their invaluable advice and help with the hardware for the microwave measurement.

Finally, I should acknowledge the help and support of people outside Fermilab. I would like to thank my colleagues from Cornell CesrTA for their warm hospitality during my visit in November 2015, Mike Billing for sharing experience and ideas and Jim Crittenden for numerous useful

discussions. I am grateful to Kazuhito Ohmi (KEK) for sharing his PEI code and helping with numerical simulations and to Alex Chao (SLAC) for his wonderful course on collective beam instabilities

ABSTRACT

Electron cloud instabilities affect the performance of many circular high-intensity particle accelerators. They usually have a fast growth rate and might lead to an increase of the transverse emittance and beam loss. A peculiar example of such an instability is observed in the Fermilab Recycler proton storage ring. Although this instability might pose a challenge for future intensity upgrades, its nature had not been completely understood. The phenomena has been studied experimentally by comparing the dynamics of stable and unstable beam, numerically by simulating the build-up of the electron cloud and its interaction with the beam, and analytically by constructing a model of an electron cloud driven instability with the electrons trapped in combined function dipoles. Stabilization of the beam by a clearing bunch reveals that the instability is caused by the electron cloud, trapped in beam optics magnets. Measurements of microwave propagation confirm the presence of the cloud in the combined function dipoles. Numerical simulations show that up to 10^{-2} of the particles can be trapped by their magnetic field. Since the process of electron cloud build-up is exponential, once trapped this amount of electrons significantly increases the density of the cloud on the next revolution. In a combined function dipole this multi-turn accumulation allows the electron cloud reaching final intensities orders of magnitude greater than in a pure dipole. The estimated fast instability growth rate of about 30 revolutions and low mode frequency of 0.4 MHz are consistent with experimental observations and agree with the simulations. The created instability model allows investigating the beam stability for the future intensity upgrades.

CHAPTER 1

ELECTRON CLOUD IN PARTICLE ACCELERATORS

One of the physical effects limiting the intensity in contemporary circular accelerators is the formation of a cloud of low energy electrons inside its beam pipe. The process usually starts with the ionization of residual gas by the beam or photoemission from the walls of the vacuum chamber by synchrotron radiation. The number of electrons then may be multiplied through the emission of secondary electrons from the surface of the chamber. If the secondary emission happens in resonance with an alternating electric field of the incoming beam it can lead to an avalanche multiplication of the number of electrons that form a so-called electron cloud.

The electron cloud can affect the performance of a particle accelerator in several ways. It impacts beam diagnostic equipment [1], causes the degradation of vacuum [2], and increases the heat load, which is critical for superconducting components operating at cryogenic temperatures [3]. The electron cloud also affects both coherent and incoherent transverse motion and causes a spread of incoherent betatron frequencies within the beam, which may affect particle stability. And finally and most importantly, the interaction with the electron cloud can induce transverse instabilities in the beam. Both single-bunch and multi-bunch electron cloud instabilities have been observed in accelerators. The instabilities typically have a fast growth rate and lead to increase of beam emittance and particle losses. Currently, the electron cloud effects are observed in many high intensity machines worldwide: Relativistic Heavy Ion Collider (RHIC) at BNL [4], Cornell Electron Storage Ring (CESR) at Cornell during a dedicated study program with a positron beam [5], Proton Storage Ring (PSR) at LANL [6], KEKB electron-positron collider at KEK in Japan [7], DAΦNE electron-positron collider at INFN Frascati in Italy [8], and in the CERN accelerator complex (PS, SPS, LHC) [9-11].

At Fermilab, an electron cloud instability has been observed at some conditions in the Recycler proton storage ring. While it does not limit the current operation with slip-stacking up to 700 kW of beam power, the instability may pose a challenge for the future PIP-II intensity upgrade [12]. Investigating the electron cloud instability in Recycler we discovered that a previously overlooked mechanism of long-term electron cloud confinement in the magnetic field of combined function dipoles plays a crucial role in the accumulation of the cloud. It allows the electrons accumulating inside the vacuum chamber over multiple beam revolutions in the ring, reaching much greater densities then they would in a pure dipole magnet with no long-term confinement. The resulting dense electron cloud couples with the betatron motion of the beam, driving a fast transverse multi-bunch instability.

This thesis consists of five chapters. Charter 1 introduces the main mechanisms involved in the formation of the electron cloud and various effects arising from its interaction with the beam. Chapters 2 and 3 address experimental studies of the fast electron cloud instability in Recycler. Chapter 2 focuses on the investigation of beam dynamics and presents a novel technique of beam stabilization by injection of a clearing pilot bunch of low charge. The findings of Chapter 2 prove that the observed instability is caused by the electron cloud trapped in beam optics magnets. Chapter 3 is devoted to the microwave measurements of electron cloud density inside the Recycler magnets. Chapter 4 addresses the numerical studies of the electron cloud build-up and the resulting transverse multibunch instability in the Recycler proton beam. Finally, Chapter 5 presents an analytical model of the electron cloud instability. Using the developed model, we estimate the strength of the instability for the future higher intensities and discuss the ways of its mitigation.

In this chapter we first describe the different physical processes leading to the generation and accumulation of the electron cloud in a particle accelerator. Then we briefly review the instabilities arising from the beam-cloud interaction. In conclusion, we discuss a way of electron cloud suppression through the so-called 'conditioning' of the beam-pipe.

1.1 Electron cloud build-up

The process of electron cloud build-up starts with a few "primary" electrons that launch a multipacting avalanche (Fig. 1.1). The circulating beam can produce these electrons through different mechanisms, e. g. ionization of the residual gas in the vacuum chamber or photoemission from the chamber's wall due to the synchrotron radiation. The primary particles then can be accelerated by a passing bunch to the energies of several hundreds of eV to a few keV, depending on the beam intensity. When an electron of such a high energy hits the wall of the vacuum chamber, it is likely to create several "secondary" electrons on impact. The secondaries typically have low energies – up to a few tens of eV – insufficient to produce their own secondaries on impact. But, if these particles have the right energies, they can survive until the passage of the next bunch and, in turn, be accelerated, projected onto the wall and produce more secondaries. Repeating on the passage of every bunch, this multipacting cascade builds up the electron cloud during the passage of the beam.

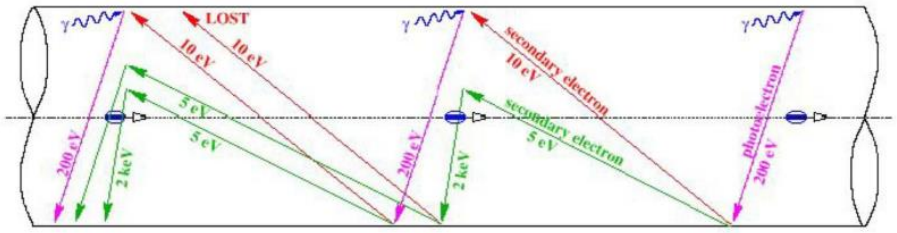

Figure 1.1: A qualitative illustration of the build-up of the electron cloud in the LHC for the case of 25-ns bunch spacing [13]. The process starts with photoelectrons and is amplified by the secondary emission.

1.1.1 Generation of primary electrons

There are several processes, contributing to the generation of primary electrons: photoemission from synchrotron-radiated photons striking the chamber walls; ionization of residual gas; and beam halo particles striking the walls of the chamber. Depending on the type of machine, one of these three processes is typically dominant. For example, in positron or electron storage rings, the beam emits synchrotron radiation in the bending magnets with a critical energy [14]:

$$\varepsilon_c = \frac{3}{2}\hbar c\gamma^3 / \rho , \tag{1.1}$$

where $\hbar$ is the Planck constant, c – speed of light, γ – relativistic factor, and ρ – bending radius. Typically, $\varepsilon_c \sim 1$ keV, leading to emission of photoelectrons upon striking the vacuum chamber. The total instantaneous power emitted by a beam particle (positron or electron) is

$$P_\gamma = \frac{2cr_e}{3\rho^2}\frac{E^4}{\left(m_e c^2\right)^3}, \tag{1.2}$$

where m_e stands for electron mass, r_e – classical electron radius, and E – beam kinetic energy. Because of the steep dependence of P on beam energy, the ratio of the number of generated primary electrons to the number of particles in the beam can be as high as ~1 [15].

In proton rings, the process is typically dominated by ionization of residual gas, or by electron generation when stray beam particles strike the chamber. The number of ionization electrons depends on the density and chemical composition of the residual gas:

$$n_{ion} = \sigma_{ion}\rho_m N , \tag{1.3}$$

where n_{ion} is the linear density of ionization electrons, σ_{ion} – ionization cross-section, ρ_m – molecular density, and N – number of beam particles. A notable exception is the LHC and some of the proposed future colliders i.e. FCC and CEPC, where the dominant mechanism is the photoemission. In the

LHC, for example, the beam emits significant synchrotron radiation, ~ 0.4 photons per proton per bending magnet, with a photon critical energy ~ 44 eV [16].

1.1.2 Secondary emission

The aggregate effect of secondary emission is usually what determines the density of the electron cloud. It is particularly strong in positively-charged bunched beams, when the production of secondary electrons comes in resonance with their acceleration by oncoming bunches. In negatively charged beams, the electrons born at the wall of the vacuum chamber are pushed back towards the wall with relatively low energy, resulting in relatively inefficient secondary emission.

Following the work of Furman and Pivi [17], we can define three separate components of the secondary emission yield: electrons elastically scattered back from the surface; scattered from one or more atoms in the bulk and reflected back, or "rediffused"; and the "true-secondary" electrons (Fig. 1.2). There is no fundamental difference between the processes of backscattering and rediffusion, and in our simulation (Chapter 4) we treat them on equal footing in our numerical model. Multiple models exist to describe each of the components of the SEY. We are not going to cover all of them in this Section, rather we will present some typical properties of the secondary emission. More details can be found, for example in [17] and [18].

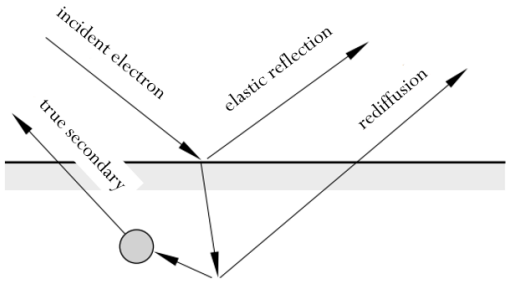

Figure 1.2: The three types of emission processes. The blob is represents a nontrivial interaction yielding true-secondary electrons [17].

The total SEY δ is a sum of a true secondary and an elastic backscattering (which includes reflection and rediffusion) components:

$$\delta = \delta_{true} + \delta_{el} . \tag{1.4}$$

The probability of an electron to reflect back can be described by an exponential fall-off:

$$\delta_{el}(E) = \exp(-E / E_w) . \tag{1.5}$$

δ_{el} is independent of the incident angle θ and only depends on the electron's energy E. The width E_w = 10 eV. The backscattered electrons elastically interact with the material and are emitted with the same energy with which they impacted on the surface.

The true secondary component of the SEY can be estimated as:

$$\delta_{true} = \delta_{\max} \frac{s(E / E_{\max})}{s - 1 + (E / E_{\max})^s} , \tag{1.6}$$

where s is a material specific parameter. δ_{true} reaches a maximum value δ_{max} at the incidence energy E_{max}. the parameters δ_{max} and E_{max} depend of the incidence angle, but can be considered constant for incidence close to normal [17]. The true secondary electrons are emitted with a $\cos(\theta)$ angular distribution with respect to the direction normal to the surface and their energy spectrum has a sharp spike around a few eV (Fig. 1.3).

Since E_{max} ~ 200-300 eV is much greater than the width of elastic backscattering E_w the maximum, the true secondary emission dominates at higher energies and the maximum total value of SEY is equal to δ_{max}. The value of δ_{max} determines whether the wall of the vacuum chamber acts as an absorber or an emitter of electrons (Fig. 1.4), and thus plays a key role in the accumulation of the electron cloud. In the following pages we will refer to the maximum value of the total secondary yield as just SEY.

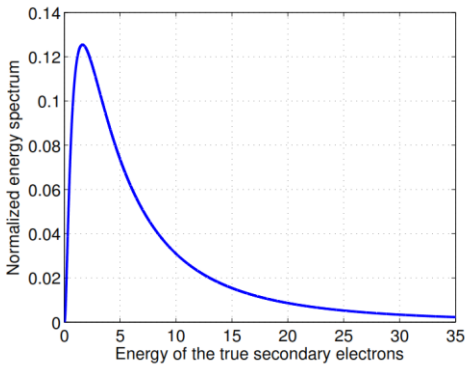

Figure 1.3: Most of the true secondary electrons have relatively low energies, below 10 eV [19].

1.1.3 Build-up regimes

When a bunch passes through a section of accelerator beampipe, containing an electron cloud, the cloud density does not remain constant. As it was discussed in the previous section, the bunch produces new primary electrons and kicks the existing ones. The electrons then impact the chamber and may be backscattered, rediffuse, or be absorbed, possibly producing one or more secondaries. Following Iadarola [19] we can define an effective secondary electron yield as the ratio of the average electron cloud densities during the passage two consecutive bunches:

$$\delta_{eff} = \frac{n_{i+1} - n_0}{n_i}, \tag{1.7}$$

where n_i and n_{i+1} are the electron cloud densities 'seen' by the i-th and the i+1-th bunches respectively, and n_0 is the density of primary electrons. The value of δ_{eff} depends on the energy of electrons, hitting the wall of the vacuum chamber and its material properties.

If the SEY is below 1 for any energy of incident electron $\delta(E) < 1$, the vacuum chamber acts as an electron absorber. This regime is called the "seed accumulation". The electron density increases linearly with time until it reaches an equilibrium between the production of primary electrons and electron absorption by the wall. The equilibrium density is comparable with the density of the primary electrons: $n_e(t) \sim n_0$.

If the effective SEY is greater than 1, the number of electrons will multiply with the passage of each new bunch, increasing exponentially with time. This regime is called the "multipacting regime". The rate of the exponential build-up is $n_e(t) \propto \exp[(\delta_{eff} - 1)t/\Delta t]$, where Δt is the bunch spacing. Here we assumed that the density of primary electrons n_0 is small compared to the total density n_e.

As the electron cloud builds up, its density increases exponentially with time and at a certain point the particle losses compensate the production, bringing δ_{eff} down to 1. This is called the "saturation". One of the mechanisms of the saturation is the screening of the positive charge of the beam by the dense negatively charged cloud, as considered in detail in Sect. 4.3.3. The screening reduces the energy the beam supplies to the cloud electrons and, consequently, the lowers the yield (Fig. 1.4). Figure 1.5 depicts the three build-up regimes, simulated in PEI code (the simulation tools and procedures are described in Chapter 4). In the simulation we varied the SEY from a moderate to somewhat unreasonably high values to see how it changes the build-up of the electron cloud density.

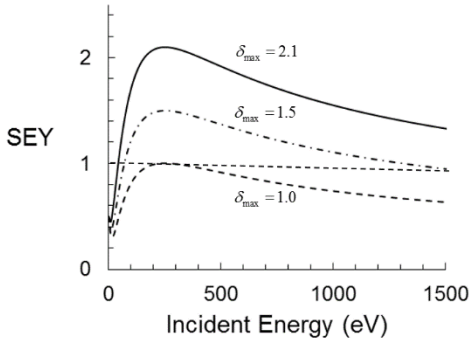

Figure 1.4: The material behaves as an absorber when the secondary yield $\delta < 1$ and as an emitter when $\delta > 1$.

A transition from the seed accumulation to the multipacting regime happens when the bunch charge becomes high enough to accelerate the electron cloud electron to the energies where $\delta > 1$ (Fig. 1.4). When the cumulative effective yield δ_{eff} becomes greater than unity an avalanche multiplication process starts, significantly increasing the cloud density (Fig. 1.6).

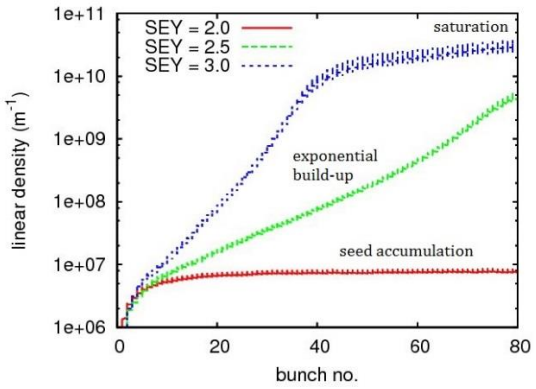

Figure 1.5: As the secondary yield increases the electron cloud goes from the seed accumulation regime to the exponential build-up. Linear density of the cloud in a Recycler dipole magnet is plotted as a function of time during a passage of a typical proton bunch train of 80 bunches. Each bunch produces 10^6 m^{-1} primary ionization e$^-$. The SEY stands for the maximum total yield, achieved at E = 250 eV.

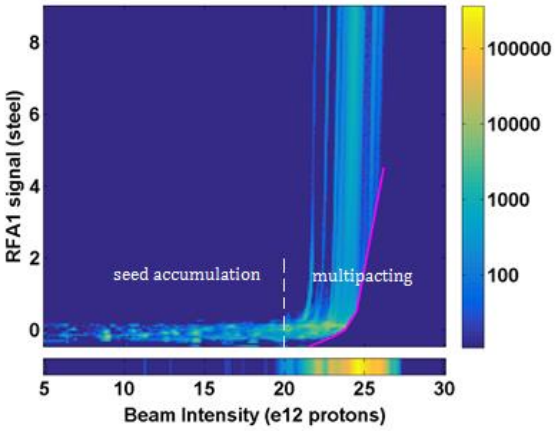

Figure 1.6: The density of the electron cloud increases dramatically as the beam intensity crosses the threshold. The signal from an electron cloud Retarded Field Analyser (RFA) detector, installed in the Fermilab Main Injector, is plotted as a fuction of the total beam intensity. The color repesents the strength of the signal in a logarithmic scale. Above the threshold intensity of ~ 20×10^{12} p most of the signals exceeded the voltage limits of the preamplifier; this data is shown separately below the main plot [20].

1.1.4 Effect of external magnetic field

During the above discussion we assumed that the electron cloud was forming in a drift section with no external fields applied. Presence of strong magnetic field (for example, in bending dipole magnets, focusing quadrupoles, or sextupole chromaticity correctors) significantly affects the build-up rate and the resulting spatial distribution of the electron cloud.

In a strong constant magnetic field non-relativistic electrons will follow a helical trajectory around the field lines (Fig. 1.7). The revolution, or cyclotron, angular frequency ω_c and radius r_c of the orbit are given by simple relations (in CGS units):

$$\begin{aligned} \omega_c &= \frac{eB}{m_e c} \\ r_c &= \frac{m_e c v_\perp}{eB} \end{aligned}, \tag{1.8}$$

where m_e and e are the electron mass and charge, c – speed of light, B – magnetic field, and $v_\perp$ is the component of the electron's velocity transverse to magnetic field line. When a cloud electron receives a kick for a passing beam, it acquires an energy of a few hundred eV. For a typical field of 1 kG and an electron energy of 200 eV we get $\omega_c = 1.8\times10^{10}\,\mathrm{s}^{-1}$ and $r_c < 0.5\,\mathrm{mm}$. Since the radius of the orbit remains quite small compared to the dimensions of the beam camber (a few to ten cm), and the cyclotron period is much smaller than a typical bunch spacing (tens of ns) the electrons, essentially, only move along the lines of the magnetic field. That restriction concentrates the cloud in a small area of space, for example a stripe, crossing the beam center for the case of a dipole field, increasing its maximum density and enhancing the resonant multipacting process.

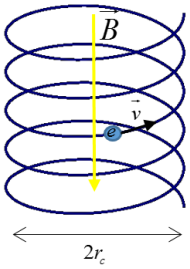

Figure 1.7: An electron moving in a uniform magnetic field follows a helical trajectory.

Fig. 1.8 shows the typical electron cloud distributions for three different magnetic field configurations. In the absence of the field the cloud uniformly fills the available aperture with a slightly higher density near the surface of the vacuum chamber, where the new secondary electrons are produce. In a strong magnetic field cloud is aligned along the field lines and the maximum density is located near the magnetic poles. For the dipole field the dense electron cloud is located at the beam center, which is dangerous because of a potential cloud-beam instability. The difference in the cloud build-up between Fermilab Recycler dipoles and drifts is examined in Sect. 4.3.7.

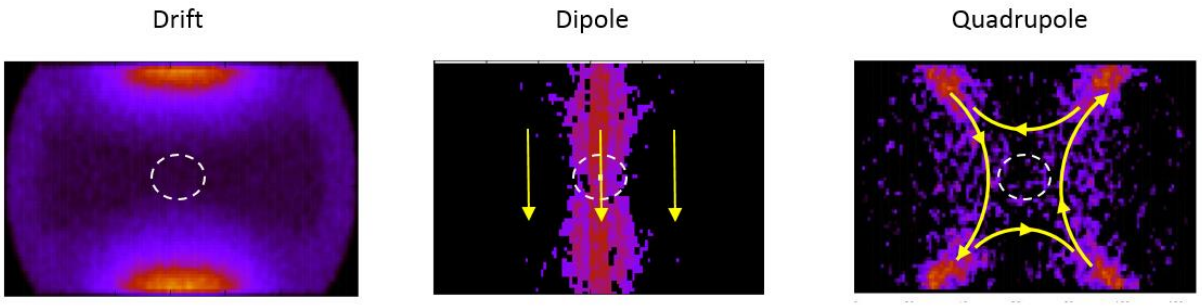

Figure 1.8: Snapshots of electron cloud density in a drift section (left), a dipole (middle), and a quadrupole (right). Yellow lines show the direction of the external magnetic field; white circle represents 2 rms beam size. The distribution was simulated using the PEI code. The simulation procedure and parameters of the model are described in Chap. 4.

1.2 Electron cloud instabilities

The electron cloud provides a media for the beam to interact with itself and may cause a collective beam instability. A typical picture of the instability is as follows: a part of the beam, displaced from the reference orbit, impacts the electron cloud, the cloud then kicks the following part of the beam. If the kicks fall in phase with the transverse motion of the beam, it starts increasing exponentially. This uncontrolled increase of beam oscillations is called an instability. Multiple models exist to describe the electron cloud instabilities (see, for example, [21]). A detailed analytical description of a multi-bunch instability with the cloud located in a dipole magnet is presented in Chapter 5.

The first observation of a beam-cloud instability dates back to 1965, when it was observed in a bunched proton beam at storage ring at the Budker Institute (BINP) in Novosibirsk, Russia. The instability lead a coherent growth of betatron oscillations and beam loss above a threshold intensity of $1-1.5\times10^{10}$ p (Fig. 1.9). Later the instability was observed with a coasting proton beam at BINP. Since then the electron cloud induced instabilities were observed in many rings around the world: for example, in Argonne ZGS and BNL AGS in 1960's (bunched beams), CERN ISR in 1972 (coasting beam), Los Alamos PSR in 1988 (Fig. 1.9) (long bunch, harmonic number h = 1). The instabilities shared common characteristic features: coherent betatron oscillation in the vertical plane starts, grows, and ultimately results in a loss of the beam [21].

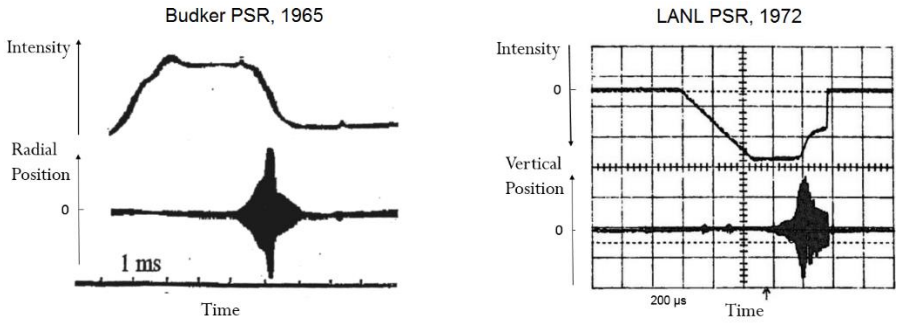

Figure 1.9: Observations of an electron-driven instability at the INP PSR in 1965 (left) and LANL PSR in 1990 (right). A coherent betatron oscillation starts, grows, and results in beam loss [21].

An electron cloud effect in lepton beams had not been seen before 1989 when the KEK Photon Factory switched from electron to positron operation. The positron beam suffered from a vertical multibunch instability which had not been seen with electron beams. The pattern of unstable modes indicated a presence of short-range wakefields, extending only over a few bunches. The instability was interpreted as one driven by photoelectrons. It was suppressed by applying a clearing voltage of 2.5 kV to the beam-position monitors around the ring. In an attempt to model this phenomenon numerically, a computer code was developed to simulate the build-up of the electron cloud inside the vacuum chamber and the resulting wake forces [22].

Apart from the multi-bunch instabilities the electron cloud can also lead to a single bunch head-tail instability, often observed as the blow-up of the transverse size of individual bunches. An intra-bunch head-tail instability in a positron beam was first observed in 1999 at the KEKB. The size of a beam consisting of closely spaced bunches blew up above a certain intensity threshold. Since the key source of the primary electrons in a lepton machine is the photoemission, it was possible 'cure' the instability by installing special solenoids. The solenoids kept the electrons near the surface of the vacuum chamber, away from the beam, thus preventing the multipacting (Fig. 1.10, left). The single bunch nature of the blowup was proven by injecting a test bunch immediately behind a train of

bunches and studying the variation of its size with the charge the charge, while keeping the charge of the preceding bunches constant. The observed increase of the size of the test bunch with the bunch current confirmed the single-bunch range of the instability (Fig. 1.10, right).

The character of the instability can be different in the two transverse planes. An example of such phenomena can be found in the CERN SPS. The machine operates with bunched proton beams with the spacing of 25 ns and bunch intensity 1.15×10^{11} p. At high intensity a fast transverse instability was observed with the growth time of about 50 revolutions (~ 1 ms) in both planes. In the horizontal plane it is a long wavelength coupled bunch instability with all bunches oscillating approximately in phase (Fig. 1.11, left). In the vertical plane the instability shows a single-bunch character with no phase or amplitude correlation between the successive bunches (Fig. 1.11, right).

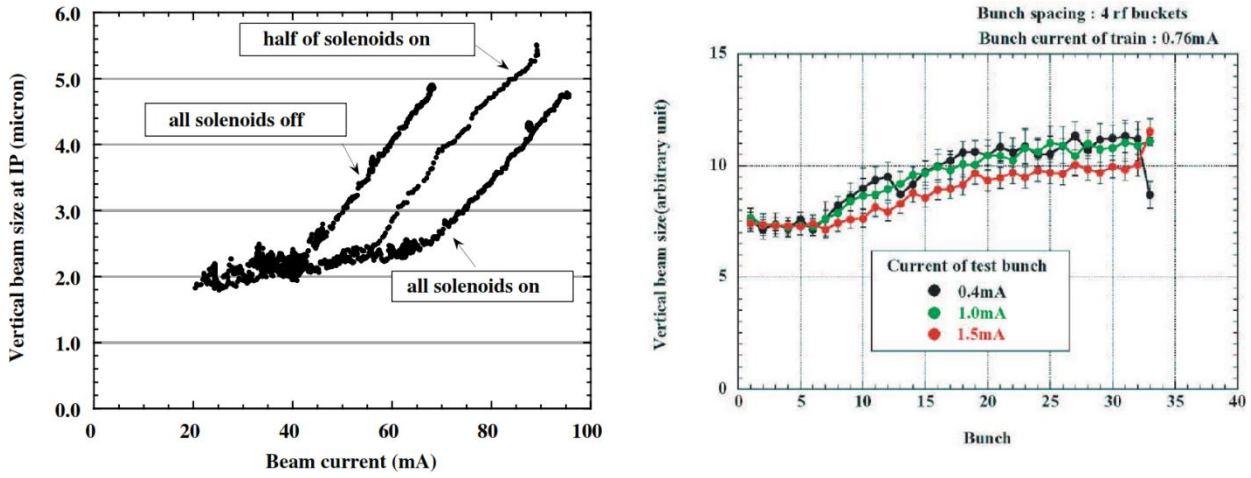

Figure 1.10: Left - vertical beam size of the KEKB increases above the threshold current. Installation of solenoids covering 800 m of ring circumference allows increasing the threshold. Two trains with 60 bunches with a bunch spacing of 4 RF buckets were injected in opposite sides of the ring. Rigt – when a test bunch follows the beam, its vertical size increases. The horizontal axis shows the length of the main bunch train [21].

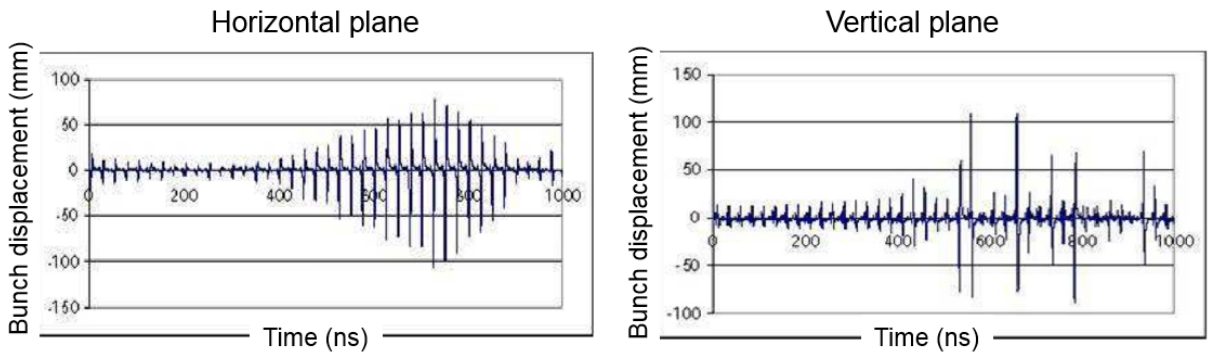

Figure 1.11: At SPS the electron cloud instability is multi-bunch in the horizontal plain (left) and single-bunch in the vertical (right). Snapshots of horizontal position of the first 48 bunches in the SPS when the instability is present [21].

To sum it up, a dense electron in a particle accelerator cloud can drive a transverse instability. It is characterized by a fast rise time and a sharp intensity threshold. Depending on the location of the electron cloud: beam optics magnets or free space, the instability can have either short or long wavelength (head-tail or multi-bunch) and can affect one or both transverse planes. The instability was observed both in proton and positron rings in bunched and coasting beams.

1.3 Electron cloud tune shift

Even if the electron cloud does not cause an instability, it still affects the coherent and incoherent betatron frequencies. In accelerators the betatron frequencies are commonly measured in the units of 'tune' Q, which is a ratio of the frequency ω_β to the revolution frequency ω_0: $Q = \omega_\beta / \omega_0$. Assuming a uniform cloud distribution and a round beam, the negative charge of the electron cloud induces a coherent single-bunch tune shift, which is related to its density as [23]:

$$\Delta Q_{x,y} = \frac{r_p}{2\gamma} \left\langle \beta_{x,y} \right\rangle n_{cl} C, \tag{1.9}$$

where r_p denotes the classical radius of the beam particles (p or e^+), $\langle\beta\rangle$ - average β-function, n_{cl} - cloud density, and C – accelerator circumference. For a flat beam and a flat geometry the vertical tune shift would be larger by a factor of 2. The tune shift ΔQ can be considerable for a sufficiently high electron cloud density. According to simulations, it can be as high as $\sim 10^{-2}$ in the CERN SPS (Fig. 1.12).

If the ring is filled with the beam non-uniformly, the electron cloud density ρ_e varies along the bunch train. Bunches in the head of the train encounter little amount of the electron cloud and their betatron frequencies stays unperturbed, whereas bunches in the tail see the much higher amount of electrons, accumulated during the passage of the previous bunches, and consequently experience a strong betatron tune shift.

Since the actual cloud distribution is non-uniform (Fig. 1.8) the field of the electron has higher order components that introduce dependence of incoherent betatron frequencies on the amplitude of the motion. This nonlinear spread of the incoherent tunes might be beneficial for Landau damping of collective effects (we briefly touch the concept of Landau damping in Chapter 5, for more details refer to [24]). A stabilization of the beam by Landau damping through the cloud-induced tune spread was observed in 1967 at the BINP PSR. Then an electron cloud instability in a coasting proton beam was suppressed by simultaneously increasing the beam intensity and the density of residual gas. This compensation scheme allowed increasing the instability threshold by a factor of 15: from 1.2×10^{11} to 1.8×10^{12} p [21]. The fast accumulation of the secondary plasma electrons by gas ionization was essential for the stabilization of the beam [25].

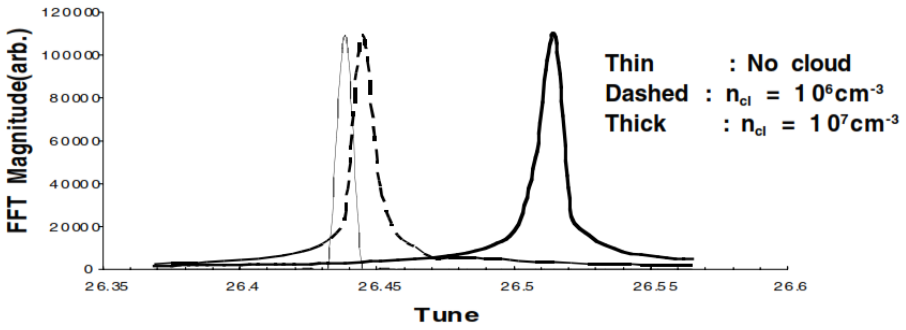

Figure 1.12: Presence of an electron cloud shifts the betatron frequency at CERN SPS. Simulation for different cloud densities made using a QUICKPIC code [26]. The tune spread is relatively small (much less than the tune shift), suggesting that the force of the electron cloud is almost linear with displacement. The model did not include gradients of the cloud density along the ring.

1.4 Beampipe conditioning

When an accelerator operates its vacuum chambers get exposed to a high radiation environment. Under this exposure the secondary emission properties change, lowering the SEY. This process is commonly referred to as 'conditioning'. Conditioning is beneficial for lowering the density of the electron cloud and increasing the instability threshold. It can be achieved both naturally, over the course of standard operation, and by means of special scrubbing runs. Conditioning during the operation has been observed at the Fermilab Main Injector and Recycler and has been studied at a dedicated test stand at the Main Injector.

The test stand, depicted in Fig. 1.13, studied the secondary yield material samples in the typical accelerator conditions. The samples undergo standard cleaning and polishing before going into the beampipe. They can be retracted into the study chamber for the SEY measurement using a specially designed arm. The arms are protected by faraday boxes to eliminate leakage current. The SEY measurement is performed using an electron gun that scans over an energy spectrum of 45 eV to 1545

eV with a 1 mm diameter spot. The measurement stand has two different arms so that two samples can be exposed to the same dose for comparison.

According to test stand data, the secondary yield of a new, 'fresh', stainless steel vacuum chamber can be as high as 2.1 – 2.4. After being exposed to the accelerator environment the SEY slowly decreases (Fig. 1.14). The ultimate value of the peak secondary yield decreases linearly with the beam intensity [27]. After the beam has been shut down the secondary emission yield of exposed beampipe rapidly increases. This process is known as 'deconditioning'. Recent measurements at the Fermilab SEY test indicate that the deconditioning is very rapid: a significant increase of SEY is observed already on the first day of the shutdown. The SEY of 316L stainless steel increases by over 20% over the course of the first week (Fig. 1.15). More detailed studies of deconditioning are currently under way at the Fermilab test stand.

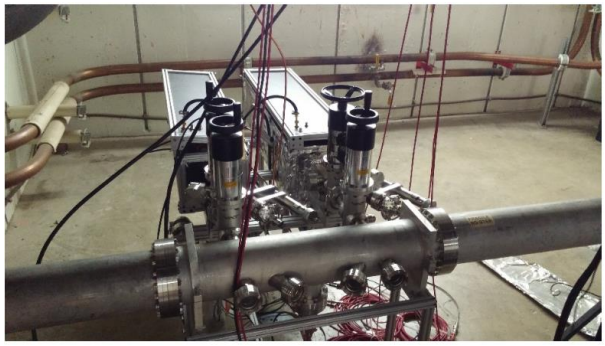

Figure 1.13: A picture of the SEY test stand in the Fermilab Main Injector

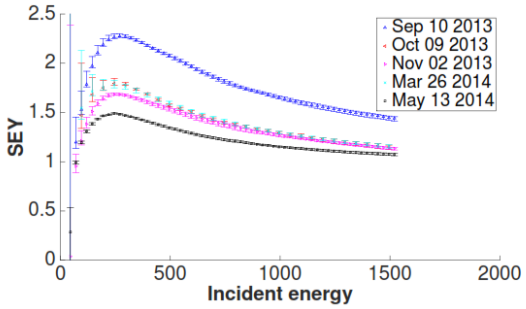

Figure 1.14: The secondary emission yield of 316L stainless steel reduces significantly as it conditions under the exposure to the accelerator beam during the 2013-14 run [27]

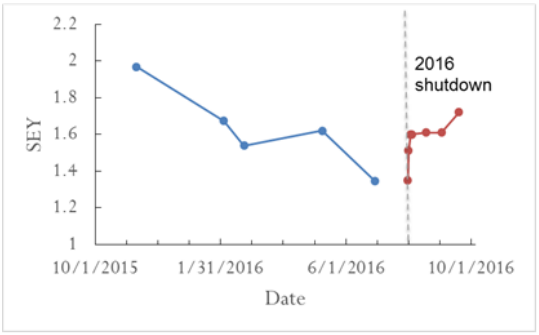

Figure 1.15: The SEY decreases during an accelerator run and then rapidly increases after the beam has been turned off. SEY measurement at the Fermilab Main Injector test stand during the 2015-16 run and the following maintenance shutdown [28].

Emission of secondary electrons is the key process governing the accumulation of the electron cloud in particle accelerators. Sufficiently high secondary yield leads to an avalanche multiplication of the cloud during the passage of the beam, which might induce to a fast transverse instability, leading to increase of betatron oscillations, emittance growth, and beam loss. The process of build-up depends on the material and cleanliness of the beampipe, beam intensity, and external magnetic fields. The SEY of the vacuum chamber, which plays a major role in the build-up, reduces as the beampipe conditions during the high-intensity operation. This conditioning significantly reduces the amount of the cloud and increases the intensity thresholds of electron cloud driven instabilities.

CHAPTER 2

BEAM DYNAMICS MEASUREMENTS OF THE FAST INSTABILITY

In 2014 a fast transverse instability was observed in the proton beam of the Fermilab Recycler. The instability acts only in the horizontal plane and typically develops in about 20 revolutions. The instability also has the unusual feature of selectively impacting the first batch above the threshold intensity of ~ $4*10^{10}$ protons per bunch. These peculiar features suggest that a possible cause of the instability is electron cloud. Earlier studies by Eldred et. al. [29] indicated the presence of electron cloud in the Recycler and suggested the possibility of its trapping in Recycler beam optics magnets.

The fast instability seems to be severe only during the start-up phase after a shutdown, with significant reduction being observed after beam pipe conditioning during beam scrubbing runs [30]. It does not limit the current operation with slip-stacking up to 700 kW of beam power, but may pose a challenge for a future PIP-II intensity upgrade. In order to understand the true nature of the instability in Recycler measurements of the dynamics of both stable and unstable beams have been performed.

In this chapter we, first, describe the beam manipulation and diagnostic tools available at Recycler. Then we show the results of beam dynamics study of the fast instability, supporting the hypothesis of its electron cloud nature. And finally, we present the technique of beam stabilization using a pilot bunch to clear the electron cloud and discuss its possible implementation in Recycler.

2.1 Beam manipulation and diagnostics

The beam dynamics measurements were made using the Fermilab's Accelerator Control Network (ACNET) [31]. ACNET allows tuning beam and accelerator parameters in real time and offers a variety of methods of beam diagnostics. Using ACNET one can control beam structure and intensity;

adjust ring parameters, such as betatron frequencies and chromaticities, etc.; run beam diagnostics: longitudinal beam profile, and its transverse position (Fig. 2.1).

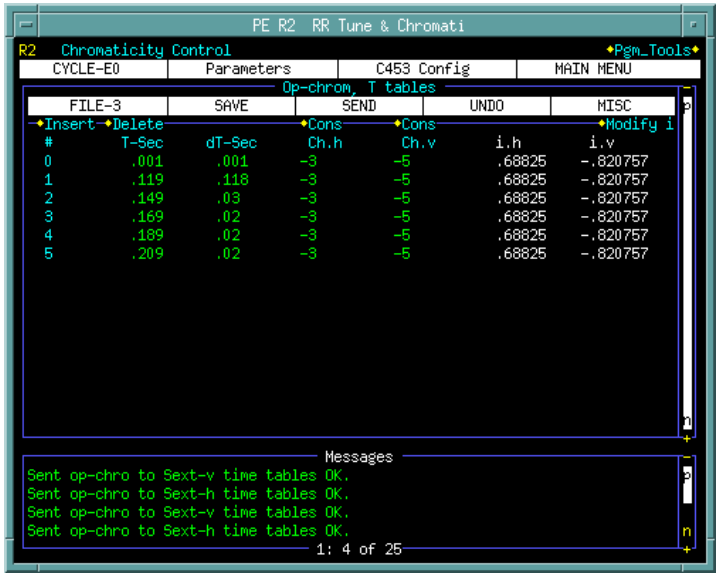

Figure 2.1: Sample ACNET page: Recycler Chromaticity Control. The control program automatically adjusts the sextupole strengths to achieve the desired chromaticity values during a study cycle.

2.1.1 Beam manipulation

The Recycler receives its 8 GeV proton beam form the Fermilab Booster synchrotron ring [32]. The azimuthal space in the Booster is divided into 84 buckets with up to 80 of those buckets filled with the beam. The beam intensity can be varied in the multiples of about $0.3*10^{10}$ protons per bunch, also known as 'turns'. This limitation comes from the specifics of the multi-turn injection procedure from the Linac into the Booster.

The Booster extracts 8 GeV protons to the Recycler (or the Main Injector) at a rate of 15 Hz and each Booster pulse is known as a batch. During the injection one can remove an arbitrary amount of bunches from the batch, varying the total number of bunches from 1 to 80. This is done by mistiming the Recycler injection kickers and sending the extra beam to the beam abort. Also, during the injection

one can adjust the so-called longitudinal bunch rotation, creating and controlling oscillations of bunch length and thus beam density, and mismatch the beam transversely, creating transverse dipole oscillations of the beam.

Six 84-bucket Booster batches and a 84-bucket kicker gap fill the 588-bucket azimuthal space of the Recycler. During the normal operation all six batches are present, but during the studies one can order any amount of batches from one to six. The individual injection positions of those batches can be adjusted as well.

2.1.2 Ring manipulation

ACNET allows its users controlling the betatron frequencies $Q_{x,y}$ and the linear chromaticities $\xi_{x,y} = \partial Q_{x,y} / \partial(\delta p / p)$ by automatically tuning ring quadrupole and sextupole magnets to reach the desired values. It does not feature a separate control for the synchrotron frequency Q_s, instead it gives control over RF voltage and phase V_{RF} and ϕ_{RF}, allowing to change both Q_s and the height of RF bucket.

The total amount of time the beam spends in the ring is controlled by the timing of injection and extraction kickers. During a study cycle one inject up to six 80-bunch Booster batches with $1/15 \approx 0.067\text{s}$ between subsequent injections. The injection positions of these bathes can be adjusted, allowing to create an empty gap between the batches of an arbitrary length (Fig. 2.2).

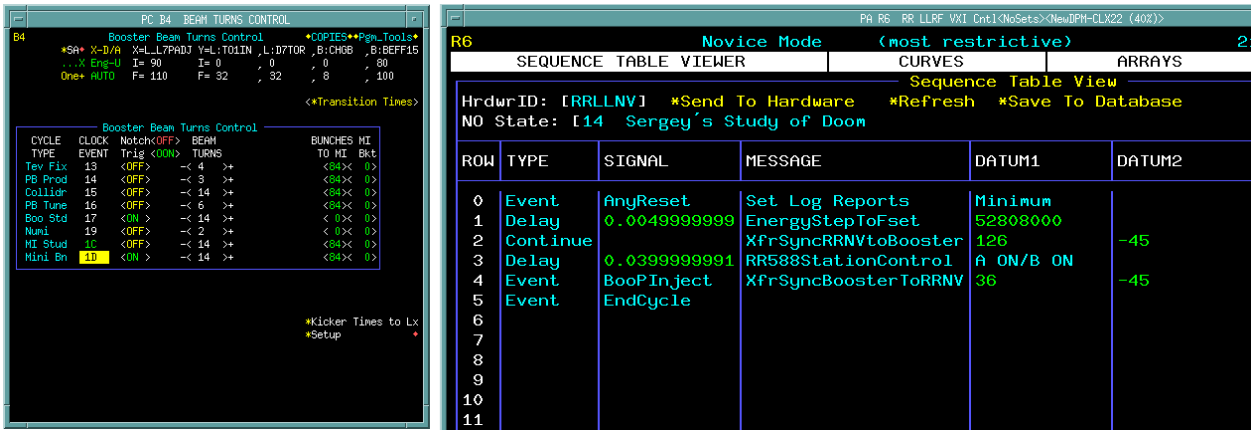

Figure 1.2: ACNET control of injecting beam. Left – Booster intensity control that allows changing the beam intensity (in turns) and the number of bunches for each specific event. Right – Recycler injection control with two injection events into the RF buckets 126 and 36; RF frequency set at 52.8 MHz, RF phase – at -45 deg.

Recycler transverse feedback system can be configured to damp dipole oscillations for a part of the beam, the whole beam, or not damp at all. It is convenient to leave the dampers on when searching for the instability threshold. The dampers prevent intolerable beam loss and triggering of the beam abort system. Since damper kicks affect the coherent beam frequencies, it is necessary to have them off when studying the dynamics of the instability.

2.1.3 Beam diagnostics

For the purpose of this study the most commonly used tools of beam diagnostics were beam position monitors (BPMs) to measure the motion of the beam centroid and determine the thresholds of the instability, wall current monitors (WCMs) to measure the oscillations of the longitudinal beam size and its peak intensity, and stripline detectors to measure betatron frequency shifts and find unstable modes.

The Recycler BPMs are 1-foot-long split-can type monitors, consisting of two either vertical or horizontal plates inside an elliptical vacuum chamber [33,34]. The difference signal from the plates is amplified and integrated over the course of 40 RF buckets to show the respecting (horizontal or vertical) displacement of the beam relative to its reference orbit. The BPM gain can vary to adjust the dynamic range to a particular beam intensity and its timing can be set up to collect data at an arbitrary time during the machine cycle.

A wall current monitor is a device that measures the image charge that flows on the vacuum chamber following the beam. Recycler WCMs have a 4 GHz bandwidth and are capable of reproducing the exact longitudinal beam profile [35]. Together with the stripline detector the WCM allows an acquisition of the full 3D profile of the beam.

An important piece of beam diagnostics is the stripline detector. There are two detectors in Recycler, each composing of two striplines: horizontal or vertical inside a common vacuum chamber (Fig. 2.3). The striplines are quarter-wave for the RF frequency of 52.8 MHz. They are connected to a fast oscilloscope, capable of digitizing the signal at sampling rate of 0.1 ns. This high temporal resolution allows looking at the internal structure of a bunch and finding higher order oscillation modes, in contrast to the BMP's which are only capable of tracing the motion of the center of mass.

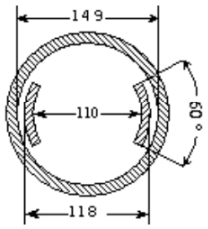

Figure 2.3: Cross section of stripline detector [36].

2.1.4 Factors beyond control

A major factor affecting the precision of the measurements is the quality of the Booster beam. As the Booster team is upgrading the machine and its operations, the amount of beam losses and hence the intensity in Recycler changes. The beam's transverse emittance and longitudinal profile also tend to change with time, making repeated measurements a challenging task. The beam losses in the MI-8 beam line, which is used to transfer the beam from the Booster to the Recycler, also vary slightly from injection to injection, affecting the control over the beam intensity in the Recycler.

Another important unknown factor is the secondary emission yield of the Recycler beampipes. SEY changes with time during accelerator operation due to the process called 'conditioning'. Recent studies show that during the conditioning SEY can change by as much as 30% for a typical 316L stainless steel [27]. During the long summer shutdowns and short maintenance windows some portions of the beampipe get exposed to air and the SEY of those regions might increase dramatically.

The uncertainties in the beam quality and the condition of the vacuum chambers make it hard to give a quantitative description of the electron cloud based on the observations of beam dynamics. Nevertheless, the measurements of beam dynamics can reveal the physics behind the instability and provide a qualitative description of the phenomenon.

2.2 Dynamics of the unstable beam

In this section we present the results of a series of beam dynamics measurements of the unstable beam at Recycler. We discover a number of features, unique to the electron cloud instability, such as the highly nonlinear dependence of the instability increment on the beam intensity and the gradual increase of the instability threshold over the course of the machine operation.

2.2.1 Peculiar features of the instability

The fast instability affects the motion in the horizontal plane only, its occurrence in the vertical plane has never been seen. The vertical motion, however, is still affected by the instability because of the coupling between the vertical and the horizontal degrees of freedom (Fig. 2.4). The coupling arises from the close position of the transverse betatron frequencies: the fractional tunes are close to 0.4 and differ by 0.05. As the instability progresses, the beam starts hitting the physical aperture. Typically, several percent of the beam is lost due the fast instability (Fig. 2.5), but in severe cases the losses may exceed 25%, and then the control system extracts the beam into the beam dump to prevent the excessive irradiation of the ring tunnel. As the beam loses charge and its effective emittance increases due to the betatron oscillations ($\varepsilon_{eff} \propto A^2$) the transverse tampers can start suppressing the oscillations, stabilising the beam (Fig. 2.4). It is important to note that although in this case the beam is not lost, its intensity decreases significantly during the instability. With the transverse dampers off, the unstable

beam is usually kicked out of the machine by the safety interlock within 500-1000 revolutions due to high losses.

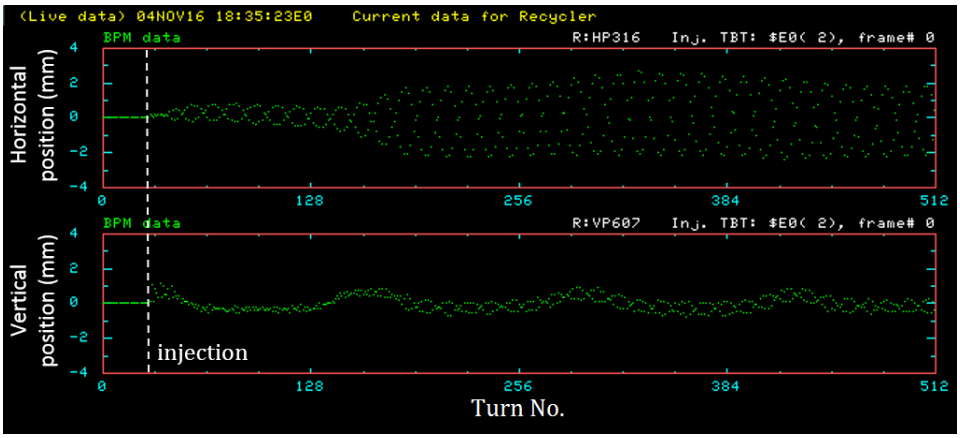

Figure 2.4: The fast blow-up of beam centroid oscillations is observed only in the horizontal plane. Turn-by-turn measurement of beam position of 1 batch after its injection into Recycler.

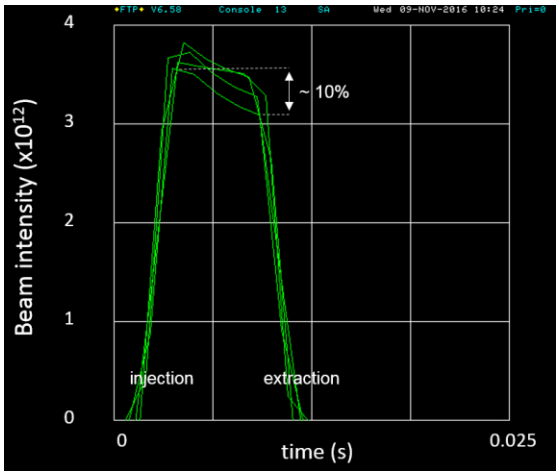

Figure 2.5: In a severe case 10% or more of the beam intensity can be lost within 0.01 s after the injection. Beam: 1 batch, 80 bunches, initial total intensity 3.7×10^{10} p. The variance in the initial intensities is caused by slightly different losses in the MI-8 injection beamline and the insufficient sampling frequency of the beam intensity monitor – only 720 Hz.

In an experiment, the beam becomes unstable when its bunch length shrinks (Fig. 2.6) due to quadrupole oscillations of the bunch length. During the longitudinal squeeze the betatron oscillation amplitude increases by several mm in 20-30 revolutions and then stays constant until the next bunch compression. The oscillations of the bunch length appear because of the longitudinal injection mismatch and insufficient Recycler RF voltage. The amplitude of the oscillations can be increased manually by adjusting the Booster bunch rotation. Normally, the amplitude of oscillations of the peak intensity (which is inversely proportional to the bunch length $I_{peak} \sim 1/\sigma_z$) is of the order of 10% and can be as high as 30%.

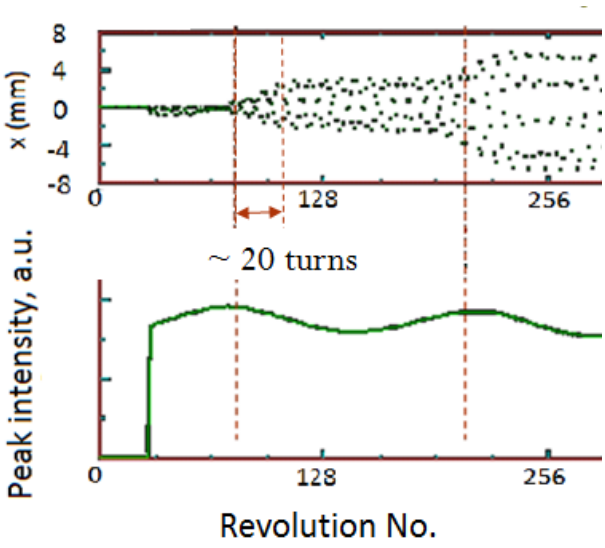

Figure 2.6: The beam becomes unstable horizontally when its bunch length shrinks due to synchrotron oscillations and its peak intensity increases. Top – turn-by-turn BPM measurement of the beam centroid position, bottom – turn-by-turn measurement of the peak beam intensity.

A stripline measurement reveals the internal structure within the unstable beam. We injected one batch of 5×10^{10} ppb with the transverse feedback system off, so that its interference did not change the characteristic modes and their frequencies, and adjusting the Booster bunch rotation to increase the oscillations of the bunch legth. The results are shown in Fig. 2.7. After the beam compresses

longitudinally large betatron oscillations (over 3 rms beam sizes) appear in the tail of the batch. The amplitude of this oscillations remains roughly constant until the beam compresses longitudinally one more time, half a synchrotron period, or about 200 revolutions, later. Then the betatron amplitude significantly increases again and the whole batch becomes unstable. One can notice that between the turns 50 and 200 the oscillations of the head of the bunch train, bunches no. 0-10, start to increase, while bunches directly after them, no. 10-15, remain stable. This may be an indicator of a presence of a long-term memory in the system – the tail of the batch affects the motion of the head on the next revolution. A similar measurement in the vertical plane shows no blow-up, triggered by the bunch length contraction. Due to the coupling between the horizontal and vertical degrees of freedom the vertical oscillations do gradually increase though after the beam becomes unstable horizontally, and their amplitude stays below ~ 1 mm.

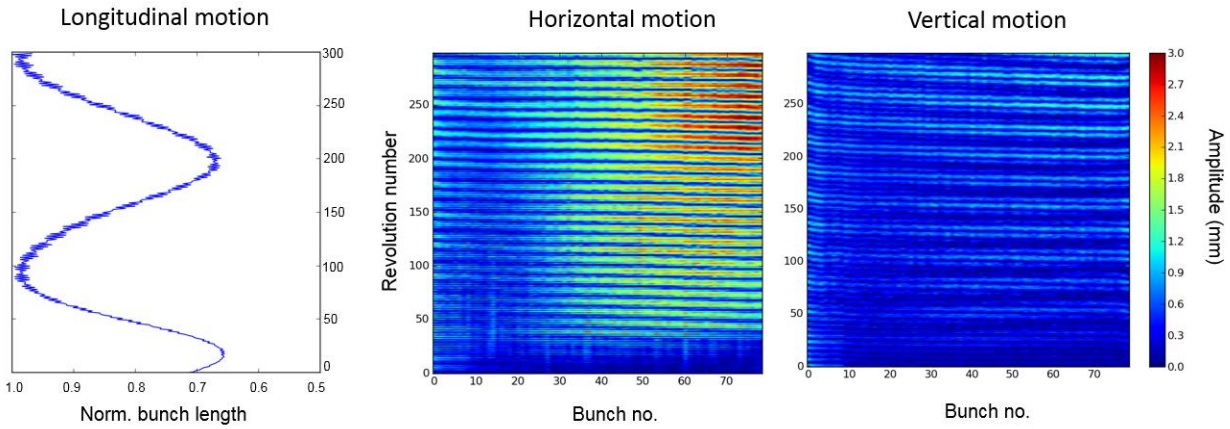

Figure 2.7: The instability mostly affects the last bunches in the train. It starts after the beam compresses longitudinally (left) and then becomes more severe after it compresses again, half a synchrotron period later. The color depicts the amplitude of the horizontal betatron oscillations of the beam center of mass as a function revolution number and position within the batch. The horizontal stripes a caused by our sampling of beam position once a revolution and appear at twice the betatron frequency: $2Q_x = 0.9$ or 1/10 turns. The data was gathered over 300 revolutions with the transverse dampers off. Beam: 1 batch, 80 bunches, 5×10^{10} ppb.

A relatively low chromaticity is needed for the instability to occur. No instability has been observed at the horizontal chromaticity $\xi_x = -10$ or higher at the current operational intensity of 5×10^{10} ppb. Typically, the chromaticity of about $\xi_x = -6$ or lower is required to induce the instability. The disappearance of the instability at a high chromaticity is expectable, since it creates a chromatic betatron frequency spread $\Delta Q_x = |\xi_x|\sigma_p$ leading to the Landau damping of collective motion (discussed in more detail in Sect. 5.1).

The lower chromaticities are beneficial for the single particle stability, since the chromaticity provides coupling between the transverse and longitudinal degrees of freedom. The strengths of synchro-betatron coupling resonances decreases with the chromaticity, leading to larger dynamic aperture, and beam lifetime. Currently, the ring operates at the moderate chromaticities of $\xi_{x,y} = -5, -7$ during the first stage of slip stacking, and this is where the instability can be most dangerous.

Finally, a peculiar feature of the instability is its selectivity – it only affects the 1st injected batch above the threshold intensity; the subsequent injections of the same intensity are not affected (Fig. 2.8). This feature cannot be explained from the standpoint of a conventional resistive wall instability, where the wake-fields beam intensity (see, for example, Table 2.2 in [37]) Hence, for the resistive wall one would expect a the instability to become more potent as more beam is injected into the machine. The stability of the last injections can be explained by the electron cloud though, since,

first, its density is a highly nonlinear function of the beam current (Sect. 4.3.6) and, second, it works as a nonlinear lens, providing an additional Landau damping.

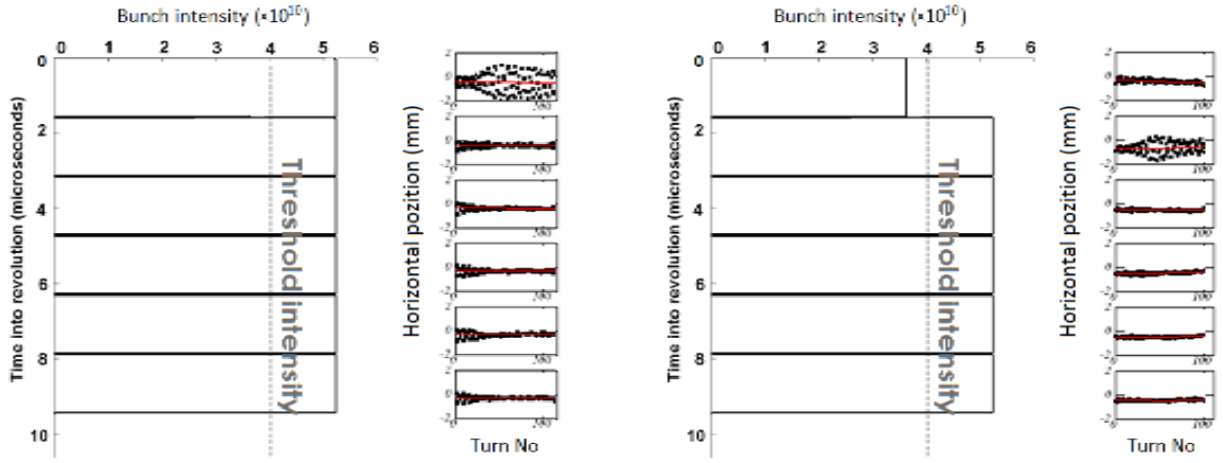

Figure 2.8: The first batch above the threshold intensity suffers the blow-up after injection into the ring. The plots show bunch intensities of six consecutive injections into the Recycler and turn-by-turn measurement of the beam center horizontal position for each injecting batch. Left – the 1st batch is above the threshold intensity of 4×10^{10} ppb and is affected by the instability, the other five batches of the same intensity remain stable. Right – the 1st batch below the threshold, the instability moves to the 2nd batch [30].

2.2.2 Intensity dependence of the instability growth rate

The growth rate of a conventional resistive wall instability scales linearly with the beam intensity. The observed fast instability, on the other side, does not follow a linear dependence (Fig. 2.9). For a beam of one batch of 80 bunches the instability does not manifest itself below the intensity of 10 turns or $4.2*10^{10}$ ppb. The instability threshold seems to be at $4.6*10^{10}$ ppb and its growth rate rapidly increases for higher intensities. The maximum growth rate is achieved at 13-14 turns or $5.4–5.8*10^{10}$ ppb, where high beam losses trigger the beam abort in less than 500 revolutions. Above $6.3*10^{10}$ ppb, however, the beam blowup starts to decrease. The beam intensity in this measurement was limited by the losses

in the Booster. The highest achieved intensity was 17 turns or $7.0*10^{10}$ ppb. At this intensity the 1 mm blowup is already barely seen on the BPMs.

Figure 2.10 shows the maximum observed betatron amplitude as a function of beam intensity with the transverse damper ON. At two intensities a beam loss was registered, for those intensities the maximum amplitude right before the loss was recorded (red dots). The width of the instability in the intensity space is quite narrow – about 1.5×10^{10} ppb. This nonlinear dependence of the beam blowup on its intensity is a characteristic feature of electron cloud driven instabilities.

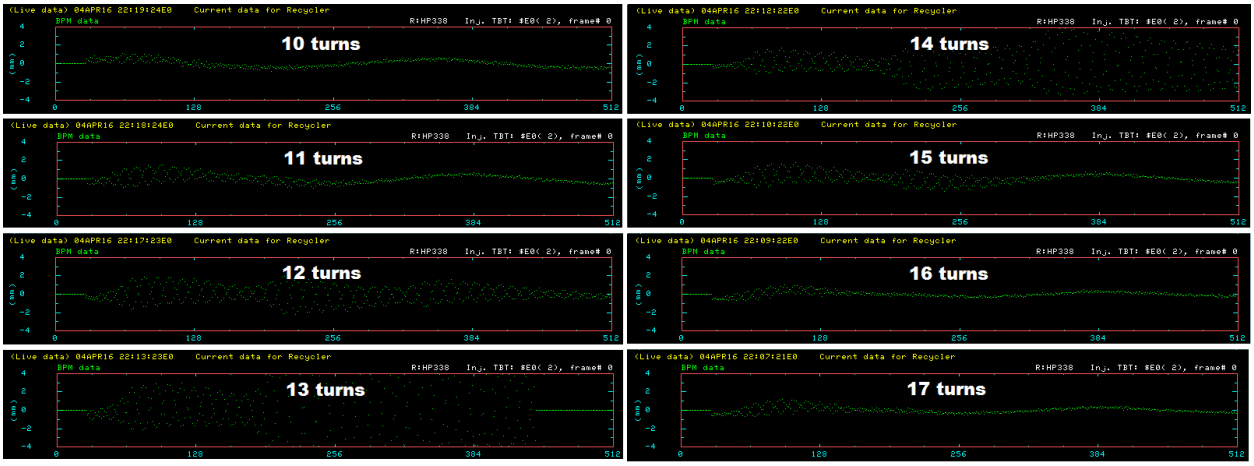

Figure 2.9: The instability goes up and then down with intensity (in Booster injection turns). Horizontal position of the beam center vs revolution number; 1 batch of 80 bunches; $\xi_{x,y}$ = -6, -8.

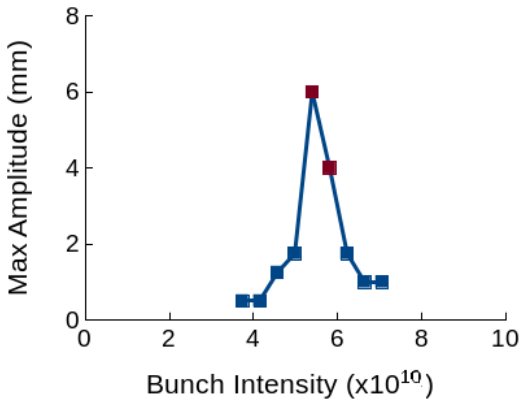

Figure 2.10: Maximum amplitude of resulting betatron oscillations has a sharp spike at the intensities around 5-6x10^{10} ppb. Red points indicate total beam loss due. Data from the Apr 4, 2016 test.

2.2.3 Conditioning during the high-intensity operation

The fast instability is most prominent during the start-up phase after a shutdown, when the vacuum in the machine is broken for ring maintenance and upgrade. As the accelerator operates the instability thresholds go up, which is consistent with a hypothesis of beampipe conditioning through scrubbing by the beam. The conditioning effect in Recycler was first mentioned by Eldred et al in 2014 [29]. At that time the threshold intensity was 4*10^{10} ppb, or 9 Booster turns. Later studies have shown the

threshold going up as the machine runs high intensity beams. After the 2015 shutdown the threshold was at $4.5*10^{10}$ and during the course of the 2015-16 operation increased to $6.3*10^{10}$ (Fig. 2.11).

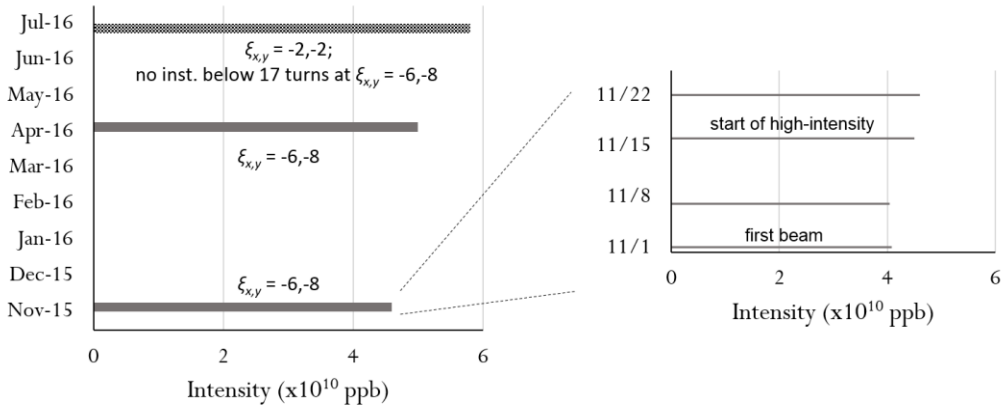

Figure 2.11: The instability threshold goes up as the machine runs high-intensity beams. Left – evolution of the threshold during the 2015-16 run; the last measurement was made at higher chromaticities – no instability observed at -6,-8. Right – conditioning during the machine start-up after the long summer shutdown in 2016. No increase of the threshold seen during the first two weeks when the machine was running low intensity (1 batch, $< 3\times10^{10}$ p).

The conditioning effect is consistent with the electron cloud nature of the instability. Recent studies by Y. Ji [27] show that the stainless steel beampipe slowly conditions when being exposed to the beam in an actual accelerator environment. The steel then rapidly deconditions after the beam is turned off [28]. During the latest run in 2016 the secondary emission yield went down by 30% from 1.95 to 1.35 in 7 months and then increased by 10% during the first two days of the deconditioning.

The peculiar features of the instability, in particular its high growth rate, the nonlinear dependence on beam intensity, and the conditioning during the high-intensity runs suggest the electron cloud nature of the instability. Its appearance only in the horizontal plane suggests that the cloud is located in the ring's dipole magnets. The Recycler dipoles are combined function magnets that have a linear focusing component in addition to the constant bending magnetic field. The presence of focusing

allows the magnets to trap the electron cloud, leading its build up over multiple revolutions (more details on this in the following chapters).

2.3 Beam stabilization by a clearing bunch

To check whether the instability is caused by the trapped electron cloud a clearing bunch test has been done. The clearing bunch technique is a method, originally developed in Cornell, which allows a detection of the trapped cloud by a special witness bunch. If a trapped electron cloud is present in the machine, a single bunch of high enough charge following the main batch, will kick it and clear the aperture. This clearing of electron cloud then can be noted by observing a change in beam dynamics.

Figure 2.12 (top) shows the increase beam center oscillations, measured by BPMs, of an unstable batch of $3.6*10^{12}$ p. The horizontal oscillations rapidly grow, leading to beam dilution and a loss of a fraction of intensity, then the beam is stabilized by the dampers. When a single clearing bunch of $\geq 1*10^{10}$ p is injected in the machine before the high-intensity batch, the later remains stable (Fig. 2.12, bottom). The position of the clearing bunch does not change the picture – it can be as far as half of the ring (or ~ 5 μs) apart from the batch, suggesting that there is a portion of the electron cloud that survives over one revolution, and it can be removed with a clearing bunch. Further increase of the clearing bunch intensity does not change the picture – the high-intensity batch remains stable. This agrees qualitatively with the simulation of electron cloud build-up and trapping in Recycler dipoles, discussed in Sects. 4.1, 4.2.

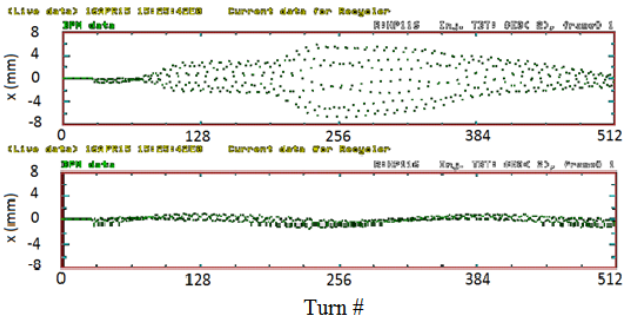

Figure 2.12: Without the clearing bunch the beam of $3.6*10^{12}$ p blows up in about 20 turns (top); with the clearing bunch of $1*10^{10}$ p it remains stable (bottom).

Figure 2.13 depicts the betatron tune shift within the 80-bunch train with respect to the first bunch, measured over 600 revolutions with a stripline detector, with the dampers off during the measurement. Since the space charge does not change the coherent tune and the resistive wall creates a negative tune shift, the positive horizontal tune shift is a clear signature of the presence of a negative charge at the beam center. The vertical tune shift is negative, indicating that the maximum density of the cloud is outside the beam. When a clearing bunch is added, the tune shifts decrease, indicating, as expected, a reduction of electron cloud density.

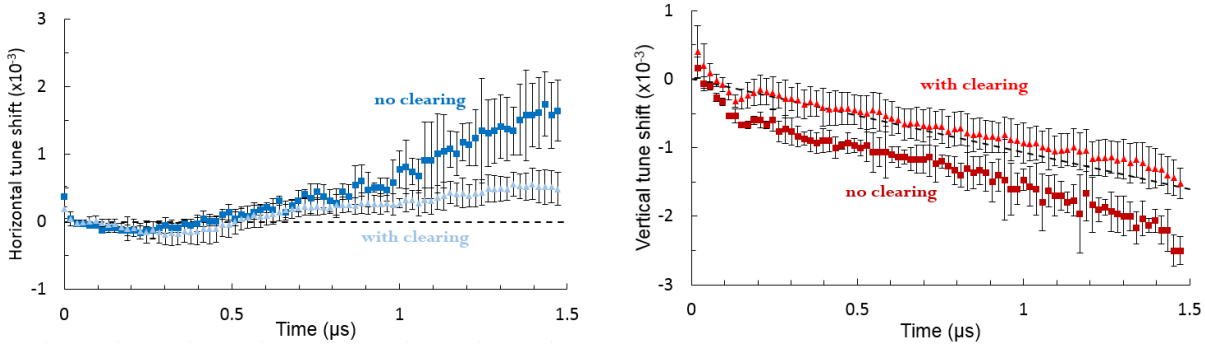

Figure 2.13: Presence of the clearing bunch reduces the tune shift between the head and the tail of the high-intensity bunch train: $5*10^{10}$ ppb, 80 bunches. The error bars represent the spread between different measurements. The black dotted lines represent the resistive wall tune shift.

There is a second effect that can affect the coherent betatron frequencies – the finite resistivity of the walls of the vacuum chamber (or "resistive wall"). It creates negative horizontal and vertical tune shifts, which scale linearly with the total charge (or bunch number in the batch). The resistive wall may be responsible for the remaining slope in the vertical tune shifts. According to the recent measurements, in Recycler the vertical resistive wall impedance is at least five times larger than the horizontal [38]. In order to account for the resistive wall contribution we performed a series of stripline measurements at lower intensities, where the fast instability is not observed. Thanks to the highly nonlinear dependence of the could build-up on intensity (see Sect. 4.3), the electron cloud density below the threshold is negligible compared to one above. Therefore the betatron frequency shift observed below the threshold is created only by the resistive wall. The frequency shift between the first and the last bunches of the batch scales linearly with intensity for a stable beam below the threshold (Fig. 2.14). This linear dependence can be used to estimate the resistive wall contribution to the total tune shift above the threshold intensity and separate the electron cloud part. The dashed lines in Fig. 2.13 represent the frequency shift due to the resistive wall.

Taking the resistive wall effect into account we see that the insertion of a clearing bunch completely removes the shifts of both horizontal and vertical betatron frequencies, confirming that the shifts are caused by the electron cloud. The electron cloud be sufficiently long-lived in order for the clearing bunch to affect it. This long (~ 1 μs) lifetime suggests that the cloud must be confined by magnetic field of beam optics magnets.

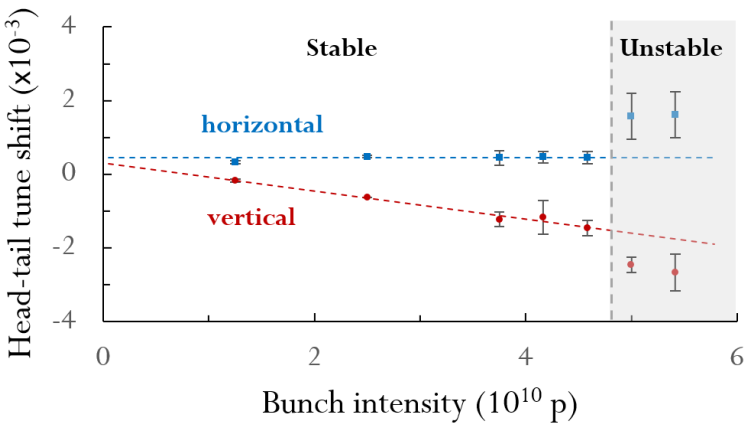

Figure 2.14: The resistive wall contribution of the head-tail tune shift scales linearly with the beam intensity. The slope is horizontal ($< 0.1/10^{10}$ p) in the horizontal plane and $\sim 0.4/10^{10}$ p in the vertical. The resistive wall part of the tune shift of an unstable beam above the threshold (grey area) can be found by extrapolation. The small positive offset (non-zero shift at zero intensity) is probably caused by the injection mismatch of the leading bunches due to the finite rise time of the injection kickers.

To sum it up, an addition of a low charge clearing bunch can stabilize a high-intensity beam. The stabilization proves the electron cloud nature of the instability and suggests that the cloud must be trapped in the beam optics magnets. The observed bunch-by-bunch shifts of the betatron frequencies and their reduction by a clearing bunch are consistent with the electron cloud picture.

2.3.1 Possible operational implementation of electron cloud clearing

It has been previously shown that only the first batch above the threshold intensity suffers from the fast instability, while the subsequent batches remain stable. If the first batch can be stabilized by a clearing bunch, injected before it, then all beam should remain stable. To confirm this idea a proof-of-principle experiment has been done on April 04, 2016.

In the proof-of-principle clearing experiment a clearing bunch of $4.2*10^{10}$ p was first injected. Then, in the next three injection cycles three high-intensity batches of $5.8*10^{10}$ ppb (14 Booster turns)

were injected in the ring (Fig. 2.15). The first four injection cycles of an actual 4+6 slip-stacking machine state were used in this test to simulate the real operation. Since the first cycle was occupied by the clearing bunch we were limited by only three high intensity batches.

Without the clearing bunch the 1st batch is unstable, as seen before in [29], and the 2nd and 3rd batches remain stable. With the clearing bunch all beam remained stable with no fast instability observed (Fig. 2.16).

In order to save an injection position in the ring the clearing bunch can be kicked out before the injection of the 2nd or 3rd batches, and the beam still remains stable. This way the clearing bunch does not need an extra position in the ring. In Figure 2.17 the bunch is extracted by the gap clearing kickers and the second high-intensity batch takes its place; the beam remains stable.

The clearing bunch can be placed at almost any position in the ring, arbitrarily far from the beam it is supposed to stabilize. Empirically it has been established that the bunch should not be place closer than 5-7 RF buckets in order for the stabilization to happen. This is probably due to the presence of decaying unconfined shortly after the beam has passed. When that cloud decays and only the trapped particles are left the pilot bunch can clear the aperture. According to the numerical build-up simulations (discussed in detail in the Chapter 4), the untrapped cloud decays in about 10 RF cycles, which is consistent with the above hypothesis.

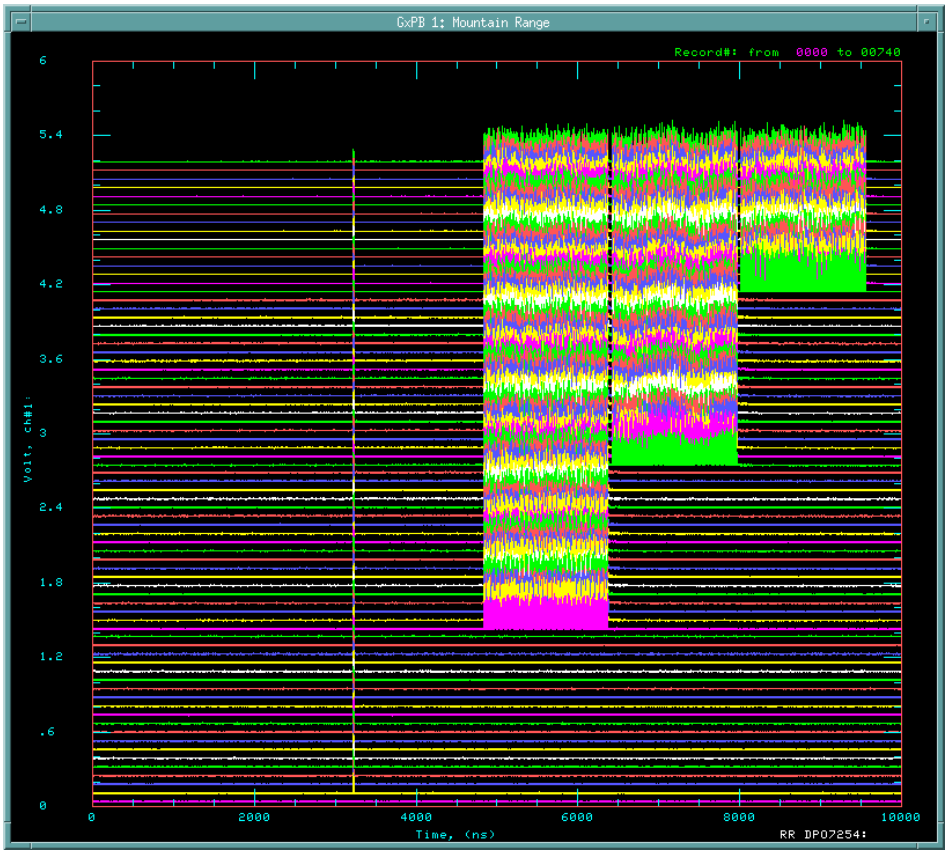

Figure 2.15: Positions of the clearing bunch and three high-intensity batches. The horizontal axis shows bunch position in the ring in nanoseconds, the vertical – time into the machine cycle, the separation between the horizontal lines is 300 revolutions (3.3 ms).

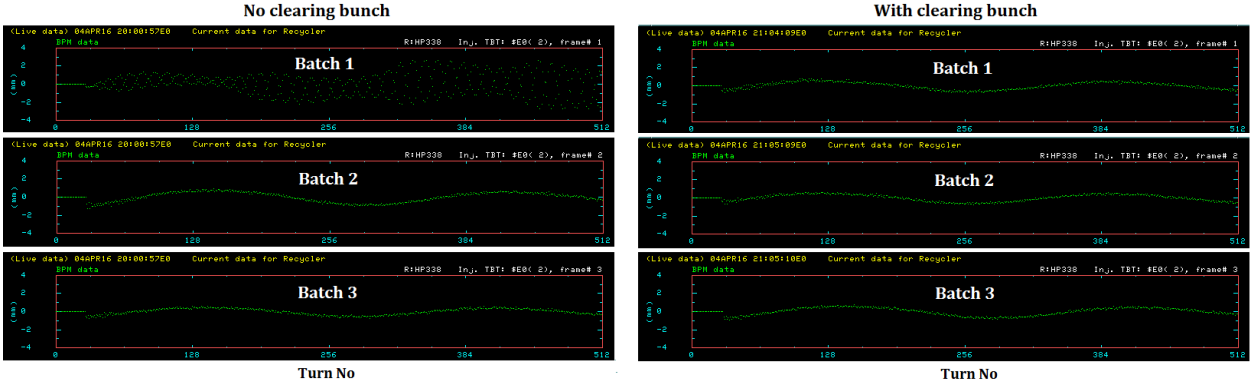

Figure 2.16: Without the clearing bunch the 1st batch is unstable, with the clearing bunch all beam is stable. Horizontal position of the beam center is plotted vs number of revolutions after its injection. Beam: $5.8*10^{10}$ ppb.

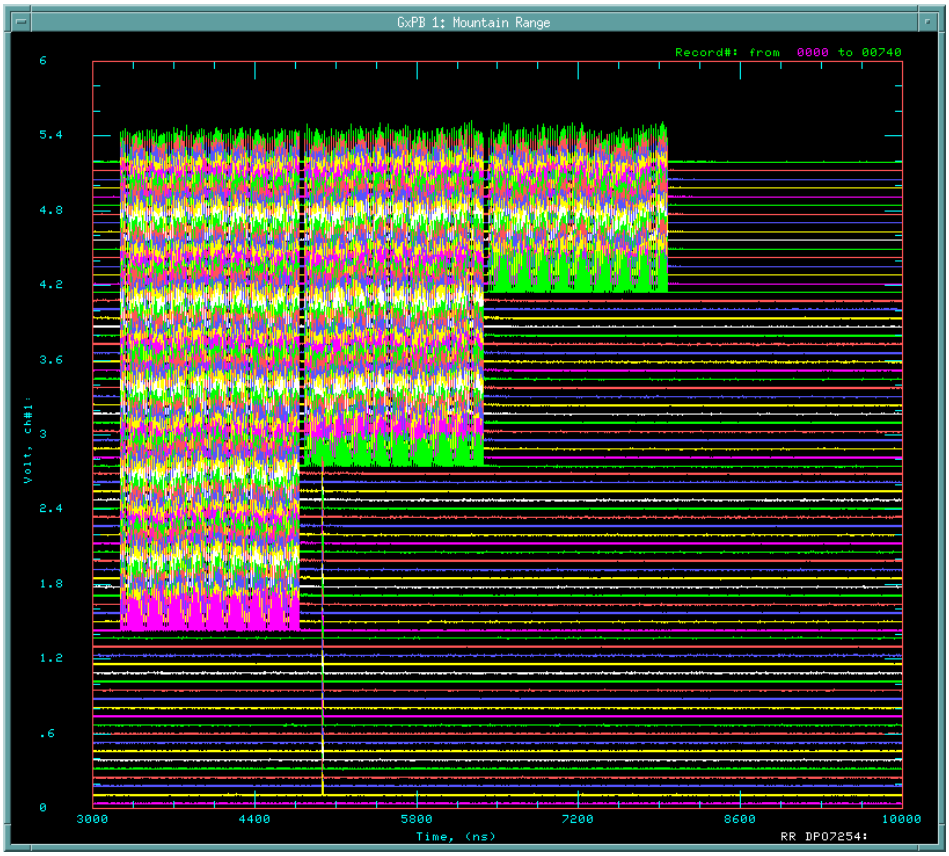

Figure 2.17: The clearing bunch (the single spike) stabilizes the first high-intensity batch; it is then thrown away and the second and third batches are injected. No fast instability is observed in any of the batches. The horizontal axis shows bunch position in the ring in nanoseconds, the vertical – time into the machine cycle, the separation between the horizontal lines is 300 revolutions (3.3 ms).

The main disadvantage of the described approach comes from the way how the clearing bunch is created. In order to achieve a single bunch in the Recycler its injection kickers and Booster extraction kickers are mistimed in such a way that 79 of 80 Boosted bunches go to the beam dump and only the first one gets injected into the ring. This procedure leads to a waste of the whole Booster cycle and unnecessary contamination of the beam dump and therefore is unpractical.

A possible solution could be an installation of a fast notcher to kick out several bunches from the tail of the first batch, creating the desired batch-clearing-bunch beam pattern. This can done on an early stage of acceleration in the linac, when the radiation damage from bunches sent to the beam

dump is minimal. This procedure does not require a separate injection Booster cycle for the clearing bunch, since the clearing bunch and the first batch are injected simultaneously. Only the first batch needs to be notched and only 7-10 bunches need to be removed, so the loss of 10-12% of beam intensity due to the creation of the clearing bunch is outweighed by the ability to work above the threshold.

CHAPTER 3

MICROWAVE MEASUREMENT OF THE CLOUD DENSITY

A microwave technique provides a non-invasive measurement of the electron cloud density and its evolution during an accelerator cycle. It is based on detecting a phase modulation of a microwave, propagating through the cloud. The method was initially proposed for measuring the cumulative average density of the electron cloud, which can vary significantly along the beampipe depending on local geometry and surface conditions, over a large section of an accelerator [39]. It proved to be valuable for studying the clouds at many large scale high intensity accelerators: MI at Fermilab [40], CESR at Cornell [41], PS and SPS at CERN [42], etc. The technique is also useful for measuring the cloud in the regions where an installation of a pick-up detector is technically challenging, for example inside the magnets.

The first attempt to perform a microwave measurement in Recycler was made Eldred et al. in 2014 [29]. The researchers used standard stripline beam position monitors to transmit the 2.0 GHz carrier signal ~ 50 m of Recycler beampipe. The studied section of the ring had several combined function dipoles, corrector quadrupoles and sextupoles, and drift sections. The spectrum of the received signal showed a characteristic spike in the modulation sideband, occurring simultaneously with the injection of an unstable batch (Fig. 3.1). That result allowed confirming the electron cloud hypothesis on the physics behind the instability. High noise and low signal level in the experiment limited its temporal resolution and did not making a reliable measurement of the density of the cloud. It was suggested that the electron cloud must be located in the dipoles, since the previous studies of the electron cloud in a similar MI beampipe did not predict a high cloud density in the drifts, and the occurrence of the fast instability only in the horizontal plane, which is typical for an instability, driven by an electron cloud in the dipole magnets. Because of the large spacing between the antennas, the exact origin of

the signal remained unknown [30]. To resolve the location uncertainty and improve the temporal resolution a new attempt has been made.

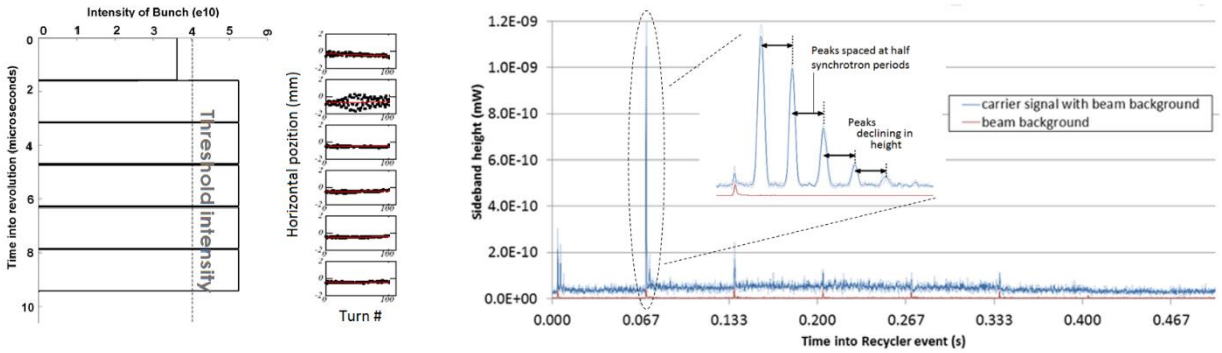

Figure 3.1: Left – the first batch above the threshold intensity suffers the blow-up after injection into the ring. Right – a phase modulation of the 2.0 GHz carrier at the revolution frequency of 90 kHz occurs simultaneously with the instability. The fine structure of the modulation sideband implies that it is connected with the longitudinal quadrupole oscillations that have a periodicity of a half of the synchrotron period [30].

In this chapter we describe the electron cloud experimental test setup at Recycler: its hardware, principles of operation, expected results, and limitations. Then we present the analysis of the noise that limits the precision of the microwave measurement, which turned out to be the beam Schottky signal. Finally, we present the results on the density of the electron cloud in a Recycler combined function magnet, its build-up and decay.

3.1 Experimental setup

In order to measure the cloud density inside a combined function magnet, we installed the source and receiver directly upstream and downstream of the dipole. This way we can isolate we origin of the electron cloud signal – if it is observed it is guaranteed to come from that magnet. The close location

of the antennas allowed greatly reducing the time of flight compared to the previous attempt [6] and hence enhancing the temporal resolution.

3.1.1 Hardware

A layout of the experiment is depicted in Fig. 3.2. All the electronics is located at the MI-50 service building. We generate a 1.97 GHz carrier with a signal generator and then amplify it with a 10 W preamplifier before sending it to the tunnel. In the tunnel, we are using two regular Recycler vertical BPMs to send and receive the TE microwave signal. The choice BPMs as antennas was made because of their availability and the time constraints of the project. To account for the cable losses in a 100 m cable run from MI-50 to the location of the test setup in the tunnel we are using an additional 1 W amplifier, sitting next the sender BPM. The amplifier is protected from interference with the reflected signal and the beam signal by a 1-2 GHz circulator, which sends them to a 5 W 50 Ω resistive load. The microwave travels about 5 m through a combined function magnet. The electron cloud, if present in the magnet, delays the propagation of the microwave, modulating its phase. The microwave signal is then picked up by the second BPM. The received signal, first, goes through a narrow band filter to reduce the interference from the beam signal and then is amplified and sent to the 20 GS/s oscilloscope. The oscilloscope is triggered by a beam-synchronized trigger. It measures the phase delay between the generated and the received signals, which is then converted into the density of the electron cloud inside the magnet.

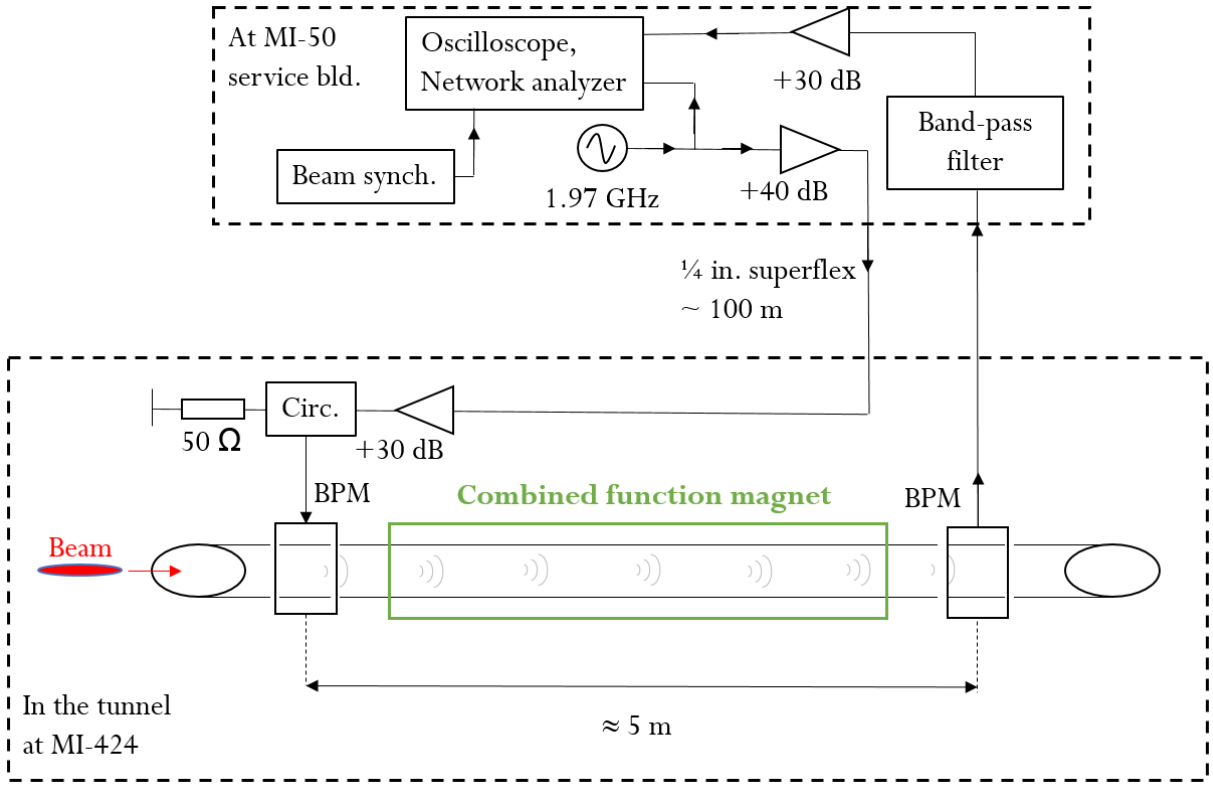

Figure 3.2: Layout of the microwave measurement setup

3.1.2 Physical principle

One can consider the electron cloud inside a magnet as a cold collisionless magnetoactive plasma. Generally, the propagation of a microwave through the plasma depends on its polarization with respect to the external magnetic field. In a uniform magnetic field $\mathbf{B_0}$ the dielectric tensor $\varepsilon_{a\beta}$ can be reduced to two components, $\varepsilon_{\parallel}$ and $\varepsilon_{\perp}$, where the subscript stands for the orientation of the electric field $\mathbf{E}$ of the RF wave parallel or perpendicular to $\mathbf{B_0}$. Assuming the electron density is much larger than the ion density, $n_e \gg n_i$ one can write [24]

$$\begin{aligned} \varepsilon_{\perp} &= 1 - \frac{\omega_{pl}^{\,2}}{\omega_{rf}^{\,2} - \omega_B^{\,2}} \\ \varepsilon_{\parallel} &= 1 - \frac{\omega_{pl}^{\,2}}{\omega_{rf}^{\,2}} \end{aligned}, \qquad (3.1)$$

where $\omega_{pl} = \sqrt{4\pi n_e r_e c^2}$ is the plasma frequency, $\omega_{rf} = 2\pi f_{rf}$ is the RF frequency, and $\omega_B = \frac{eB_0}{m_e c}$ is the Larmor frequency; e and m_e are the electron charge and mass, r_e – classical electron radius. For the Recycler magnets B_0 = 1.38 kG and $\omega_B = 2\pi \times 3.72\text{GHz}$ (Table 3.1).

A $\mathbf{E} \perp \mathbf{B_0}$ (horizontally polarized) can be resonantly absorbed at $\omega_{rf} \sim \omega_B$. The high value of ω_B makes such a measurement technically challenging at Recycler. At lower frequencies the electron contribution to $\varepsilon_\perp$ is negligible. For a TE wave with $\mathbf{E} \| \mathbf{B_0}$ (vertically polarized) the deviation of $\varepsilon_\|$ from the unity is linear with the electron density n_e and does not depend on the magnetic field strength B_0. For the typical electron cloud densities < 10^7 cm^{-3} it is quite small, of order or less than 10^{-4}.

A TE wave propagating in a waveguide filled with vacuum has a group velocity of

$$v_{g,vac} = c\sqrt{1-(\omega_{\text{cutoff}} / \omega_{\text{rf}})^2} \tag{3.2}$$

where $\omega_{cutoff} = 2\pi f_{cutoff}$ is the cutoff frequency of the waveguide, corresponding to the TE_{10} mode. The electron plasma changes the dielectric constant of the medium, and consequently the group velocity. For a vertically polarized wave $v_{g,pl} = v_{g,vac} / \sqrt{\varepsilon_\|}$. Assuming the beampipe in the combined function is uniformly filled with the cloud, the resulting phase delay is

$$\Delta\varphi(n_e) = \omega_{rf} L_m \times \left(\frac{1}{v_{g,vac}} - \frac{1}{v_{g,pl}(n_e)} \right) \approx \frac{L_m \omega_{pl}(n_e)^2}{2 v_{g,vac} \omega_{rf}} \propto n_e, \tag{3.3}$$

where L_m is the length of the magnet.

The temporal resolution of the experiment is limited by the time it takes the microwave to propagate through the magnet

$$\Delta t_{\min} = \frac{L_m}{v_{g,pl}} \approx \frac{L_m}{c\sqrt{1-(\omega_{\text{cutoff}} / \omega_{\text{rf}})^2}}. \tag{3.4}$$

Here we used $\varepsilon_{pl} \approx 1$. Examining Eqs. (3.3) and (3.4) one can easily notice the tradeoff between the sensitivity and the temporal resolution. On one hand, a lower RF frequency, closer to the cutoff of

the beampipe, increases the measured phase delay for a given cloud density. On the other hand, the lower the frequency – the higher the propagation time. To resolve the dynamics of electron cloud build-up one needs to have a temporal resolution comparable with the bunch spacing. For Recycler that means $\Delta t_{\min} < 100$ ns. For this experiment we chose $f_{rf} = 1.97$ GHz, it was then fine-tuned to reduce the noise (see Sect. 3.2). Table 3.1 summarizes the key physics parameters of our set-up. For an electron cloud density of ~10^6 cm^{-3} we would expect to see a signal of 0.35 deg.

Table 3.1: Key physics parameters of the set-up

Parameter	Symbol	Value
Length of the dipole	L_m	4.5 m
Magnetic field	B_0	1.38 kG
Larmor frequency	f_B	3.72 GHz
Cutoff frequency	f_{cutoff}	1.87 GHz
RF frequency	f_{rf}	1.97 GHz
Group velocity	$v_{g,vac}$	0.3c
Temporal resolution	$\Delta t_{\min}$	50 ns
Sensitivity	$d\perp\varphi/dn_e$	6 mrad/(10^6cm^{-3})

3.1.3 Signal transmission

There are two major sources of signal losses in the experiment: signal reflection due to imperfect coupling of the BPM and cable losses. The attenuation of the microwave during its propagation through the beampipe is insignificant.

The signal reflection losses are caused by the design of the BPMs, which were not intended to be used as launch pads for microwaves. The BPMs have a 50 Ω, matched to the cables, only at low frequencies. Near 2 GHz, however, most of the incoming signal is reflected back. To estimate the contribution of this part of the losses, we assembled a test stand, consisting of two BPMs – a source

and a receiver, located at the ends of a 1-m-long beampipe. By a careful choice of the working point one can achieve the total attenuation in the range of 20-30 dB (Fig. 3.3). This measurement also gave us the cutoff frequency of the beampipe f_{cutoff} = 1.87 GHz (measured at -60 dB).

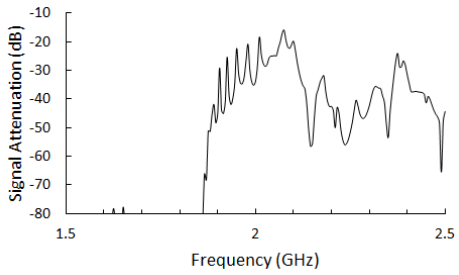

Figure 3.3: The BPMs reflect most of the power back at 2 GHz. The total transmission loss due to reflection is 20-30 dB. Beampipe cutoff frequency is 1.87 GHz.

The major portion of the losses happens in the cables. We used ¼ in. superflex heliax cables, mainly due to their availability, which have a high attenuation above 1 GHz. It is rated at 28.5 dB/100m signal attenuation at 2 GHz. We lose about 30 dB on the way from the preamplifier, located upstairs at the MI-50 service building, to the BPMs in the tunnel and another 30 dB on the way back. To account for the losses on the way forward we installed an additional 30 dB amplifier in the tunnel, next to the BPMs. The losses on the way back seem to be unavoidable. Due to high radiation in the tunnel it is impossible to install the sensitive electronics like an oscilloscope downstairs. A down-conversion might improve the signal attenuation but requires an installation of high power bandpass filters (like cavity-type filters) to protect the mixer from the low frequency high peak power components of the coherent beam signal.

3.2 Schottky noise

An investigation of the noise spectrum in the measurement revealed that it is a Schottky signal induced by the beam, which has a random component due to its large but finite number of particles [43]. The characteristic feature of the Schottky signal is the linear increase of its bandwidth with the frequency. This increase makes performing a microwave measurement a challenging task. In this section we briefly describe the physics behind and the structure of the Schottky signal and then show how we choose the microwave frequency to minimize the interference.

3.2.1 Noise spectrum

The Schottky signals are a powerful tool of beam diagnostics of coasting and bunched beams, and the power spectrum of these signals is well known. In this section we present a simple analysis of the spectrum of, first a coasting beam, and then a beam bunched by a linear RF voltage. The main conclusions, however, hold true for a beam bunched by an arbitrary wave-form stationary RF voltage [44].

Consider, first, an unbunched beam, travelling through a pick-up. The current of the k'th particle can be written as

$$i_k(t) = \frac{e}{T_0}\sum_m \delta(t - t_k - mT_0), \tag{3.5}$$

where t stands for the time, $t_k = T_0\varphi_k$ is its initial phase of the k'th particle, m is the revolution number, T_0 – revolution period, and δ is the Dirac delta-function. Applying a Fourier expansion to i_k we get

$$i_k(t) = ef_0 \sum_{n=-\infty}^{+\infty} e^{in(2\pi f_0 t - \varphi_k)}, \tag{3.6}$$

where $f_0 = 1/T_0$ is the revolution frequency. Thus the spectrum of the k'th particle is a series of delta-functions with a period of f_0 (Fig. 3.4, top). Another, l'th particle may have a slightly different

revolution frequency f_1 due to a different energy. The frequency shift Δf relates to the relative momentum difference $\Delta p/p$ as

$$\Delta f = f_0 \eta \Delta p / p , \tag{3.7}$$

where η is the momentum compaction factor. Adding up all the particles in the beam we obtain the total beam current $I(t) = \sum_k i_k(t)$. Its average value is $I_0 = \langle I(t) \rangle = e f_0 N$, where N is the total number of particles in the beam. The average power of the beam signal is proportional to $\langle I(t)^2 \rangle$:

$$\langle I(t)^2 \rangle = \int_0^T e^2 f_0^{\,2} \sum_k (\sum_n e^{ih(2\pi f_0 t - \varphi_k)})^2 dt \ . \tag{3.8}$$

Assuming a random distribution of the initial phases, Eq. (3.8) reduces to a sum of a series of periodic bands around the harmonics of the revolution frequency with an rms width proportional to the rms momentum spread σ_p (Fig. 3.4, bottom):

$$\langle I(t)^2 \rangle = \sum_n 2e^2 f_0^{\,2} N = \sum_n I_n^{\,2} \tag{3.9}$$

The average total beam power in each band is the same, it is equal to

$$I_n^{\,2} = 2e^2 f_0^{\,2} N = 2e f_0 I_0, \tag{3.10}$$

where N is the number of particles and I_0 is the beam current.

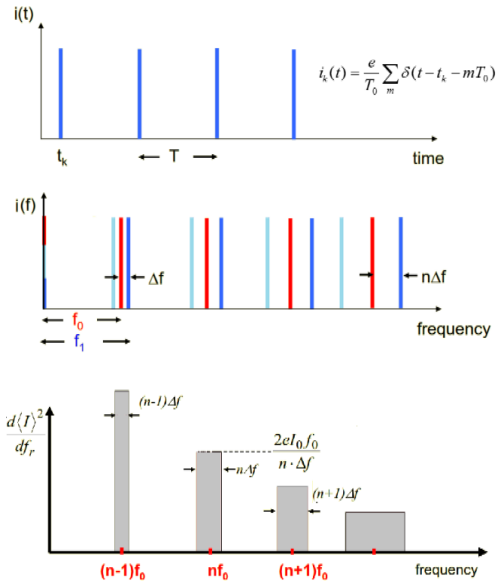

Figure 3.4: Single particle current (top) and spectrum (middle) are series of periodic delta-functions. When all the particles in the beam are added together, the resulting spectrum gets broader with frequency (bottom) [45].

In a bunched beam in addition to the cyclotron motion each particle undergoes longitudinal oscillations within its RF. Then Eq. (3.5) should be rewritten as

$$i_k(t) = ef_0 \sum_{n=-\infty}^{+\infty} e^{in(2\pi f_0 t + \theta(f_s, \varphi_k + f_s t))}, \tag{3.11}$$

where θ is the azimuthal displacement of the k'th particle from the bunch center and f_s is the synchrotron frequency. The synchrotron modulation splits each single particle spectral line into an infinite number of lines with a spacing of f_s. For a linear RF voltage the amplitudes of the lines decrease as (see Eq. (9.33) in [46]):

$$\begin{aligned} i_{k_{n,m}} &\propto J_m(\pi k_z n) \\ k_z &= \Delta z / C \end{aligned}, \tag{3.12}$$

where Δz is the span of longitudinal particle motion, C is the ring circumference, and J_h is the hth-order Bessel function.

3.2.2 Schottky noise on the Recycler BPMs

The noise signal from one of the BPM plates was measured directly with a spectrum analyzer. To remove the interference from a relatively low frequency coherent signal (main harmonic at the RF frequency 53 MHz) we used a 1.7-2.4 GHz bandpass filter. Despite the filters attenuation of 60 dB the some low frequency signal still went through, particularly at the frequencies below 250 MHz. This leakage can be explained by negligible cable losses at low frequencies (more details on cable losses are provided in Sect. 3.1.3). Despite somewhat unwanted, the low frequency signal proved to be useful for determining the nature of the noise signal.

The observed signal has all the characteristic properties of the Schottky signal described above. It appears on the harmonics of the revolution frequency, 90 kHz (Fig. 3.5). During the slip stacking, when two beams of different energies are stored in the ring, the slip-stacking sidebands appear in the signal. The 2 Hz difference in the revolution frequencies translates into a $2\text{GHz}/90\text{kHz}\times 2\text{Hz} = 45\text{kHz}$ shift at 2 GHz, putting the slip-stacking sidebands exactly in between the main peaks. At lower frequencies one can resolve the 250 Hz synchrotron frequency of the machine (the synchrotron lines merge at high frequencies as their width increases). Comparing the width of the spectral lines at 200 MHz and 2 GHz, one can easily see that it is proportional to the frequency, as expected for a Schottky signal. At 200 MHz the FWHM is 1 kHz, about 0.1 of the FWHM at the 2 GHz – 10 kHz. The rms momentum spread, estimated from the width of the spectral lines

$$\frac{\Delta p}{p} = \frac{\sigma_f}{f}\frac{1}{\eta} \sim \frac{5\text{kHz}}{2\text{GHz}}\times 115.3 \sim 2.9\times 10^{-4} \tag{3.13}$$

agrees with the tomography measurement of 3.3×10^{-4}. The 10% discrepancy in the result can be attributed to a rough method used to estimate the rms frequency spread σ_f: we estimated it as ½ of the linewidth at -5 dB, or at about $e^{-\frac{1}{2}}$ of its maximum value.

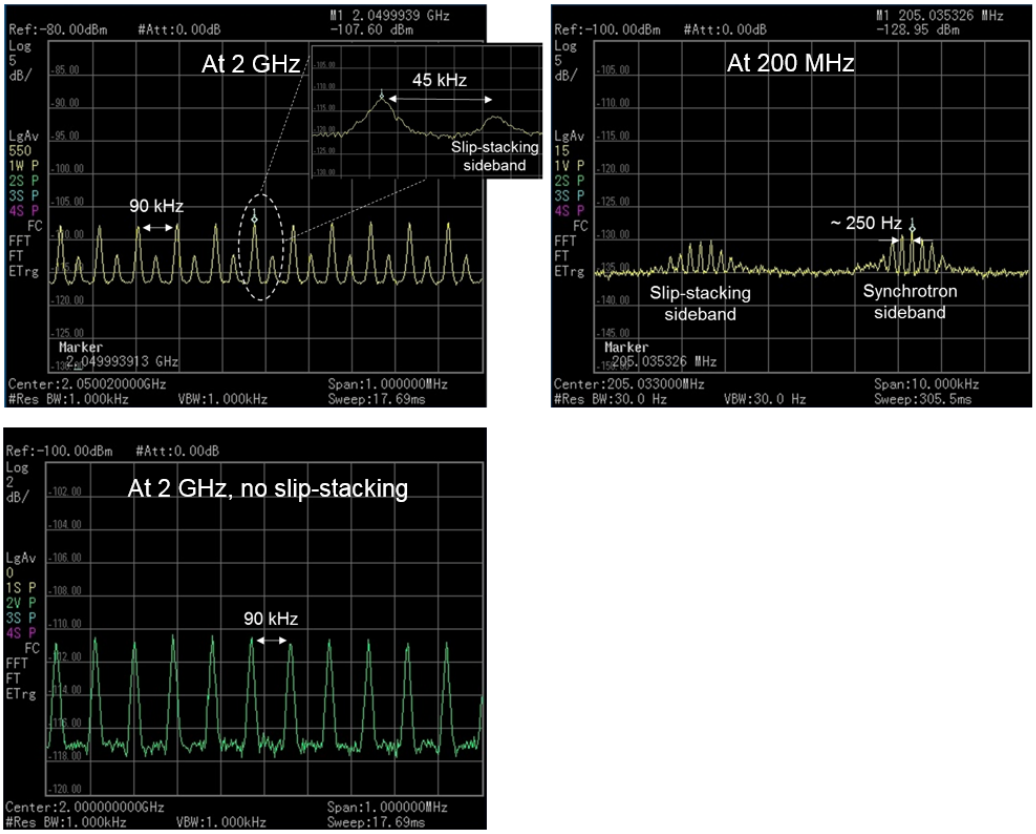

Figure 3.5: Spectrum of the Recycler Schottky signal. When the machine operates with the slip-stacking, the two beams of different energies produce signal at the revolution harmonics of ~ 90 kHz. Because of the 2 kHz difference in the frequencies, the signals separate at high harmonic numbers. At 2 GHz (harmonic number $n_h \sim 2\times10^4$) the slip-stacking signal is in the middle between the main peaks (top-left). The slip-stacking signal disappears when the machine operates with a monochromatic beam (bottom left). At 200 MHz ($n_h \sim 2\times10^3$) one can resolve the sidebands on the harmonics of the synchrotron frequency (top right). The distance to the slip-stacking sideband scales with the harmonic number: it is ~4.5 kHz at 200 MHz and ~45 kHz at 2 GHz.

The Schottky spectrum is a powerful noninvasive diagnostic tool that can reveal valuable information about the internal structure of the beam. Apart from the relevant frequencies and the momentum spread, discussed above, one can derive in a straightforward matter from the Schottky spectrum such quantities as the betatron frequency spread, chromaticity [45], and space charge

frequency shift [47]. An important parameter is the transverse emittance, which is proportional to the total power, concentrated in a betatron sideband:

$$\varepsilon \propto A_\beta \Delta f_\beta, \tag{3.14}$$

where A_β and Δf_β are, respectively, the height and width of the sideband. The power can be calibrated, using a beam of known emittance (for example using scrapers to shape the beam transversely). An attempt to show that a conventional stripline BPM can be used as a Schottky detector at high intensities is currently under way at Recycler [48].

3.2.3 Frequency selection

Despite all of its usefulness, for the purpose of the microwave electron cloud detection the Schottky signal is the noise background that has to be reduced. The power of the signal is proportional to the measurement bandwidth. We measured the power around the desired frequency 2 GHz. Before the amplification the power in a 1 MHz bandwidth is of the order of (for a typical total beam intensity of 40×10^{12} p) $P_{1\text{MHz}} \sim -80\text{dB} = 10^{-8}\text{W}$. To detect the build-up and decay of the electron cloud we need a temporal resolution of at least 100 ns, meaning at least 10 MHz measurement bandwidth and at least -70 dB of noise signal (before the amplification). Since the noise has the same frequency as the signal, it cannot be filtered out. After the final amplification the signal and noise power levels are about the same, -40 dB. The huge interference and the overall low signal level make the fast measurement did not let us doing the fast measurement.

It is possible to pick a frequency between the noise bands for a slow measurement. With a measurement bandwidth low enough to avoid both cyclotron and betatron bands one can select the microwave frequency between them and significantly reduce the interference from the beam. That can be achieved with a bandwidth up to 1-3 kHz (Fig. 3.5), resulting in a temporal resolution up to 0.3-

1.0 ms. The frequency, where one can achieve (a) a relatively high transmission, (b) a relatively low group velocity, and (c) stay away from the Schottky bands is 1.970 GHz.

3.3 Measured electron cloud density

3.3.1 Density vs beam intensity

To measure the average density of the electron cloud inside a combined function magnet during the Recycler operation a we performed a 'slow' measurement, using a network analyzer both drive the 1.97 GHz microwave and measure the phase delay. For each beam intensity 1000 measurements of the phase delay were made during a 60.2 s machine supercycle. On each supercycle the phase was calibrated during the 6 s window of no beam in the Recycler, when the Main Injector does slow-spill extraction. The lowest intensities were obtained with 6 batches in the ring. The highest intensities were measured during the 4+6 'slipstacking' operation, when the machine stores ten batches of two slightly different energies.

Averaging over 1000 data samples (limit set by the memory of our analyzer) allowed reducing the interference from the beam Schottky signal, discussed above, and resolving the small delay, presumably created by the electron cloud. For low intensities no signal was detected. For higher intensities we detected the phase delay of up to 0.5 deg, corresponding an electron cloud density of 1.5×10^{12} m^{-3} (Fig.3.6). The density increases sharply above the total beam intensity of 1×10^{13} p and then reaches a saturation, which is consistent with the simulations of electron cloud build-up discussed in Chapter 4.

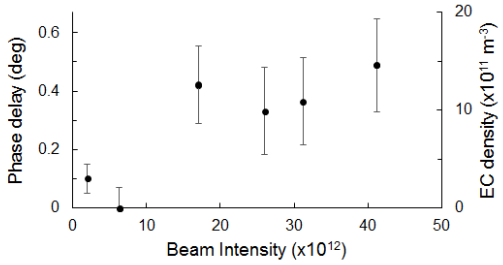

Figure 3.6: The electron cloud density increases dramatically above 1×10^{13} p total beam intensity.

It should be noted that the measured density of electron cloud is still an estimate rather than the exact value. Its calculation is based on the assumption that the cloud fills the beampipe aperture uniformly, which, strictly speaking, is not the case for a cloud in strong dipole magnetic field, as will be shown in the next Chapter. Moreover, some portions of the beampipe may be more contaminated than the others and consequently have more electron cloud in them. Nevertheless, the microwave measurement has shown the presence of the electron cloud in a combined function magnet. It can reach high densities for high-intensity beams.

3.3.1 Electron cloud decay

To measure the rate of accumulation and decay of the electron cloud we did a measurement of the phase shift during and after the passage of a batch and with a 50 ns rolling window. The short window length was determined by the bunch spacing and was required to resolve the change in the density of the cloud, which may vary significantly over a course of a few bunches. In the frequency domain the sapling window corresponded to 20 MHz bandwidth. Because of the huge bandwidth, the measurement received a lot of interference from the Schottky beam signals, discussed in Sect. 3.2. To reduce the noise we collected the data for 100 turns after the beam injection and performed averaging.

The results of this measurement are inconclusive. While we do observe some decay of the RF phase with time after the last bunch has left the magnet, and while the magnitude of the decrease is consistent with our expectations from electron cloud (Sect. 4.3.4), there is a great uncertainty in the results, resulting from the Schottky signal (Fig. 3.7). The noise signal did not disappear immediately after the beam is gone, because of the imperfect coupling of the BPM's at high frequencies. The resulting 'ringing' lasted for several hundred microsecond, spoiling the measurement.

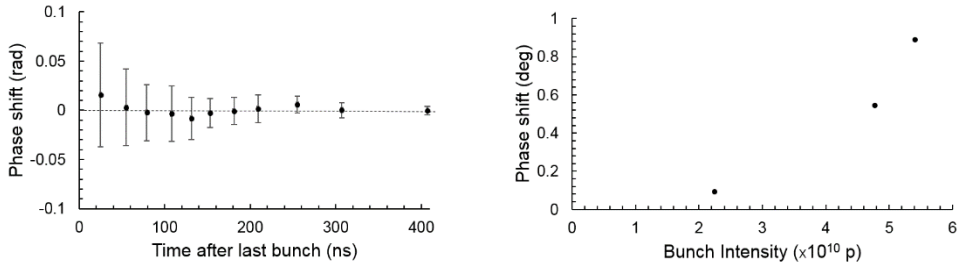

Figure 3.7: Left – the average phase shift decreases with time after the beam has left the combined function magnet; beam: 80 bunches, 5.4×10^{10} ppb. Right – the maximum phase shift, measured 25 ns after the last bunch, increases with the beam intensity; error bars not shown. RF frequency: 1.970 GHz.

The small RF phase shift makes it is challenging to perform a microwave measurement of the electron cloud density in an isolated magnet. The phase shift is limited by the wave propagation time or, in other words, by the temporal resolution of the measurement. In a fast microwave measurement the problem is further complicated by the interference from the Schottky beam signal. It is still possible to observe the decay of the cloud after the beam, and hence the Schottky noise, is gone, but one needs to design special RF launch pads, coupled at the desired frequency. The standard BPM's have high impedance at the microwave frequencies, resulting in multiple reflections of the beam induced signals.

CHAPTER 4

NUMERICAL SIMULATION

A numerical simulation allows an estimation of the density of electron cloud and the rate of the induced instability for different parameters of the problem: beam intensities, bunch lengths, and the secondary emission yield of the beampipe. A combined solution of the build-up of electron cloud and its interaction with the beam is a complex, computationally intense problem. The simulation results may vary significantly depending on the exact modelling details [18]. Because of its complexity and sensitivity to details, we approach the problem in several steps.

First, we examine analytically the process of the electron cloud trapping in a combined function magnet. We find the conditions when a fraction of the electron cloud particle is confined by the magnetic field and estimate its population and lifetime.

Then we study numerically the build-up of the electron cloud with a stationary beam. We show how the trapping affects the build-up and compare the simulation results with the analytical estimates of the electron cloud trapping and the experimental observations of the fast instability, presented in Chapter 2. Having confirmed the numerical model, we extend the studies to the higher beam intensities, planned for the PIP-II upgrade.

And finally, after the parameters of the electron cloud have been determined, we simulate the beam-cloud interaction to find the growth rate and the characteristic mode frequencies of the electron cloud driven instability.

4.1 Electron cloud trapping in a combined function magnet

4.1.1 Combined function dipole as a magnetic trap

In a combined function dipole the electrons of the cloud move along the vertical field lines. This motion conserves their energy E and magnetic moment

$$\mu = \frac{mv_{\perp}^2}{2B} = const, \tag{4.1}$$

where $v_{\perp}$ is the component of the velocity normal to the magnetic field B. As an electron moves closer to a magnet pole it sees a higher B (Fig. 4.1) and it can reflect back if

$$E - \mu B = 0 \tag{4.2}$$

Alternatively, the electron will reflect back at the point of maximum magnetic field if the angle between the electron's velocity and the normal to the field line is lower than:

$$\theta < \theta_{\max} = \cos^{-1}(\sqrt{B_0 / B_{\max}}). \tag{4.3}$$

Eq. (4.3) is a commonly known formula for a 'magnetic mirror'. Particles with angles $|\theta| < \theta_{\max}$ are trapped by the field. For Recycler magnets (Table 4.1), Eq. (4.3) gives a capture of ~10^{-2} particles of electron cloud, assuming their uniform distribution.

4.1.1 Electron capture by the field

Let us look at the process of electron cloud trapping in more detail and consider the last two bunches of the batch. The first bunch kicks the electrons of the cloud, created by the batch. With an energy of the order of 100 eV the electrons drift along the magnetic field in the vacuum chamber, finally reaching its walls and producing secondary electrons with the energies of a few eV [19]. In the absence of the beam these secondary electrons would eventually reach the aperture and die. But the next proton

bunch can stop a fraction of the secondaries, reducing their angle to $\theta < \theta_{max}$ (Fig. 4.2). These electrons will remain trapped in the magnetic field after the beam is gone.

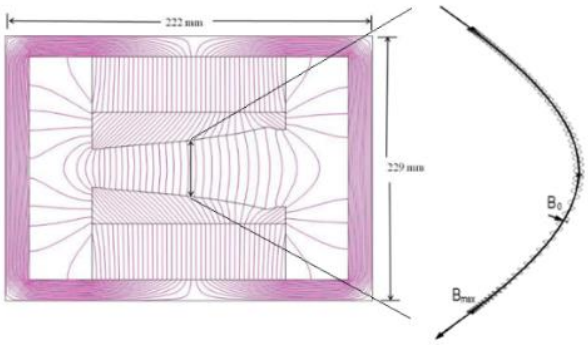

Figure 4.1: Electron cloud can get trapped by magnetic field of a combined function magnet. Cross-section of a Recycler permanent combined function dipole; the vacuum chamber is not shown.

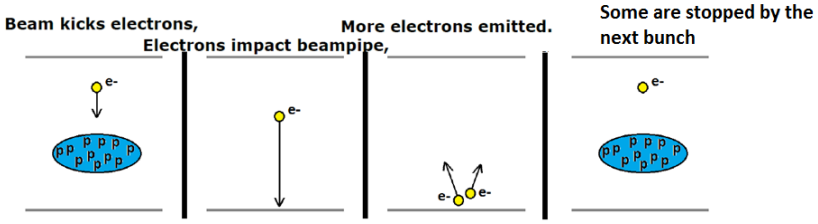

Figure 4.2: The first bunch kicks the cloud, creating secondary electrons, the second bunch stops some of them.

Thanks to the strong magnetic field the motion of an electron is essentially a 1D problem that can be easily solved. Initially, the secondaries start at the wall of the vacuum chamber, at $y = -A/2$, where A is the vertical aperture, and have some distribution of velocities $\mathbf{v} = (v_y, v_\perp)$. During one RF period the electrons travel $\Delta y = v_y \tau_{RF}$ before receiving a kick from the next proton bunch. Assuming a transverse waterbag and longitudinal Gaussian beam profile and neglecting the space-charge of the electron cloud the equation of motion during the proton kick becomes

$$\begin{cases} y'' + C \cdot y \exp(-t^2 c^2 / 2\sigma_s^2) = 0, y < r_0 \\ y'' + C \cdot \frac{r_0^2}{y} \exp(-t^2 c^2 / 2\sigma_s^2) = 0, y \geq r_0 \end{cases} \qquad (4.4)$$

$$C = \frac{q_e^2 N_b}{m_e r_0^2 \sqrt{2\pi\sigma_s^2}},$$

where r_0 and σ_s are the transverse and longitudinal bunch sizes and N_b – bunch population. This system has to be solved with a restricting condition $|y| < A/2$ – the electron should stay inside the vacuum chamber.

For some initial values of v_y an electron loses the vertical velocity completely after the kick by the proton bunch. For Fermilab Recycler (Table 4.1) we find five such trapping 'modes' (Fig. 4.3).

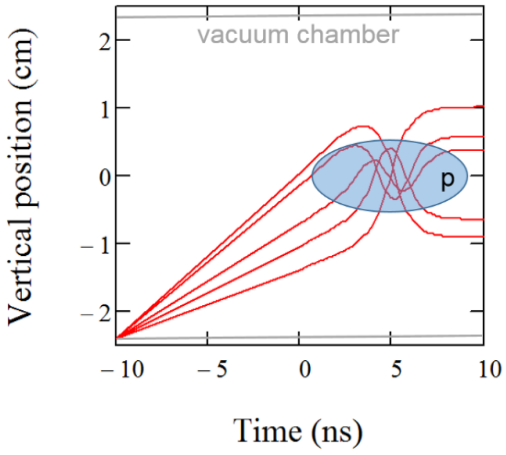

Figure 4.3: There are five distinct trapping 'modes' in Recycler combined function dipoles. Electrons (red trajectories) start at the wall of the vacuum chamber, drift, and then are stopped by the proton bunch (blue). Electron energy E = 5 eV. Timescale – one RF period.

Assuming an initial velocity distribution $f(\mathbf{v})$ from [19] one can estimate the fraction of the electron cloud that falls within the trapping modes (Fig. 4.3) and stays trapped by the field after the beam is gone. For Recycler magnets this ratio can be as high as a few percent for low beam intensities. At the current operational intensity of 5×10^{10} ppb about 1% of particles are trapped, and at higher intensities this amount gets smaller (Fig. 4.4).

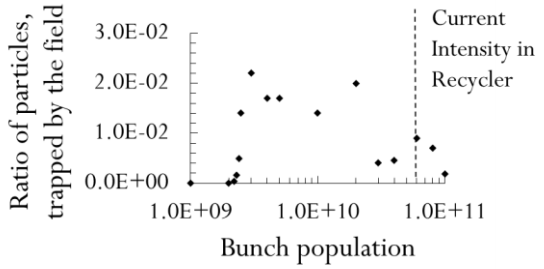

Figure 4.4: About 1% of electrons are trapped at the current beam intensity in Recycler. This fraction reduces for higher intensities.

4.1.2 Electron cloud clearing with a witness bunch

As mentioned above, the trapping requires at least two bunches: the first to kick the cloud and create the secondaries; and the second to stop a fraction of those. Therefore, a single bunch of high enough intensity does not trap the cloud but clears the aperture instead. This clearing bunch can be used to indicate the presence of the trapped electron cloud and measure its density [49] or to bring the electron cloud density below the threshold, stabilizing the beam. The experimental results on the clearing bunch test in Recycler are presented in Sect. 2.3 and the corresponding numerical simulations – in Sect. 4.3.

4.1.3 Lifetime of the trapped cloud

In the absence of the beam, the long-term confinement of the electron cloud can be affected by two effects: longitudinal drift and scattering. The drift is caused by the presence of the magnetic field gradient $B' = dB/dx$ in the transverse plane and its absence in the longitudinal direction. In a pure quadrupole field configuration, the drift might lead to a cloud lifetime of as low as several revolution periods [50], and thus reduce the cloud density the beam sees on the next revolution. An exponential decay with a time constant ~ 60 to 90 μs has been measured in a quadrupole at the PSR ring in

LANL [51]. The effect is significantly weaker for a combined function magnet. The longitudinal drift velocity in this case is

$$v_d = \frac{1}{2}\omega_c r_c^2 \frac{B'}{B_0}, \tag{4.5}$$

where $\omega_c = eB_0/(m_e c)$ is the cyclotron frequency, B_0 – the dipole magnetic field component, and r_c – the radius of the cyclotron orbit. If the cloud drifts a distance l_d comparable with the magnet length L_{dip} it may escape the magnet and decay. For the Fermilab Recycler $v_d < 2\times10^5$ cm/s, L_{dip} = 5 m and the resulting lifetime is ~ 1 ms.

In general, the lifetime of trapped electrons may be also limited by scattering on each other and on the residual gas. For the scattering on the other electron cloud particles the Coulomb cross-section σ_C can be estimated as (see Eq. (41.7) in [24])

$$\sigma_C = 16\pi r_e^2 \left(\frac{m_e c^2}{\varepsilon}\right)^2 \Lambda_C, \qquad \Lambda_C = \ln(1/\chi_{\min}) \tag{4.6}$$

where r_e – is the classical electron radius, ε – the electron energy, c – the speed of light, Λ_C – the Coulomb logarithm, and χ_{min} – the minimal scattering angle. χ_{min} can be estimated as $\chi_{\min} \sim \theta_{\max}$, since the scattering does not lead to a particle loss if it stays within the trapping cone $\theta < \theta_{\max}$. Then for the electron energies $\varepsilon \sim 1-10$ eV the cross-section $\sigma_C < 10^{-13}$ cm^2.

According to the experimental measurements [52], the scattering cross-section for many residual gases is of the order of 10^{-15} cm^2 at the energies $\varepsilon < 10$ eV. Combining the two scattering effects we obtain a lifetime ~ 1 ms for the electron cloud density n_e < 10^7 cm^{-3} and the residual gas pressure P ~ 10^{-8} Torr.

Since all the loss mechanisms result in the lifetime significantly greater than the revolution period of 11 μs, all the trapped cloud will be present on the next turn. It will act as the new seed electrons, and can lead to a higher electron cloud density on the next revolution.

4.2 Numerical model

In order to see how the presence of trapping changes the build-up of the electron cloud and leads to a two-stream instability, we used an electron cloud simulation code PEI4, running on the Fermilab's Wilson computing cluster. PEI4 is fast and flexible Fortran-based code, initially developed at KEK for simulation of electron cloud driven instabilities in positron rings [53]. It is capable of solving a combined problem of electron cloud build-up and its interaction with the beam in 2D (only the transverse motion). The flexibility of the code allows incorporation of an arbitrary magnetic field, proton or positron beams, and various bunch train distributions.

4.2.1 Model of the beam

The beam is represented by a series of rigid bunches with Gaussian shape. Their transverse and longitudinal sizes are defined by three sets of corresponding emittances and beta-functions. The bunches are separated by longitudinally by 1 RF period and form bunch trains. The number of trains, number of bunches in a train, and the intensity of each individual bunch can be adjusted. Because the bunches are considered to be rigid, there is no Landau damping in the simulation.

4.2.2 Model of the ring

The ring was modelled as a linear transfer matrix with one thin interaction point, representing the electron cloud inside of a magnet. With the help of its author K. Ohmi (KEK) the PEI code was changed to accommodate a combined function magnet, as well as a pure dipole or a quadrupole. The replacement of a set of extended magnets by one lumped element is justified from the beam dynamics

point of view. It gives the same result in the first, linear, order of perturbation theory [37], but is significantly less demanding computationally.

4.2.3 Model of the electron cloud

The electron cloud is represented by an ensemble of macroparticles of a constant weight. Each macroparticle is described by its transverse displacement relative to the center of the beampipe and transverse velocity. When a particle reaches a wall of the vacuum chamber, the secondary electrons are produced. The macropartilces are then rearranged to keep the number of electrons in each of them constant.

The main source of primary electrons in Recycler is ionization of residual gas by the beam. To simulate it the seed electrons were put at the beam with their linear density following $\lambda[\mathrm{m}^{-1}] \sim 6N_b \times P[\mathrm{Torr}]$, where P is the gas pressure and N_b is the number of particles per bunch [14].

The model of secondary emission includes true secondary and elastically reflected electrons and assumes normal incidence (for more details refer to Sect. 1.1.2). In a dipole field, however, an electron hits the wall of a vacuum chamber at an angle. That increases the time the electron spends near the wall surface and consequently the SEY. Experimental data on angular dependence of SEY fits an empirical formula:

$$SEY = SEY_0(1 + a_1(1 - \cos(\theta)^{a_2})), \tag{4.7}$$

where a_1 and a_2 are material specific parameters and SEY_0 – the yield measured at normal incidence [17]. For a simple estimate one can use $a_1 = 0.26, a_2 = 2$. Then for the Fermilab Recycler combined function dipoles the simulated mean incident angle is 15 deg (Fig. 4.5) and the resulting increase of SEY, according to Eq. (4.7) is about 5%.

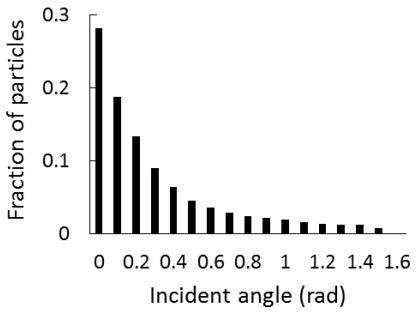

Figure 4.5: Most particles hit the vacuum chamber at small angles to the normal.

4.2.4 Beam-cloud interaction

The beam-cloud interaction is calculated using the classical Basetti-Erskine model [54]. The models uses the complex error functions for a fast evaluation of the electric field of a two-dimensional Gaussian charge distribution. To calculate the impact of the three-dimensional Gaussian beam on the cloud the program splits the bunch into a number or longitudinal slices and then calculates the kick of each slice.

The PEI code supports three main modes of operation. In the first regime it calculates only the build-up of the electron cloud, created by a train of stationary proton or positron bunches. The kick of the cloud on the beam is not calculated. This mode is suitable for a fast computation of the cloud density for a particular beam intensity. In the second regime the code computes the impact of the electron cloud on every bunch, but still treats the bunches as stationary. This allows a fast computation of the unstable modes in the beam and their growth rates. And finally, the last mode is tracking, coupled with the electron cloud build-up.

4.3 Electron cloud build-up

The accumulation of the electron cloud depends on a vast variety of parameters, including the properties of the beam, the vacuum chamber, and the magnetic fields. In this section we, first briefly examine these dependencies, then show how the mechanism of trapping changes the build-up, and finally find the density of electron cloud for current and planned future intensities in Recycler.

4.3.1 Dependence on the secondary emission

One of the major unknown parameters of the problem is the secondary emission yield (SEY) of the beampipe. Because the build-up of electron cloud is an exponential process even a small change in SEY can change the picture of the build-up (Fig. 4.6). For a batch of 60-cm-long bunches of 5×10^{10} p for smaller SEY's, below 2.2, the electron cloud does not accumulate during the passage of the beam. For SEY ~ 2.5 the cloud builds-up to a certain linear density and then decays after the beam is gone, but the final density remains higher than the ionization density, allowing multi-turn accumulation of the cloud. For high SEY's, greater than 2.8, the cloud reaches saturation at about the beam density (more detail in Sect. 4.3.3). The saturation is likely to occur because the self space charge force of the cloud starts to compensate the Coulomb force of the beam.

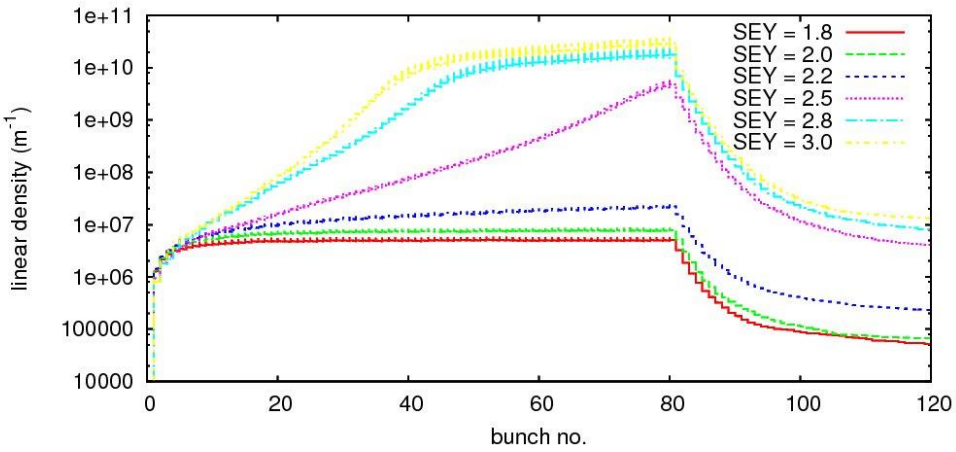

Figure 4.6: A small change in SEY leads to a drastic increase of electron cloud density after the passage of one bunch train. $N_b = 5\times10^{10}, \sigma_z = 60\text{cm}$. At high SEY's the cloud reaches saturation at about the linear density comparable to the density of the beam ($\sim 9\times10^9\ \text{m}^{-1}$).

For normal Recycler 60-cm-long bunches the secondary emission yield of at about 2.5 or higher is required for the electron cloud to accumulate at the current intensities. Such a high SEY typically is not achieved in stainless steel. Shorter bunches have a higher peak charge density and therefore may create the cloud at lower SEY. The dependence of the cloud build-up on the bunch length is discussed in the next section.

4.3.2 Dependence on bunch length

The bunch length is an important parameter of the problem. In an experiment the beam becomes unstable when its bunch length shrinks (Fig. 2.6) due to quadrupole oscillations of the bunch length. Their magnitude of these oscillations (based on the observations of the normal Recycler operation) can be as high as 30%. This is enough to significantly change the picture of the electron cloud build-up.

Figure 4.7 depicts accumulation of the cloud during one passage of a batch of 80 $5\times10^{10}\,p$ for different bunch lengths and SEY = 2.1 For the nominal bunch length of 60 cm and longer bunches the maximum electron cloud density is small – of the order of 10^7 m^{-1}. For a shorter 40-cm-long bunch the cloud reaches the density between 10^8 and 10^9 m^{-1}. About 10^{-2} of those particles stay tapped after the beam has passed, allowing the cloud to accumulate over multiple revolutions. For even shorter bunches, the cloud might reach a saturation density of about 10^{10} m^{-1} in a single pass. The small density of the cloud at $\sigma_z = 60\text{cm}$ and significantly higher density for shorter bunches qualitatively explain why the instability is only seen when the bunches compress longitudinally.

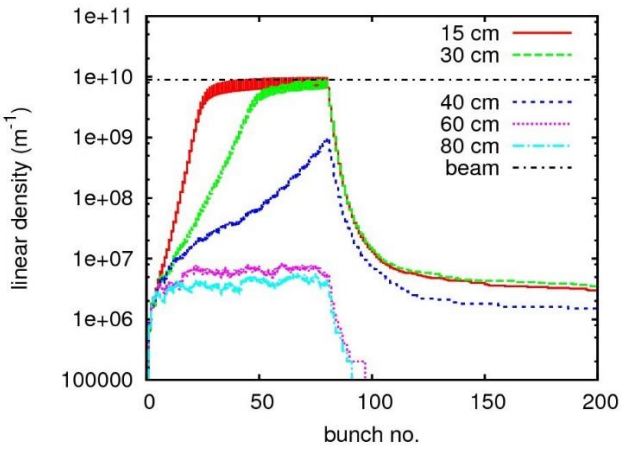

Figure 4.7: The build-up of electron cloud is much faster for shorter bunches. SEY = 2.1; single pass, $N_b = 5\times10^{10}$, 80 bunches; ionization density 10^6 m^{-1}.

4.3.3 Saturation of the electron cloud

It is often seen in the simulation that the density the electron cloud increases exponentially and the stops at a certain threshold. This levelling off is called 'saturation'. It happens when the flux of the particles hitting the wall of the vacuum chamber equalizes the flux of the new born secondaries. There are two possible explanations for this effect. First, as the density of the cloud increases its own space

charge starts playing a role in the dynamics of the build-up. The negative charge of a dense cloud can screen the positive charge of the proton beam, reducing its kick and hence the energy of the electrons hitting the wall of the vacuum chamber. Because of the dependence of the secondary yield on the incident energy the lower energetic electrons are likely to produce less secondaries, so the secondary flux decreases. If the hypothesis is correct, the electron cloud should saturate at about the average beam intensity, which is what we saw in Fig. 4.7.

The second explanation is that as the electron density increases, the diffusion losses during the periods of no beam go up and, at a certain point, start compensating the production during the arrival of the next bunch. The amount of particles the cloud loses due to diffusion depends on the distance between the bunches, so if this is the mechanism of the saturation, the saturation density should depend on the bunch length (shorter bunches mean more no-beam time for the same RF period).

To find out the true nature of the saturation we ran the build-up simulations for the same beam intensity and a number of bunch lengths. The results show that the cloud saturates at about the beam intensity both for short and for long bunches with no dependence on the bunch length, or alternatively on the drift time (Fig. 4.8). For shorter bunches the cloud just reaches the saturation slightly earlier, which is expectable since the shorter bunches have more peak intensity and supply more energy to the cloud on impact, leading to a higher secondary yield. When the space charge of the cloud was turned off, the cloud no longer saturated, proving that the saturation is caused the self space charge of the electron cloud.

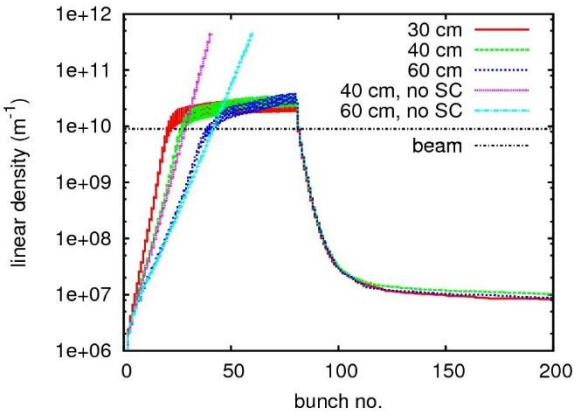

Figure 4.8: The electron cloud saturates at a linear density comparable with the density of the beam, independent its bunch length. Without the self space charge the cloud intensity continues to grow exponentially with no saturation (no SC lines). The lines show different bunch lengths for the same intensity $N_b = 5\times10^{10}$ and SEY = 3.0.

4.3.4 Trapping in a combined function magnet

To determine the effect of particle trapping on the density of the electron cloud we performed simulations of the cloud build-up over multiple revolutions in the machine and compared the outcome with the analytical estimates, presented in Sect. 4.1.

For a pure dipole field, the cloud rapidly builds up during the passage of the bunch train and then decays back to the initial ionization electron density in about 300 RF buckets, or ~ 6 μs (Fig. 4.9). When the field gradient is added, up to 1% of the electron cloud stays trapped, increasing the initial density on the next revolution. The final density, which the cloud reaches after ~ 10 revolutions, is two orders of magnitude greater than in the pure dipole case (Fig. 4.9). The resulting cloud distribution is a stripe along the magnetic field lines, with a higher particle density being closer to the walls of the vacuum chamber (Fig. 4.10). The electron cloud stripe should produce a horizontal focusing effect, because of its horizontal location at the beam center. In the vertical plane, the simulated cloud distribution should defocus the beam due to the higher charge density outside of the beam. This agrees

qualitatively with the observed betatron frequency shifts (Fig. 2.13). A more rigorous, qualitative comparison is given in Sect. 5.2.

At lower densities ~10^{-2} of particles are trapped, which agrees with an estimate from Eq. (4.3); as the density of electron cloud increases the trapping ratio goes down to ~10^{-3}. The most likely cause of this decrease is the space charge of electron cloud which was neglected in the analytical estimates.

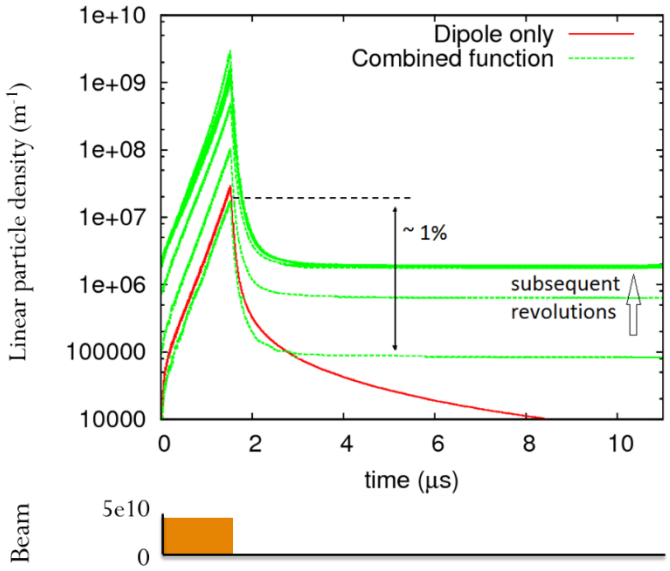

Figure 4.9: In a combined function magnet the electron cloud accumulates over many revolutions, reaching a final density much higher than in a dipole. Beam: 5*10^{10} ppb, 80 bunches.

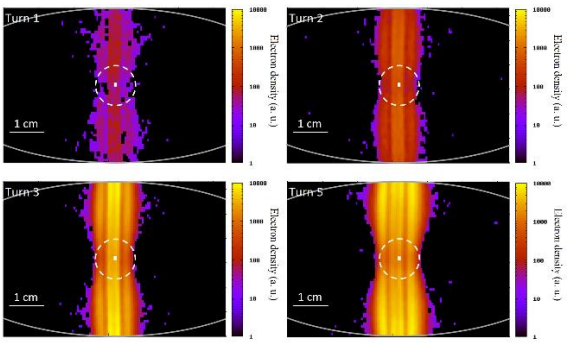

Figure 4.10: Electron cloud forms a stripe inside the vacuum chamber and its intensity increases with the number of turns. Its horizontal position – beam center (white dot). White circles represent 2 rms beam size.

The multi-turn electron cloud accumulation due to the trapping mechanism might play an important role in a proton ring, where the density of the primary ionization electrons is relatively low. For a positron machine of a similar energy the amount of primary electrons is much greater due to the photoemission by synchrotron radiation. Because of the large number of primary electrons, the cloud can reach a saturation density during just one passage of a bunch train. Then the presence of trapping would only slightly affect the overall picture, shifting the saturation towards the head of the batch. The recent numerical study at CESR using an ECLOUD code shows that, due to the high average photon absorption rate of 2.15 $\gamma/m/e^+$ the cloud in its combined function magnets reaches a saturation density during the passage of one positron bunch train [15]. We obtain similar results simulating the positron beam in the DAFNE ring [55] (Fig. 4.11).

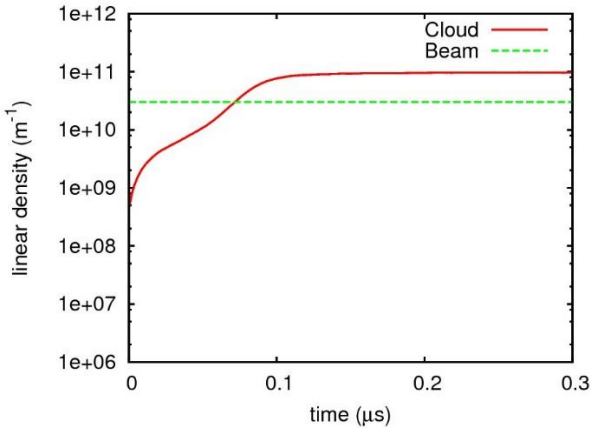

Figure 4.11: The electron cloud reaches the saturation density within one revolution period in the DAFNE ring. The ring circumference of 0.3 μs is uniformly filled with 120 e^+ bunches, $N_b = 2.4\times10^{10}$. The key ring parameters are summarized in Table 4.2.

4.3.5 Clearing with a witness bunch

As mentioned in Sect. 4.1.3, a trapped cloud can be cleared by a single bunch following the beam at a sufficient distance. In Fig. 4.12 a bunch of $5*10^{10}$ protons, added 120 RF buckets after the main batch, destroys the trapped cloud, preventing the multi-turn build-up. First, one can see a small increase in the cloud density as the clearing bunch kick the cloud and it reaches the vacuum chamber, producing the secondary electrons. Then, the density rapidly drops as these secondaries reach the aperture.

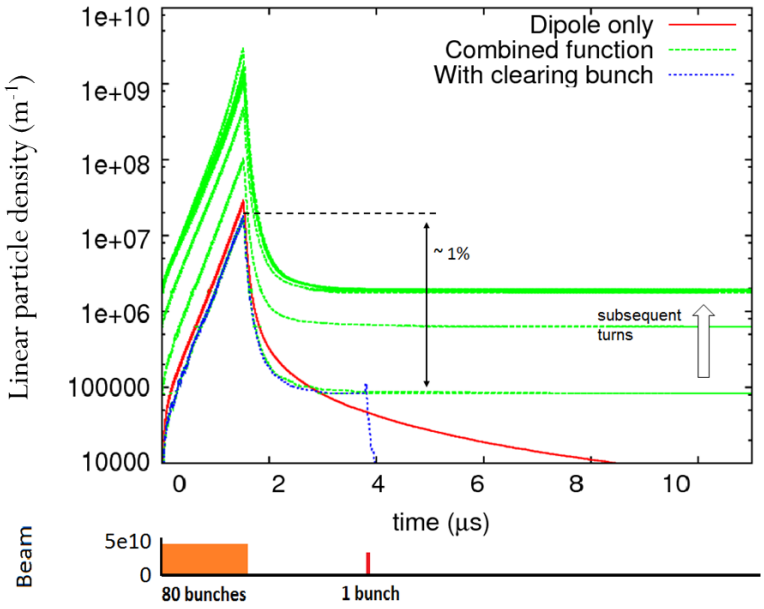

Figure 4.12: A clearing bunch destroys the trapped cloud, preventing the multi-turn accumulation in a combined function magnet. The resulting maximum electron cloud density is the same as in a pure dipole. Beam: $5*10^{10}$ ppb, 80+1 bunches

The clearing effect observed in this simulation explains the stabilization of a high-intensity beam by a low intensity pilot bunch, described in Sect. 2.3. The clearing bunch prevents the multi-turn accumulation of the electron cloud, significantly reducing its final density. In the above simulation the density was reduced by two orders of magnitude to the level seen in a pure dipole.

Table 4.1: Recycler parameters for simulation in PEI

Beam energy	8 GeV
Machine circumference	3.3 km
Batch structure	80 bunches, 5e10 p
Tunes: x, y, z	25.45, 24.40, 0.003
RF harmonic number	588
RMS bunch size: x, y, z	0.3, 0.3, 40 cm
Secondary emission yield	2.1 @ 250 eV
Density of ionization e^-	10^4 m^{-1} (at 10^{-8} Torr)
B-field and its gradient	1.38 kG, 3.4 kG/m
Beampipe	Elliptical, 100 x 44 mm

Table 4.2: DAΦNE e+ parameters for simulation in PEI

e^+ energy	0.51 GeV
Machine circumference	97.7 m
Batch structure	120 bunches, 2.44×10^{10} e^+
Tunes: x, y, z	5.15, 5.21, 0.012
RF harmonic number	120
RMS bunch size: x, y, z	0.3, 0.01, 2.5 cm
Secondary emission yield	2.1 @ 250 eV
Density of photo e^-	3.3×10^8 m^{-1}
B-field	Dipole, 10 kG
Beampipe	Rectangular, 64 x 20 mm

4.3.6 Peak density of the electron cloud

Thanks to the trapping mechanism, the electron cloud, accumulating over many revolutions, might reach a significantly higher density than after the first passage of the beam. The amount of the accumulated cloud depends on the beam intensity and on the efficiency of trapping, which, in turn, also depends on the beam intensity (Fig. 4.4). Figure 4.13 shows the final steady state distributions of the electron cloud density during a passage of 1 batch in Recycler. The maximum linear density is achieved not at the highest intensities, but instead for $N_p \sim 6-7\times10^{10}$ ppb (Fig. 4.14). An interesting case in the line at $7.5*10^{10}$ ppb: while the build-up rate is high due to high bunch charge, the trapping ratio is low, resulting in the peak density lower than for smaller intensities $5-7\times10^{10}$ ppb.

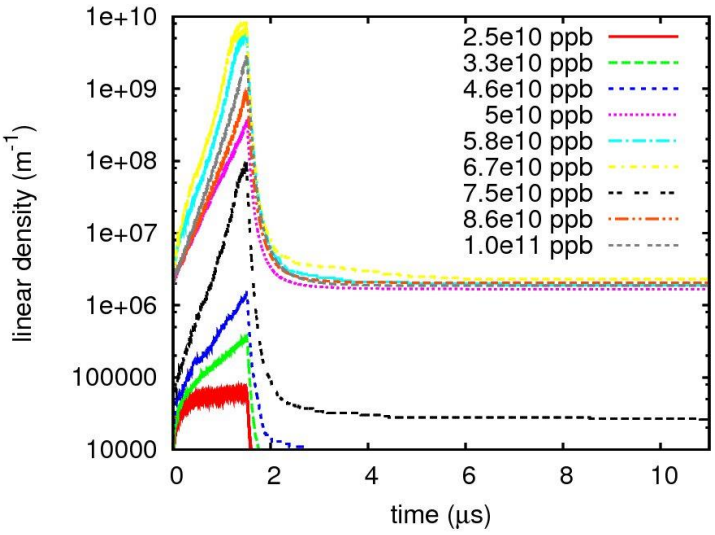

Figure 4.13: The final distribution of the electron cloud density after 20 revolutions of multi-turn build-up. 1 batch of different intensities. SEY = 2.1, σ_z = 40 cm, ionization density 10^4 m^{-1}.

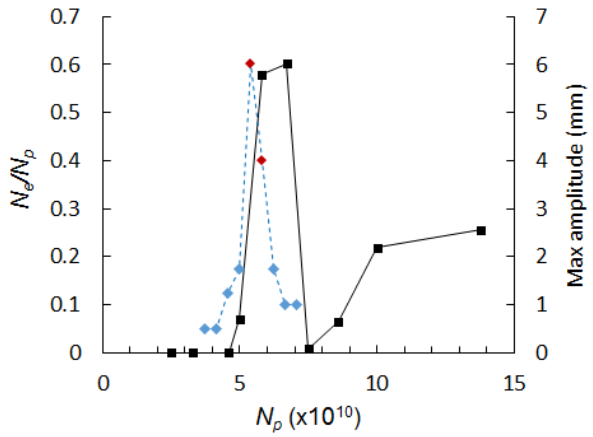

Figure 4.14: Electron cloud density reaches its maximum density at the intensities of $N_p \sim 6-7\times10^{10}$ ppb. The vertical axis shows the normalized electron cloud density N_e/N_p. The dashed line shows the maximum betatron amplitude measured for these intensities.

The maximum of the cloud density in Fig. 4.15 coincides with the intensities where the most rapid instability is observed (for more details on the intensity scan, refer to Sect. 2.2.2). That is one more evidence that the observed instability is caused by the electron cloud. The discrepancy in the width of the two peaks in Fig. 4.14 can be caused by several effects. The first one is the change of bunch length in the experiment – the Recycler was optimized to work at the intensity of 14 turns (about $6*10^{10}$ ppb); and operation at higher intensities lead to a deterioration of the quality of the Booster beam and increase of longitudinal emittance in Recycler. The second effect is the absence of Landau damping in the simulation – as the electron cloud density increases it should start creating a spread of the incoherent frequencies leading to Landau damping of betatron coherent oscillations. This is effect is not accounted for in our rigid bunch model.

4.3.7 Electron cloud in drift sections

The picture would have been incomplete without the consideration of electron cloud in the straight sections. The drifts, that occupy almost 40% of the machine circumference, might also accumulate the electron cloud. Due to the absence of the strong magnetic fields the trapping and consequently the multi-turn accumulation of the cloud, described in the previous sections, in impossible in a drift. Therefore one only need to study the evolution of the cloud density during a single pass of the beam through the straight section.

In a drift the electron cloud fills the aperture almost uniformly with a slightly higher density near the wall of the vacuum chamber directly above and below the beam (Fig. 4.15). Unlike in the dipole case, in a straight section most of the cloud is located outside of the beam, and therefore has a low impact on its dynamics. In the extreme case of a uniform charge density only the charges inside the beam affect its motion.

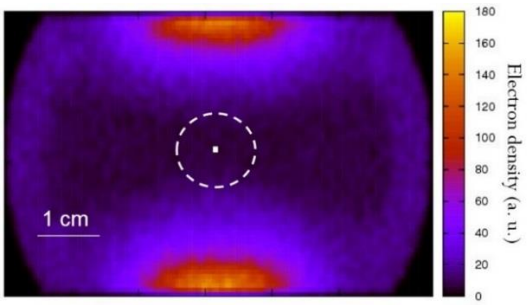

Figure 4.15: The electron cloud fills the aperture almost uniformly in a drift section. The snapshot was taken at the moment the last bunch of the train left the section. The beam center and its 2 rms size are shown in white. 1 batch of 80 bunches, $5*10^{10}$ ppb, SEY = 2.1, σ_z = 40 cm.

For the cloud to start to exponentially build-up during the passage of the beam, its intensity has to above the threshold of about 4×10^{10} for SEY = 2.1 (Fig. 4.16). The build-up becomes more rapid at higher intensities. After the beam has passed, the electron cloud density falls down rapidly as the particles drift, eventually reaching the physical aperture (Fig. 4.16).

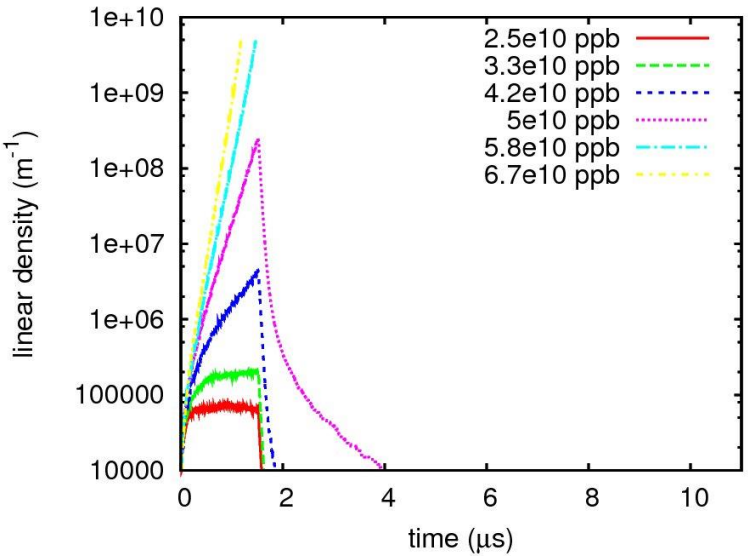

Figure 4.16: The cloud in a drift section accumulates rapidly during the passage of a bunch train for beam intensities greater 4×10^{10} ppb, it then decays quickly after the beam has left the section. SEY = 2.1, σ_z = 40 cm. At the highest intensities the computation was interrupted after exhausting all available memory.

At the current beam intensities the dominant source of the electron cloud in Recycler is its combined function magnets (Fig. 4.17). They create a cloud of a greater number of electrons, which are located mostly at the beam center, compared to the free space that creates a lower number, almost uniformly cloud distributed throughout the vacuum chamber. At the higher proton intensity of 1×10^{11} ppb, required for the PIP-II upgrade, the two effects are of the dame order though. The high density of the cloud in the straight sections may pose a challenge at the PIP-II intensity. Electron cloud effects in the drifts have to be carefully studies.

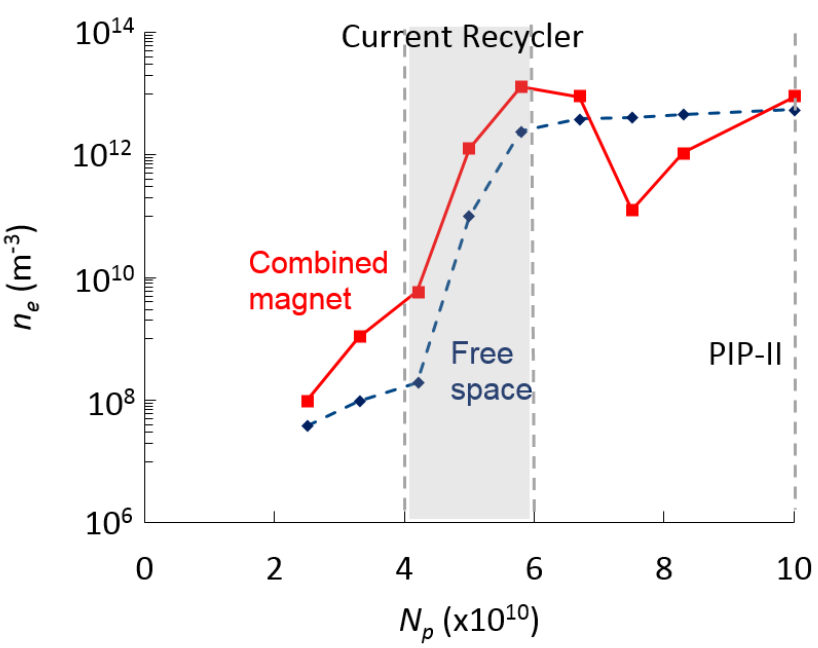

Figure 4.17: Combined function magnets provide one to two orders of magnitude greater electron cloud density at the beam center n_e than the free space at the current Recycler intensities. For the higher PIP-II intensities the tow effects are comparable. SEY = 2.1, σ_z = 40 cm, $P = 10^{-8}$ Torr.

4.4 Electron cloud instability

Using of the electron cloud, estimated in the previous section, we can now proceed to the study of the resulting instability. The PEI code allows the tracking of the proton beam with a simultaneous simulation of the cloud build-up. Because of the huge computational complexity of the problem, the numerical model (described in Sect. 4.2) is rather simplified. The proton beam is treated in the rigid bunch approximation, therefore only the multibunch modes appear in the simulation. The high-frequency head-tail intra-bunch modes cannot be resolved in this model. Another consequence of the rigid bunch model is the absence of the stabilizing Landau damping. Finally, the long range resistive wall interaction, that could provide an additional coupling between the tail of the bunch train and its head, is out of the scope of this study.

4.4.1 Growth rate

The simulation starts with a batch of 80 proton bunches of 5×10^{10} ppb at the reference orbit (no injection mismatch). At the interaction point each bunch creates primary ionization electrons and kicks the cloud producing the secondary electrons. The action of the electron cloud on the bunch is also calculated at each time step. The key simulation parameters are summarized in Tables 4.1, 4.3.

The initial beam oscillations in the simulation appear due to numerical noise and the random kicks from the low number of macroparticles, representing the electron cloud in the beginning of its build-up. After the electron cloud reaches its steady state density due to the trapping and the resulting multi-turn build-up, the horizontal oscillations of the bunch train start to grow rapidly (Fig. 4.18). The bunches in the tail of the batch are the most unstable, since they receive the accumulated kick from all the previous bunches. The head of the batch remains relatively stable, as it interacts only with the trapped particles, whose density is relatively low. As the oscillation amplitude increases, the bunches in the head and in the tail start building up the cloud at different horizontal positions. Consequently the build-up becomes less efficient, and the electron cloud density decreases. The simulation also show relatively high-frequency betatron oscillations in the vertical plane, although no visible increase is seen during the first 20 revolutions.

The amplitude modulation seen in Fig. 4.18 is caused by the betatron motion. In the absence of the instability a particle rotates on its phase-space ellipse with its betatron frequency (Fig. 4.19). Since the particle's position, plotted in Fig. 4.18, is a mere projection of the phase-space ellipse of the horizontal axis *x*, the betatron motion leads to a sin-like modulation of the observable. The period of the modulation is defined by the fractional horizontal tune, and equals to 10 turns for the Recycler horizontal tune of 0.45. One can remove the effect by going to the normalized coordinates:

$$\begin{aligned} x_N &= x/\sqrt{\beta_x} \\ p_{x,N} &= \alpha_x x/\sqrt{\beta_x} + x'\sqrt{\beta_x} \end{aligned} \tag{4.8}$$

and similarly for the vertical plane. a and β are the Twiss parameters (see for example [15]). In the normalized coordinates the phase space trajectory is a circle. The rate of the increase of its radius $R = \sqrt{x_N^{\,2} + p_{x,N}^{\,2}}$ will give us the growth rate of the instability.

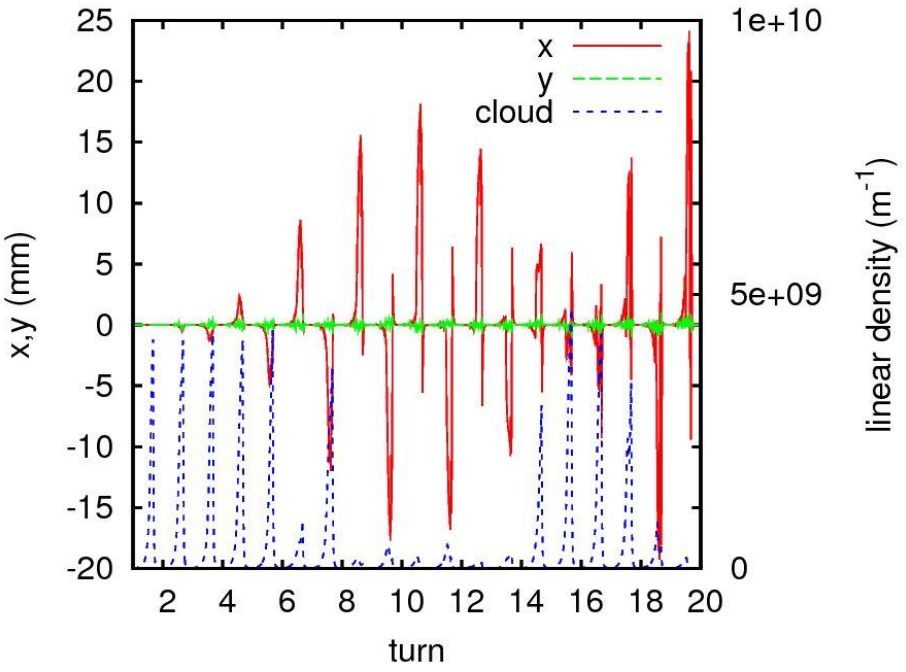

Figure 4.18: As the electron cloud reaches its maximum density the horizontal instability starts developing. The horizontal and vertical positions of every bunch in the batch and the electron cloud density are plotted for the first 20 revolutions after the cloud has accumulated to its maximum density (about 5×10^{9} m^{-1}). On the 21st revolution the simulation was stopped due to a loss of some of the particles.

Table 4.3: Twiss parameters at the interaction point

Axis	α	β, m	γ, m^{-1}	ε, mm-mrad
x	0	40	0.025	0.22
y	0	40	0.025	0.2
s	0	1000	0.001	200

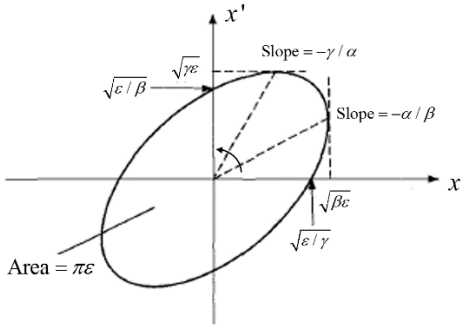

Figure 4.19: The phase space trajectory in the physical coordinates x and x' is an ellipse. α, β, and γ are the Twiss parameters, ε is the Courant-Snyder invariant $\varepsilon = \gamma x^2 + 2\alpha x x' + \beta x'^2 = const$ [56].

Figure 4.20 plots the logarithm of the radius of the phase-space trajectory R as a function of the revolution number. Applying linear fits to the data we can estimate the instability growth rates in both planes. We obtain the horizontal growth rate of 11 turns; no instability is observed in the vertical plane. The resulting high growth rate of the instability is likely to be an overestimate, because our macroparticle numerical model with a linear accelerator lattice could not include the stabilizing effects of Landau damping and nonlinear decoherence.

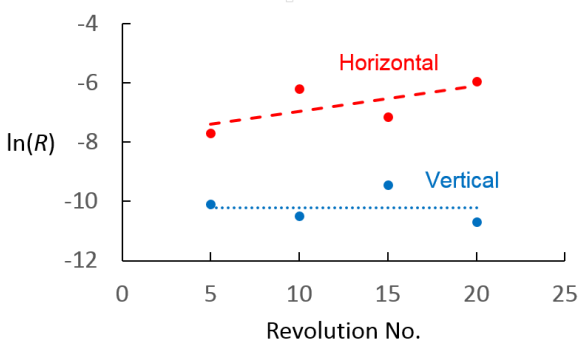

Figure 4.20: The instability develops only in the horizontal plane. The dashed lines represent linear fits. The horizontal growth rate is 8.6×10^{-2} rev.$^{-1}$, the vertical growth rate is 0.

4.4.2 Most unstable mode

As the beam becomes unstable, the transverse mode with the highest growth rate rapidly suppresses the others. The frequency of this most unstable mode can be derived from the tracking results by a simple Fourier transform. In order to reduce the numerical noise, one has to prepare the data before the processing. First, the average offset, was accounted for to remove the constant component. Then a Hamming window was applied to the data to enforce its periodicity and reduce the noise in the resulting spectrum. Finally, a Discrete Fourier Transform (DFT) was performed to the horizontal positions of the bunches in the batch on each revolution. The resulting spectrum has a sharp peak at the low frequencies (Fig. 4.21).

The spectral density in Fig. 4.21 has a maximum at low frequencies, with the peak being at 0.66 MHz. The density rapidly falls down at the higher frequencies. The upper frequency bound, 26.5 MHz is set by our rigid bunch model and the RF frequency of f_{RF} = 53 MHz. The frequency resolution of the method is $\Delta f = f_{RF}/80$ = 0.66 MHz is limited by the number of bunches in the batch.

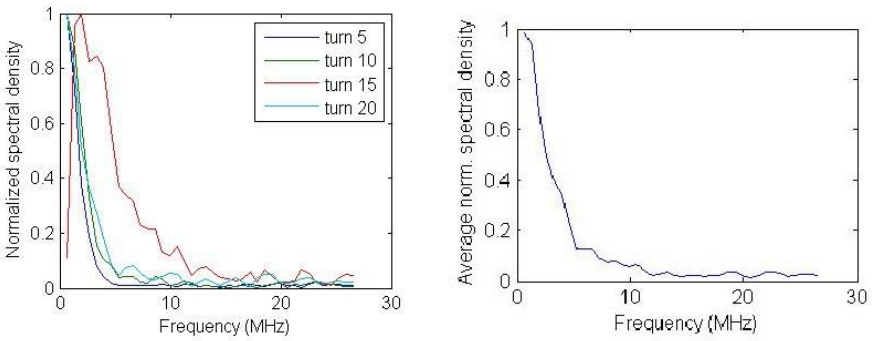

Figure 4.21: The frequency of the most unstable mode is 0.66 MHz. Left – the evolution of the spectrum over the time scope of the instability – 20 turns. Right – the normalized spectral density, averaged over the last 10 revolutions.

To sum it up, the analysis shows that the trapping in combined function magnets allows the multi-turn accumulation of the electron cloud. The resulting cloud density can be up to two orders of magnitude greater than that in a pure dipole. After the electron cloud has reached its maximum density, it starts driving a multibunch instability in the horizontal plane with a growth rate of 11 revolutions. The most unstable mode is the low frequency mode with a frequency below 1 MHz. It can therefore be efficiently suppressed with a strong enough transverse feedback system, acting on the center of mass of each bunch.

CHAPTER 5

ANALYTICAL MODEL OF THE ELECTRON CLOUD INSTABILITY

An analytical model is potent to give an important insight into the dynamics of the instability. In this chapter we, first, present a model of the transverse multibunch instability, driven by the electron cloud trapped in the combined function magnets. Then, we apply the model to explain the instability currently seen in Recycler and compare the analytic estimates with experiment and simulation. And finally, we consider the impact of increasing the beam intensity to the limit set by the PIP-II.

5.1 Model of the beam-cloud interaction

According to numerical studies with the PEI code (presented in Chapter 4), the trapping mechanism allows the electron cloud to gradually build up over multiple turns, reaching a final density orders of magnitude greater than in a pure dipole. The resulting cloud distribution is a stripe along the magnetic field lines, with higher particle density closer to the walls of the vacuum chamber (Fig. 5.1). The width of the stripe is about the size of the beam. Knowledge of the electron cloud build-up and its distribution allows the construction of a simple model of the electron cloud instability in Recycler.

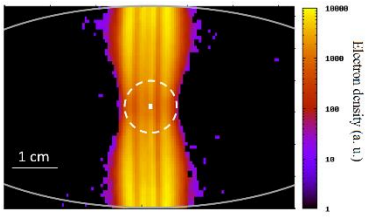

Figure 5.1: Electron cloud forms a stripe inside the vacuum chamber; the beam center and its 2 rms size are shown in white (for more details refer to the Sect. 4.3.4).

5.1.1 Coasting Beam

First, consider a round coasting proton beam travelling in a ring, uniformly filled with electron cloud. Let us denote the position of the beam centroid at an azimuthal angle θ at time t as $X_p(t, \theta)$. Further, assume that the beam travels at a constant azimuthal velocity around the ring ω_0 and use a smooth focusing approximation with betatron frequency ω_β.

For simplicity, we represent the electron cloud by a vertical stripe of uniform charge density, located at a horizontal position X_e. Let us further assume that the number of electrons remains, on average, constant in time. Because of the vertical dipole field, the individual electrons of the cloud cannot drift horizontally, but the position of the cloud can change as some regions build up and others are depleted, following the transverse motion of the proton beam. The characteristic time constant of this slow motion is then the time of build-up: $\lambda \sim 1/\tau_{buildup}$.

For small oscillation amplitudes we can assume the electron-proton interaction force to be linear in displacement. Then the coupled collective motion of the beam and the electron cloud is described by the following system of equations:

$$\begin{cases} \left(\frac{\partial}{\partial t} + \omega_0 \frac{\partial}{\partial \theta}\right)^2 X_p + \Gamma\left(\frac{\partial}{\partial t} + \omega_0 \frac{\partial}{\partial \theta}\right) X_p = -\omega_\beta^2 X_p + \omega_p^2 X_e \\ \frac{\partial}{\partial t} X_e = \lambda (X_p - X_e) \end{cases}, \tag{5.1}$$

where Γ is the rate of Landau damping. The coupling frequency ω_p is

$$\omega_p^2 = \frac{\langle N_e \rangle_{circ} r_e c^2}{\pi \sigma^2 R} \cdot \frac{m_e}{\gamma m_p} = \frac{e^2 n_e}{2\varepsilon_0 \gamma m_p}, \tag{5.2}$$

where r_e is the classical radius of electron, σ – RMS transverse size of the beam, R – radius of the ring, n_e – electron cloud density, and γ – relativistic factor.

The linear damping term Γ in Eq. (1) arises from the spread in betatron frequencies for particles oscillating with different amplitudes. The characteristic rate of the Landau damping can be estimated as

$$\Gamma \sim \omega_\beta \frac{\Delta Q_x}{Q_x}, \tag{5.3}$$

where Q_x is the horizontal tune and ΔQ_x is its rms spread.

Looking for solutions of Eq. (5.1) in a form $X_{e,p} \propto e^{-i\omega t + in\theta}$ one obtains an equation for the mode frequency ω:

$$-(\omega - n\omega_0)^2 - i\Gamma(\omega - n\omega_0) + \omega_\beta^2 - \omega_p^2 \frac{i\lambda}{\omega + i\lambda} = 0 \tag{5.4}$$

It can be solved perturbatively, under the assumption that

$$\omega_\beta, \lambda \gg \omega_0, \omega_p, \Gamma. \tag{5.5}$$

This assumption is valid only for a relatively high betatron tune $Q_x = \omega_\beta / \omega_0 \gg 1$ and a relatively long ring (needed for $\lambda \gg \omega_0$), which is generally the case for storage rings.

Solving Eq. (5.4) in the leading order one gets two modes for each wave number n: $\omega_\pm - n\omega_0 = \pm\omega_\beta$. Then in first order:

$$\omega_\pm = n\omega_0 \pm \omega_\beta + \Delta\omega, \tag{5.6}$$

where the small complex tune shift $|\Delta\omega| \ll \omega, \lambda, \omega_\beta$ is:

$$\Delta\omega \approx \frac{1}{2}\left[-i\Gamma \pm \frac{\omega_p^2}{\omega_\beta} \frac{\omega_\pm(\omega_\pm - i\lambda)}{\lambda^2 + \omega_\pm^2} \right] \tag{5.7}$$

It may be more convenient to look at the real and imaginary parts of $\Delta\omega$ separately:

$$\begin{aligned} \mathrm{Im}(\Delta\omega) &\approx \frac{1}{2}\left[-\Gamma \mp \frac{\omega_p^2}{\omega_\beta} \frac{\lambda\omega_\pm}{\lambda^2 + \omega_\pm^2} \right], \\ \mathrm{Re}(\Delta\omega) &\approx \pm \frac{\omega_p^2}{2\omega_\beta} \frac{\omega_\pm^2}{\lambda^2 + \omega_\pm^2}. \end{aligned} \tag{5.8}$$

The imaginary tune shift in Eq. (5.8) consists of two parts with the first being the negative Landau damping term. The motion becomes unstable only if the whole expression is positive. The "+" modes are always stable, while the "-" modes can be unstable for some n if $\mathrm{Im}(\Delta\omega) > 0$. The most unstable mode, for which $\mathrm{Im}(\Delta\omega)$ is the greatest, is $\omega_{\max} = \lambda$ and its wave number $n_{\max}$ is

$$n_{\max} = \frac{\omega_\beta + \lambda}{\omega_0} = Q_x + \frac{\lambda}{\omega_0}, \tag{5.9}$$

and the growth rate of this mode is

$$\gamma_{\max} = \frac{1}{2}\left(\frac{\omega_p{}^2}{2\omega_\beta} - \Gamma \right). \tag{5.10}$$

In an experiment an observer sees the most unstable mode as it suppresses the others thanks to its higher exponential growth rate. Thus, a turn-by-turn measurement of beam position at $\theta = \theta_0$ will detect a shift of the betatron tune of

$$\Delta Q_{\max} \approx \frac{1}{4Q_x}\frac{\omega_p{}^2}{\omega_0{}^2}. \tag{5.11}$$

The resulting betatron tune shift is two times lower than the tune shift for a uniform electron cloud density [23].

5.1.2 Bunched Beam

The previous discussion is valid for the case of a coasting beam. In order to calculate the instability growth rate for a bunched beam one needs to first compute the wake-functions or the electron cloud impedance.

First, let us use the complex frequency shift $\Delta\omega$, obtained for a coasting beam, and find the impedance of the cloud as (see for example A. Chao [37] Eq. (6.262)):

$$Z(\omega) = \frac{2\gamma T_0{}^2 \omega_\beta}{N r_0 c} i\Delta\omega, \tag{5.12}$$

where N is the total number of protons in the ring and r_0 is the classical proton radius. We can do this trick because the impedance is the property of the medium only and hence does not depend on the model of the beam.

Eq. (5.12) is valid for wake-fields that do not affect the incoherent frequencies. Because the electron cloud does shift both coherent and incoherent frequencies, and because what matters for an instability is the distance between the coherent and the incoherent tunes, we have to subtract the incoherent tune shift from $\Delta\omega$ before plugging it into the equation. The incoherent tune shift can be found from Eq. (5.8) in the limit of large ω as

$$\Delta\omega \approx -\frac{\omega_p^2}{2\omega_\beta} \tag{5.13}$$

Knowing the impedance one can compute the wake functions using a well-known relation (see for example Eq. (2.72) in [37]):

$$W(z) = \frac{-i}{2\pi}\int_{-\infty}^{+\infty} Z(\omega) e^{i\frac{\omega z}{c}} d\omega \tag{5.14}$$

In the case of a bunched beam, in the rigid bunch approximation, one does not need to compute $W(z)$ along all the z-axis, but only at a discreet set of bunch positions $z_k = kc\tau_{rf}$, where τ_{rf} is the RF period.

Finally, from the impedance of the most unstable mode one can estimate the instability growth rate of a bunched beam as [57]:

$$\gamma_{b,\max} \approx -\frac{L}{C}\frac{2r_0 N_b \beta_x}{\gamma\tau_{rf}} \mathrm{Re}(Z(\omega_{\max})) - \frac{\Gamma}{2}\ , \tag{5.15}$$

where C is the ring circumference and L is the total length of the magnets. For the Recycler $L/C \approx 1/2$.

5.2 Fast instability in Recycler

The described model was applied to estimate the growth rate of the fast electron cloud instability in Recycler. In order to use the model one needs to know the density of the electron cloud and the rate of its build-up. These quantities were obtained by measuring the betatron frequency shift and comparing it with the build-up simulations.

To determine the parameters of the electron cloud one batch of 80 proton bunches of 5×10^{10} ppb was injected into the ring and the shift of the horizontal tune was measured as a function of the bunch number. Because the positive horizontal tune shift is a distinctive feature of the electron cloud, it allowed an estimation of the cloud density. In order to check with the simulation the cloud density both within the high-intensity batch and after its passage, a witness bunch of low intensity – $8*10^9$ p, insufficient to clear the electron cloud, was injected at different positions behind the main batch.

The experimental results are in good agreement with the simulation (Fig. 5.2) and the small discrepancies may come from the multiple assumptions used in Eq. (5.11), namely the smooth focusing optics, the rigid bunch approximation, and the assumption of the constant electron cloud density. The resulting dependence allows the estimation of the maximum density of electron cloud – $n_e \sim 6\times10^{11}\,\mathrm{m}^{-3}$. The density increases by an order of magnitude in 40 bunches (800 ns) and falls after the beam has passed in 10 bunches (200 ns). The characteristic rate of the build-up, defined as the increase of the cloud density by a factor of e, is about $1/20$ bunches or $\lambda \sim 2.65\times10^{6}\,\mathrm{s}^{-1}$. The parameters of the model are summarized in Table 5.1.

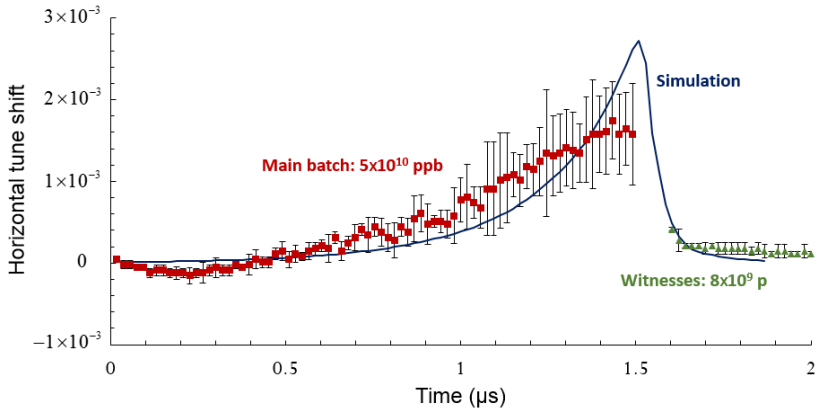

Figure 5.2: Results the of electron cloud simulation agree with the measured horizontal tune shift. Beam: $5*10^{10}$ ppb, 80 bunches, followed by one witness bunch of $0.8*10^{10}$ p at various positions. The gap between the high-intensity batch and the witness is due to the rise-time of the injection kickers.

Table 5.1: Parameters of the model

Parameter	Symbol	Value
Relativistic factor	γ	10
Revolution frequency	ω_0	0.57×10^{6} s^{-1}
Betatron frequency	ω_β	14.54×10^{6} s^{-1}
Protons per bunch	N_b	5×10^{10}
RF period	τ_{rf}	18.9 ns
Electron cloud density	n_e	6×10^{11} m^{-3}
e-p coupling frequency	ω_p	0.23×10^{6} s^{-1}
Electron cloud build-up rate	λ	2.65×10^{6} s^{-1}
Chromatic tune spread	$\Delta Q_x/Q_x$	10^{-4}
Landau damping rate	Γ	0.25×10^{-3} s^{-1}

According to Eq. (5.9), the most unstable mode is $n_{max} \approx 30$, and its frequency is about 0.4 MHz. The impedance of this mode, calculated using Eq. (12), is 20 MΩ/m (Fig. 5.3). Figure 5.4 depicts the corresponding wake function *W(k)* as a function of bunch number *k*. *W(k)* fits an exponential decay curve

$$W = W_0 \exp(-\Delta z / c\lambda), \Delta z > 0. \tag{5.16}$$

The estimate of the mode frequency qualitatively agrees with the simulation in the PEI code and the stripline measurement. PEI simulated the ring, completely filled with 588 bunches of 5×10^{10} p. The resulting frequency is about 0.7 MHz (Fig. 5.5). In the stripline measurement one batch of 80 bunches of the same charge was injected. The measured frequency was about 0.9 MHz. Both simulated and measured frequencies agree to about a factor of two with each other and the estimate.

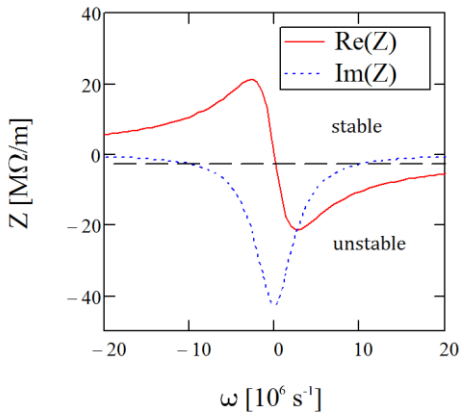

Figure 5.3: Real and imaginary parts of impedance as a function of a mode angular frequency *ω*. The dashed line represents the Landau damping term in Eq. (5.15). The modes with Re(*Z(ω)*) below the dashed line are unstable.

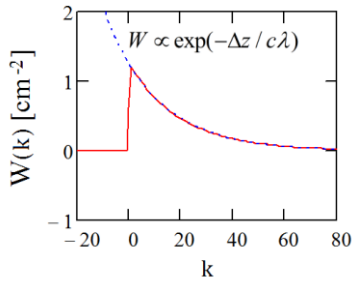

Figure 5.4: Electron cloud wake falls down exponentially with distance.

Using the calculated value of the real part of the impedance we can now estimate the growth rate using Eq. (5.15). We obtain a growth rate of $\gamma_{\max} = 0.033$ and the characteristic time of the instability $\tau_{\max} = 1/\gamma_{\max} \approx 30$ revolutions (0.3 ms). This rate is consistent with the observations of the fast instability in Recycler (Fig. 2.6).

The instability threshold can be estimated from the condition $\mathrm{Im}(\Delta\omega) \le 0$ for all modes. At the threshold the positive growth term in Im($\Delta\omega$) is compensated by the negative Landau damping term Γ. For the considered parameters of the Recycler ring the threshold electron cloud density is $n_{thr} = 8\times10^{10}$ m^{-3}. According to the build-up simulation (Sect. 4.3.6) the threshold density is reached at the beam intensity of 4.5×10^{10} ppb, which is consistent with the observations of the fast instability (Figs. 2.7, 2.8).

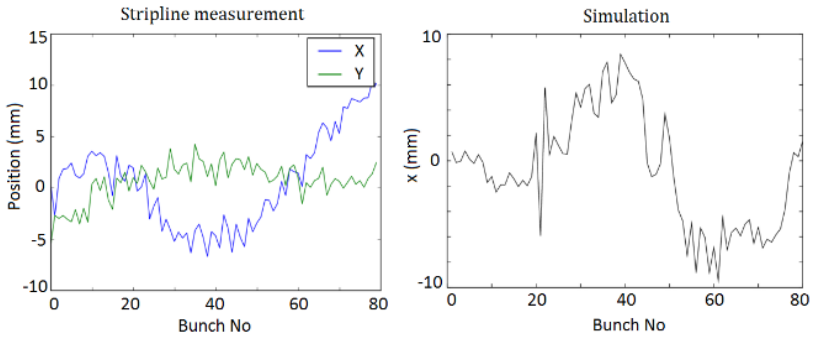

Figure 5.5: Simulation in PEI and stripline measurements show an instability in the horizontal plane with a period of slightly less than the length of a batch and a frequency < 1 MHz.

5.3 Instability at higher intensities

We developed a simple analytical model of the electron cloud instability with the cloud trapped in the combined function dipoles has been developed. It allows an estimation of the instability threshold, the frequency of the most unstable mode and its growth rate. For the current parameters of the Recycler beam, the model yields an unstable mode with a frequency of 0.4 MHz and a growth rate of 30 revolutions, which is consistent with the observations of the fast instability and the simulations in PEI. The estimated threshold intensity of resulting multibunch instability is also consistent with the intensity scans performed at Recycler.

The model allows the prediction of the rate of the instability for higher intensities of the proton beam, given an estimate of the electron cloud density, which can be obtained from numerical simulations or a direct measurement. In this analysis we compare the resulting growth rates using the simulated electron cloud density for different secondary emission yields.

According to the model, the instability can be dangerous at higher intensities. For SEY = 2.1 the instability is most severe at the beam intensity $N_p = 6\times10^{10}$ ppb, which is consistent with the measurements (Fig. 5.6). Because of the saturation of the electron cloud build-up, the instability rate increase further at higher intensities. The rate is significantly lower for lower SEY's. Decreasing the yield by 0.1 one can reduce the rate by one to two orders of magnitude.

Although the rate for the PIP-II intensity of 10^{11} ppb does not exceed one for lower intensities, the instability can still be extremely dangerous – with a growth rate below 10 revolutions – for high enough secondary yields. With sufficient scrubbing one should be able to condition the beampipe enough to allow for the high intensity operation. A test of scrubbing can be done at a lower intensity of $6-7\times10^{10}$ pbb, where the growth rate is reaches its maximum.

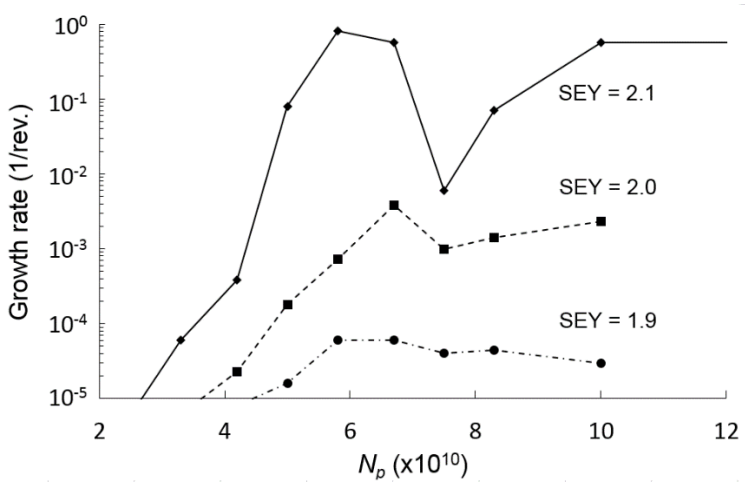

Figure 5.6: The maximum growth rate is achieved at the intensities of $6-7\times10^{10}$ ppb. The growth rate decreases significantly for lower secondary emission yield.

5.4 Landau damping of the fast instability using octupoles

As shown in Sect. 5.1, the presence of a spread of the betatron frequencies leads to reduction of the instability growth rate via Landau damping (Eq. (5.15)). Normally, the frequency spread is too small to change the landscape of the unstable of (Fig. 5.3) and significantly affect the growth rate. The spread can be increased though either artificially, introducing special nonlinear focusing elements (i. e. octupoles or electron lenses), or by the electron cloud itself, thanks to the nonlinearity of its potential. In this section we consider increasing the Landau damping using a special set of octupole magnets.

In our model the Landau damping is linear with the frequency spread. Due to the fast growth rate of the instability a high damping rate, and hence a huge frequency spread is required to stabilize the

beam (Fig. 5.7). According to Eqs. (5.3), (5.15), a $\Delta Q_x = 0.04$ spread is needed to suppress the instability in the Fermilab Recycler.

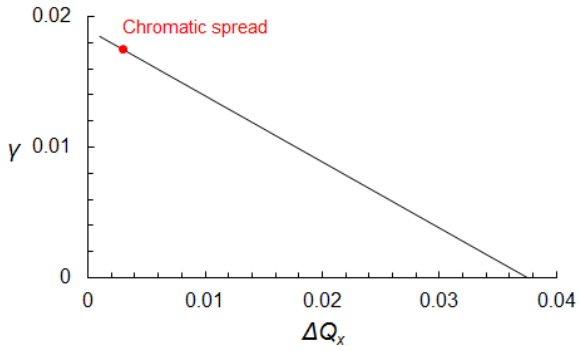

Figure 5.7: The estimated instability growth rate decreases linearly with the spread of horizontal betatron frequencies.

Achieving such a huge spread of betatron frequencies with nonlinear octupole magnet might be challenging. Typically, adding a strong nonlinearity to an otherwise perfect linear focusing lattice breaks down the integrability of the single particle motion. It leads to resonant behavior and chaotic motion at large amplitudes, resulting in a reduction of the dynamic aperture. The exact value of the maximum attainable octupole tune spread is machine-specific and depends on the choice of bare betatron tunes (which are typically about equal). For example, a maximum tune shift of 5×10^{-3} at 6σ can be obtained without damaging the dynamic aperture at the LHC [58].

One of the ways of improving the single particle stability is to restore the integrability by using a special linear focusing lattice and tailoring the nonlinear potential to it as described in [59]. Using conventional octupole magnets one can achieve single particle dynamics with one integral of motion (for two transverse degrees of freedom. Even a single integral of motion can significantly improve particle dynamics in terms of achievable tune shifts and dynamical aperture. For instance, it proved to

be beneficial for achieving a record-high beam-beam tune shift with round colliding beams at VEPP-2000 at BINP [60].

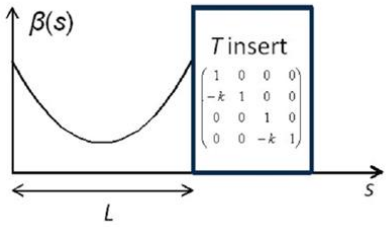

Figure 5.8: The ring outside of the nonlinear section has a transfer matrix of a thin axially symmetric lens [59].

To obtain one integral of motion one can create the nonlinearity by a set of octupole magnets, placed in a drift section with equal beta-functions and zero dispersion (Fig. 5.8). The rest of the ring outside the octupole channel has to have a linear transfer matrix of a thin axially symmetric lens with. The strength of the octupoles should vary inversely proportional to the cube of the beta-function β^3 at their location, creating a potential:

$$V(x,y;s)=\frac{\alpha}{\beta(s)^3}\left(\frac{x^4}{4}+\frac{y^4}{4}-\frac{3x^2y^2}{2}\right), \tag{5.16}$$

where a is the strength of the potential, x and y are the transverse coordinates, and s is the longitudinal coordinate. Then, in the normalized coordinates the potential $U=\beta(s)V(x,y;s)$, and the resulting Hamiltonian H (neglecting the longitudinal motion) is

$$H=H_0+U=\frac{1}{2}\left(P_x^2+P_y^2+x_N^2+y_N^2\right)+\alpha\left(\frac{x_N^4}{4}+\frac{y_N^4}{4}-\frac{3x_N^2y_N^2}{2}\right), \tag{5.17}$$

where x_N, y_N, P_x, and P_y are the normalized transverse coordinates and momenta. H is independent of the longitudinal position s and, thus, is an integral of motion in the octupole channel. Since the ring

outside of the channel has the betatron phase advance of a multiple of π, it therefore preserves the integral of motion to first order.

The Hamiltonian (5.17) has two integral manifolds $x_N = P_x = 0$ and $y_N = P_y = 0$ where the motion essentially in 1D and therefore integrable. Because the potential of this system is a positive-definite form, the motion is stable and bounded for any initial amplitude, and its frequency increases infinitely with amplitude (for $\alpha > 0$). In general, apart from these special cases, the motion is in 2D. Due the lack of the second integral the motion the system has a finite dynamic aperture (Fig. 5.9 (a)). The size of the region of stable motion is approximately defined by the distance to the unstable fixed points $P_x = P_y = 0, |x_N| = |y_N| = 1/\sqrt{2\alpha}$. From our modeling we observed that a particle becomes unstable if its amplitude is greater than ~ $0.6/a^{1/2}$. The region of regular motion is actually slightly smaller because of a thin layer of bounded chaotic motion near the boundary of the stable zone. The normalized acceptance of the system is

$$A = x_N{}^2 \sim (0.6\alpha^{-1/2})^2 \sim 0.4/\alpha \tag{5}$$

Unlike the 1D case, the frequency shifts of a 2D system are both positive and negative. Figure 5.9 (b) depicts the spread of frequencies, obtained by tracking of 10^4 particles with a Hamiltonian given by Eq. (5.17). The maximum positive tune shift is about 0.14, while the negative is about 0.26, resulting in the total frequency spread of 0.4, or, going back to the physical units, 40 % of the fractional tune.

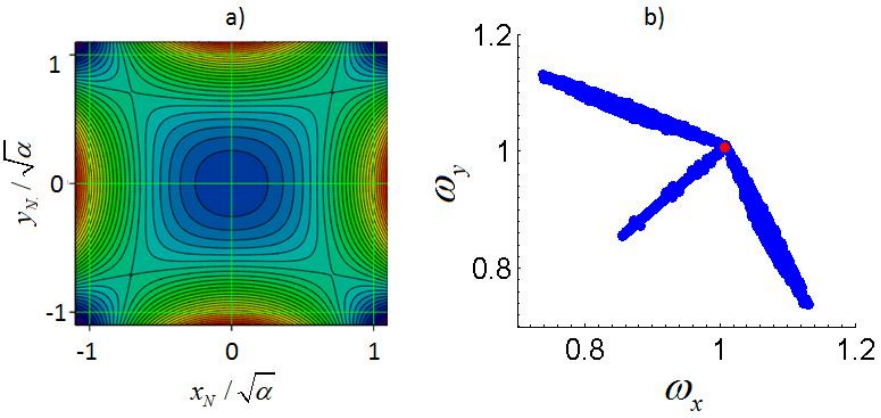

Figure 5.9: The motion remains bounded only for initial amplitudes < $0.6\alpha^{-1/2}$, and the corresponding tune spread is 0.7. a) – Lines of equal potential of the Hamiltonian (2). b) – Frequency spread of the stable particles; the linear tune (without the octupole potential) is normalized to 1 (red dot) [61].

Unlike the case of a short octupole, added to a linear lattice, the maximum betatron frequency spread $\Delta Q_{\max}$, achievable with this octupole channel is not limited by the octupole and higher order resonances. Instead, it scales linearly with the phase advance in the nonlinear section $\Delta\Psi$ [61]:

$$\Delta Q_{\max} \sim 0.4\Delta\Psi \tag{5.18}$$

Numerical studies show that a spread of $\Delta Q_{\max} \sim 8\times10^{-2}$ can be achieved with conventional octupole magnets in a realistic 3D accelerator lattice with imperfections. This spread is sufficient for stabilizing the Recycler beam by Landau damping. Creating it requires a total phase advance of 0.3 over one or several nonlinear sections and a control the linear optics at the 10^{-2} level of precision [61].

CHAPTER 6

CONCLUSION

Combined function magnets are widely used in the present day particle accelerators. Because of the gradient of the magnetic field (which provides the transverse focusing) these magnets can trap the electrons of the electron cloud, created by the beam. These trapped particles make it possible for the cloud to accumulate over multiple revolutions, possibly leading to a fast transverse instability. Such an instability, driven by the multi-turn accumulation of the electron cloud in combined function magnets has been observed in the Fermilab Recycler proton storage ring.

The fast instability in Recycler has a number of features, characteristic of an electron cloud instability: very fast growth rate, nonlinear dependence on beam intensity and bunch length, and conditioning during the high-intensity operation. Its electron cloud nature has been proven by the clearing bunch experiment – a pilot bunch of low charge, following the main high-intensity beam, kicks the electrons, confined by the magnetic field, and clears the aperture. The clearing bunch destroys the trapped cloud, preventing its multi-turn accumulation. We have observed that the fast instability can be mitigated using this method. This finding suggests that the instability is caused by electron cloud and that the cloud is trapped in Recycler magnets.

A measurement of microwave propagation through has shown the presence of electron cloud inside a Recycler combined function magnet. Its density reaches $\sim 10^{12}$ m^{-3} at high beam intensities. Measuring the time constants of cloud build-up and decay has proven to be technically challenging because of the interference from the beam Schottky signal. This interference seems unavoidable for a fast measurement.

Numerical simulation of the electron cloud build-up in the PEI code agrees with analytical estimates and show that up to 10^{-2} of the electrons can be trapped in the magnetic field of a Recycler

combined function dipole after beam has left the magnet. The trapping significantly affects the density of the electron could, allowing it accumulating over multiple revolutions and eventually reaching a density much higher than in a pure dipole. For the parameters of Fermilab Recycler with one batch of normal intensity the cloud reaches an average linear density of $\sim 10^9$ m^{-1} in a combined function magnet compared to $\sim 10^7$ m^{-1} in a pure dipole of the same field strength. These results agree qualitatively with the observed stabilization of the beam by a clearing bunch and quantitatively with the measurements of betatron tune shift. At higher beam intensities the electron cloud reaches the saturation at the density of 10^{10} m^{-1}, or the peak density on axis of 2×10^{12} m^{-3}, which is consistent with the microwave measurement. The saturation occurs when the space charge force of the cloud starts compensating the kick of proton beam.

We have constructed a simple analytical model of the electron cloud instability with the cloud trapped in the combined function dipoles. The model allows the estimation of the instability threshold and growth rate for a given electron cloud density. For the current parameters of the Fermilab Recycler the model predicts a multibunch instability in the horizontal plane with a growth rate of 30 revolutions and the frequency of the most unstable mode of 0.4 MHz. The analytical estimates are in good agreement with the experimental observations of the fast instability in Recycler and with the numerical simulations in PEI.

Thanks to its low frequency the instability can, in principle, be efficiently suppressed with a strong enough transverse feedback system, acting on the center of mass of each bunch. Stabilization of the Recycler beam by means of the intrinsic Landau damping requires a huge spread of betatron frequencies of the order of 3×10^{-2}. Such a betatron frequency spread is an order of magnitude greater than what is typically achieved in accelerators with conventional octupole magnets. The required spread can be created in a special but realistic accelerator focusing lattice with a special octupole

channel that preserves one integral of motion – the Hamiltonian. Numerical simulations show that one can achieve a spread of up to 8×10^{-2} without restricting the dynamic aperture [61].

According to the numerical studies in PEI, the maximum electron cloud density and the most severe resulting instability is achieved at the intensity of $6-7\times10^{10}$ ppb. The instability growth rate at the PIP-II intensity of 10^{11} ppb the electron cloud density shall not exceed that at the lower intensities. Reduction of the secondary emission yield even by as little as 0.1, for example during special beampipe conditioning runs, can significantly reduce the instability growth rate.

References

[1] W. Höfle, "Observations of the electron cloud effect on pick-up signals in the SPS", in *Proc. 10th Workshop on LEP-SPS Performance*, Chamonix, France, 2000.

[2] G. Bregliozzi, G. Lanza, V. Baglin, and J. M. Jimenez, "Vacuum Pressure Observations during 2011 Proton Run", in *Proc. Evian 2011 LHC Beam Operation Workshop*, Evian, France, 2011.

[3] L. Tavian, "Performance Limitations of the LHC Cryogenics: 2012 Review and 2015 Outlook", in *Proc. Evian 2012 LHC Beam Operation Workshop*, Evian, France, 2012.

[4] W. Fischer *et al.*, "Electron cloud observations and cures in the relativistic heavy ion collider," *Phys. Rev. ST Accel. Beams* vol. 11, no. 4, p. 041002, 2008.

[5] J. A. Crittenden *et al.*, "Studies of the Effects of Electron Cloud Formation on Beam Dynamics at CesrTA," in *Proc. 2009 Particle Accelerator Conference*, Vancouver, BC, 2009, p. 4631-4633

[6] R. Macek, "Possible cures for electron cloud problems", in *Proc. ECLOUD'02* Workshop, Geneva, Switzerland, 2002

[7] H. Fukuma, "Electron Cloud Observations and Predictions at KEKB, PEP-II and SuperB Factories," in *Proc. ECLOUD'12*, La Biodola, Isola d'Elba, Italy, 2012

[8] M. Zobov *et al.*, T. Demma, and P. Raimondi, "Operating experience with electron cloud clearing electrodes at DAFNE," in *Proc. ECLOUD'12,* La Biodola, Isola d'Elba, Italy, 2012.

[9] R. Cappi, M. Giovannozzi, E. Métral, G. Métral, G. Rumolo, and F. Zimmermann, "Electron cloud buildup and related instability in the CERN Proton Synchrotron", *Phys. Rev. ST Accel. Beams,* vol. 5, 094401, 2002

[10] K. Cornelis, "The electron cloud instability in the SPS", in *Proc. ECLOUD'02,* Geneva, Switzerland, 2002.

[11] G. Iadarola and G. Rumolo, "Electron cloud in the CERN accelerators (PS, SPS, LHC)," in *Proc. ECLOUD'12*, La Biodola, Isola d'Elba, Italy, 2012.

[12] S. Holmes *et al.*, "Long Term Plans to Increase Fermilab's Proton Intensity to Meet the Needs of the Long Baseline Neutrino Program", in *Proc. IPAC'16*, Busan, Korea, pp. 3982-3985, 2016

[13]M. Furman, "Electron Cloud Effects in Particle Accelerators", *in Proc. ECLOUD'2012,* La Biodola, Elba, Italy, 2002

[14]F. Zimmermann, "Particle-matter interaction" in *Handbook on Accelerator Physics*, A. Chao, M. Tigner, Ed. World Scientific, 1999

[15]J. A. Crittenden, Y. Li, S. Poprocki, and J. E. San Souice, "Electron cloud simulations for the low-emittance upgrade at the Cornell Electron Storage Ring", in *Proc. NAPAC'16*, Chicago, IL, Oct. 2016

[16]F. Zimmermann, "A Simulation Study of Electron-Cloud Instability and Beam-Induced Multipacting in the LHC," SLAC-PUB-7425, LHC Project Report 95, 1997.

[17]M. A. Furman, M. Pivi, "Probabilistic model for the simulation of secondary electron emission", *Phys. Rev. ST Accel. Beams* vol. 5, p. 124404, 2002

[18]E. Benedetto *et al.*, "Review and Comparison of Simulation Codes Modeling Electron-Cloud Build Up and Instabilities", in *Proc. EPAC'04*, Lucerne, Switzerland, 2004, pp. 2502-2504

[19]G. Iadarola, "Electron Cloud Studies for CERN Particle Accelerators and simulation Code Development", Ph.D. thesis, Beams Dep., CERN, CERN-THESIS-2014-04, 2014

[20]M. Backfish, J. Eldred, C. Y. Tan, and R. Zwaska, "Beam Tests of Beampipe Coatings for Electron Cloud Mitigation in Fermilab Main Injector", *IEEE Trans. Nucl. Sci.* vol. 63 no.2, pp. 957-964, 2016

[21]F. Zimmermann, "Review of single bunch instabilities driven by an electron cloud", *Phys. Rev. ST Accel. Beams* vol. 7, p. 124801, 2004

[22]K. Ohmi, "Beam-Photoelectron Interactions in Positron Storage Rings", *Phys. Rev. Lett.* vol. 75, p. 1526, 1995

[23]K. Ohmi, S. Heifets, and F. Zimmermann, "Study of Coherent Tune Shift Caused by Electron Cloud in Positron Storage Rings", in *Proc. Asian Particle Accelerator Conference,* Beijing, 2001

[24]L. D. Landau, E. M. Lifshiz, *Physical Kinetics*, Moscow: Fizmatlit, 2002 (in Russian)

[25]V. Dudnikov, "Some features of transverse instability of partly compensated proton beams", in *Proc. PAC'01*, Chicago, IL, 2001

[26]G. Rumolo *et al.*, "Electron cloud effects on beam evolution in a circular accelerator", *Phys. Rev. ST Accel. Beams* vol. 6, p. 081002, 2003

[27]Y. Ji, L. Spentzouris, and R. Zwaska, "Secondary electron yield measurement and electron cloud simulation at Fermilab", in *Proc. IPAC'15*, Richmond, VA, USA

[28]Y. Ji, L. Spentzouris, and R. Zwaska, "In-Situ Secondary Electron Cloud Measurement at Fermilab Main Injector", in *Proc. NAPAC'16*, Chicago, IL, USA

[29]J. Eldred *et al.*, "Fast Transverse Instability and Electron Cloud Measurements in Fermilab Recycler", in *Proc. HB'14,* East Lansing, MI, 2014, pp. 419-427

[30]J. Eldred, "The High-Power Recycler: Slip-stacking & Electron Cloud", Fermilab, Nov. 2015

[31] James Patrick, "The Fermilab accelerator control system", in *Proc. ICAP'06*, Chamonix, France, 2006

[32]D.E. Johnson, V. Lebedev, and I. Rakhno, "Fermilab Booster Injection Upgrade to 800 MeV For PIP-II", in *Proc. IPAC'15*, Richmond, VA, 2015, pp. 3986-3988

[33]Brian Fellenz, Philipp Adamson. Private communication

[34]B. Banerjee *et al.*, "Fermilab Main Injector Beam Position Monitor Upgrade", in *Proc. Beam Instrumentation Workshop 2006: Twelfth Beam Instrumentation Workshop*, Batavia, Illinois, 2006

[35]Brian Fellenz. Private communication

[36]J. Crisp, K. Gubrienko, and V. Seleznev, "Stripline Detectors for Main Injector", in *Proc. National 16th Conf. on Accelerators*, Protvino, Russia, 1998

[37]A. Chao, *Physics of Collective Beam Instabilities in High Energy Accelerators*, Ney York, NY: Wiley, 1993

[38]R. Ainsworth, P. Adamson, A. Burov, I. Kourbanis, and M.-J. Yang, "Estimating the transverse impedance in the Fermilab Recycler", in *Proc. IPAC'16*, Busan, 2016, pp. 867-869

[39]S. De Santis *et al.*, "Measurement of Electron Clouds in Large Accelerators by Microwave Dispersion", *Phys. Rev. Lett.* vol. 100, p. 094801, 2008

[40]N. Eddy *et al.*, "Measurement of Electron Cloud Density with Microwaves in the Fermilab Main Injector", in *Proc. PAC'09*, Vancouver, Canada, 2009

[41]J. P. Sikora *et al.*, "Electron Cloud Density Measurements in Accelerator Beam-pipe Using Resonant Microwave Excitation", *Nucl. Instrum. Methods Phys. Res. A,* vol. 754, pp. 28-35, 2014

[42]T. Kroyer, F. Caspers, and E. Maher, "The CERN SPS Experiment on microwave transmission through the beampipe", in *Proc. PAC'05*, Knoxville, TN, 2005

[43]W. Schottky, "Regarding Spontaneous Current Fluctuation in Different Electricity Conductors", *Ann. Phys.*, vol. 57, p. 541, 1918

[44]V. Balbekov and S. Nagaitsev, "Longitudinal Schottky Spectra of Bunched Beams", in *Proc. EPAC'04*, Lucerne, Switzerland, 2004

[45]F. Caspers, "Schottky Signals", *Proceedings of CERN Accelerator School 2008*, Dourdon, France, 2008.

[46]A. Janson, V. Lebedev, R. Moore, and V. Shiltsev, "Beam Instrumentation" in *Accelerator Physics at the Tevatron Collider*, V. Lebedev, V. Shiltsev Ed. Springer, 2014

[47]S. Paret, V. Kornilov, O. Boine-Frankenheim, and T. Weiland, "Transverse Schottky and Beam Transfer Function Measurements in Space Charge Affected Coasting Ion Beams", *Phys. Rev. ST Accel. Beams*, vol. 13, p. 022802, 2010

[48]S. Antipov, N. Eddy, and S. Nagaitsev, "Using a Beam Position Monitor as a Schottky Detector at Recycler", in preparation

[49]M. Billing *et al.,* "Measurement of electron trapping in the Cornell Electron Storage Ring", *Phys. Rev. ST Accel. Beams* vol. 18, p. 041001, Apr. 2015

[50]] P. J. Channel, "Two-Stream Instability Model With Electrons Trapped in Quadrupoles", *JINST* vol. 4, p. 08008, 2009

[51]R. Macek, et al., "Electron cloud generation and trapping in a quadrupole magnet at the Los Alamos proton storage ring", *Phys. Rev. ST Accel. Beams* vol. 11, p. 010101, Jan. 2008

[52]A. D. MacDonald, *Microwave Breakdown in Gases*. New York, NY: Wiley, 1966

[53]K. Ohmi, "Electron cloud effects: codes and simulations at KEK", CERN Rep. CERN-2013-002, pp. 219-224

[54]M. Bassetti and G. A. Erskine, "Closed expression for the electrical field of a two-dimensional Gaussian charge", CERN-ISR-TH-80-06, CERN, 1980

[55]T. Demma, A. Drago, S. Guidicci, M. Zobov, and K. Ohmi, "A simulation study of the electron cloud instability at DAFNE", in *Proc. PAC'09*, Vancuver, Canada, 2009

[56]S. Y. Lee, *Accelerator Physics*, Singapore: World Scientific, 2008

[57]Yu. Alexahin, "Algorithm for finding effective impedance from e-cloud buildup simulations", FNAL Beams-doc-4863-v1, Fermilab, Jun. 2015

[58]J. Gareyte, J. P. Koutchouk, F. Ruggiero, CERN-LHC-PROJECT-REPORT-091, 1997

[59]V. Danilov and S. Nagaitsev, "Nonlinear Accelerator Lattices with One and Two Analytic Invariants", *Phys. Rev. ST Accel. Beams* vol. 13, 084002, 2010

[60]A. Ronamov *et al.*, "Status of the Electron-Positron Collider VEPP-2000", in *Proc. PAC'13*, Pasadena, CA, pp. 14-18, 2013

[61]S. Antipov, S. Nagaitsev, and A. Valishev, "Single-Particle Dynamics in a Nonlinear Accelerator Lattice: Attaining a Large Tune Spread with Octupoles in IOTA", submitted for publication